Risk posed by neutron contamination in high energy radiotherapy

A thesis submitted in fulfilment of the requirements for the degree of Doctor of Philosophy

Stephanie Keehan

Bachelor of Applied Sciences (Physics) with Distinction – RMIT University
Bachelor of Applied Sciences (Honours): First class – RMIT University

School of Science

College of Science, Engineering and Health

RMIT University

May, 2017

RISKS POSED BY NEUTRON CONTAMINATION IN HIGH ENERGY RADIOTHERAPY

Stephanie Keehan

Bachelor of Applied Sciences (Physics) with Distinction

Bachelor of Applied Sciences (Honours): First class

School of Science

College of Science, Engineering and Health

RMIT University

A thesis submitted for the degree of Doctor of Philosophy

May, 2017

Declaration

I certify that except where due acknowledgement has been made, the work is that of the author alone; the work has not been submitted previously, in whole or in part, to qualify for any other academic award; the content of the thesis is the result of work which has been carried out since the official commencement date of the approved research program; any editorial work, paid or unpaid, carried out by a third party is acknowledged; and, ethics procedures and guidelines have been followed. I acknowledge the support I have received for my research through the provision of an Australian Government Research Training Program Scholarship.

Stephanie Keehan, May 2017

Supervisors

Professor Rick Franich
RMIT University

Doctor Michael Taylor
RMIT University

Professor Tomas Kron
Peter MacCallum Cancer Centre

Acknowledgements

Firstly, my deep thanks to my supervisors. Thanks to Rick for his scientific guidance and thorough attention to detail in the experimental design, analysis and communication. Thanks for the many opportunities to develop many new skills. Thanks to Michael for teaching me nuclear physics and how to drink good whiskey. Thanks (I think) for sharing your love of unnecessary pie charts and obscure foreign language references. Thanks to Tomas for his truly remarkable levels of unfailing enthusiasm and ever-practical advice. I have benefitted tremendously from the depth and breadth of his knowledge.

Thanks to my fellow students in the RMIT Medical Physics team: Max Hanlon, Jeremy Supple, Adam Yeo, Peta Lonski, Ryan Smith, Mary Finnegan, and Leon Dunn, for the collaboration and collusion. All of you have listened patiently to a lot of neutron problems over the years. For critical access to linacs, equipment and expertise: Ryan Smith and the staff at the Alfred were there at all hours of the day and night topping up the bucket of photons, and Peta Lonski and the team at Peter MacCallum who listened to a lot of noisy TLD readouts. Duncan Butler, Tracy Wright and Chris Oliver at ARPANSA also provided a few essential "calibrated neutrons". I couldn't have done it without your support.

I owe a lot of gratitude to the entire physics department at RMIT. Quite a few (un?)fortunate professors have put with me since my undergraduate. Special thanks to Salvy Russo, Dougal McCulloch, Gary Bryant, Jared Cole, and Arwen Pagon for their support and encouragement over many years. I also want to thank Lisa Dias from the school of applied science for her excellent advice and assistance. I also want to thank my fellow students doing all the other physics: Jackson Smith, Martin Cyster, Muhammad Ahmed, Jair Garcia, Jan Jeske, Emelie Flood, Patrick Charchar, and Masturina Kracica for all the coffee breaks (and beers).

I am grateful to the team at ACDS and the rest of ARPANSA who not only employed me, but fully supported my continued work on this thesis. Thanks to Ivan Williams for looking over the first drafts, and Duncan Butler for believing I knew what I was doing. My sincerest thanks to Jessica Lye for moral support and practical advice on juggling work and study. I'm also very grateful to Maddy Shaw, Andrew Alves, Joerg Lehmann, Peter Thomas and Peter Harty who have taught me a lot about physics, dosimetry, uncertainties and clinical relevance.

Thanks to my parents, Karene and Mick, for starting it all by giving me an education and encouraging me to go to university. I think they were a bit bemused when I stayed longer than 3 years, but I very much appreciate their enduring support and the support of my entire family, including my wonderful sisters, Sarah and Natasha. Finally: a very big thank-you to Roshan, for cooking for me and putting up with me throughout.

Table of Contents

List of figures

List of tables

Summary

Radiotherapy is a common cancer treatment which aims to use radiation energy to kill tumour cells without damaging healthy tissue. High energy x-rays penetrate tissue deeply, depositing most of their energy beyond the skin and shallow tissues. X-rays with energies above 8 MeV may interact to produce neutrons, to which the patient is then exposed. Treatment planning systems (TPS), which calculate the amount of energy deposited to biological structures, do not currently account for contaminant neutrons produced in high energy interactions.

Constant improvements in modern radiotherapy techniques have resulted in better patient life expectancy than ever before. The unfortunate corollary of increased life span is increased manifestation of late onset side effects from low dose radiation exposure. This has resulted in an increased drive to reduce the dose to untargeted tissues as much as possible. A perfect treatment plan delivers a prescribed dose to the target volume and no dose to any other tissue. In reality, there is always some tissue through which the radiation must pass in order to reach the target, and some energy which passes beyond the intended target volume. In addition, there is unavoidable scattering of radiation within the patient, which results in out-of-field doses to untargeted tissue.

Dose to untargeted tissues resulting from x-ray energy is relatively well understood and is calculated and reported by TPS. Dose resulting from contaminant neutrons is not currently considered by TPS. The overall number of neutrons produced is relatively low, because high energy x-rays may interact in a variety ways and reactions producing neutrons are generally less likely. However, energy deposited by radiation can produce different biological outcomes depending on the type of radiation which deposits the energy. The biological damage inflicted by neutron radiation depends on the energy of the neutrons, and neutrons with energy around 1 MeV may be up to 20 times more damaging than x-rays.

So, how do we know the risk associated with neutrons produced from high energy x-rays? Measure the number of neutrons produced? Measure the amount of energy they deposit? Neutron radiation is incredibly difficult to quantify, much more so than alpha, beta, x-ray, gamma or proton radiation. Neutrons are neutrally charged particles, which means they are not attracted or repelled by the positive nuclei or negative electrons which make up all matter. Neutrons primarily pass straight through most materials without leaving a trace of evidence. This makes them quite difficult to detect! Neutrons do interact with the nuclei of some materials, in nuclear reactions, which produce energy and secondary particles which can more easily be detected. The extra energy released in these interactions and their complex probability functions make it difficult to determine the number of neutrons or the energy they would release in human tissue.

The high uncertainty in neutron measurement techniques has resulted in some controversy around the use of high energy x-ray beams. There is no question that the deeper penetration of the higher energy x-rays is extremely useful for treatment of some anatomical sites. The source of the contention is the degree of risk posed by the neutrons themselves. Without an accurate and precise method for quantifying the degree of neutron contamination, an accurate determination of the risk cannot be made.

Thermoluminescence dosimeters (TLDs) and activation foils have been used in this work to quantify neutrons produced in high energy radiotherapy. TLDs are a common radiotherapy dose measurement tool and are routinely used in existing clinical protocols. Lithium fluoride is a common TLD material and the two naturally occurring isotopes of lithium, ^{6}Li and ^{7}Li, have very different probabilities for neutron interaction. TLDs made from these materials can be used in pairs to produce signals which in combination can be correlated with the degree of neutron exposure. Activation foils are materials which

become radioactive when exposed to neutrons. A first principles calculation can be used to determine the number of neutrons causing activation in a material.

Both these methods for neutron detection are highly dependent on the energy of the neutrons. Both produce a response related to the number of incident neutrons which needs to be corrected for the energy of the neutrons which are to be measured. The energy deposited by the neutrons in the detector material is not directly related to the energy which would be deposited in tissue in a patient exposure. Another energy correction is required to quantify the biological damage which may occur. This is the primary source of uncertainty and the cause of the disagreement between the vast number of existing publications on the topic.

This work determines energy correction values for the calibration of LiF TLDs for neutron measurements. The neutron energy spectrum relevant to high energy radiotherapy is modelled and used to determine energy corrections for activation foils. It is also needed to convert the response of detectors to the energy deposition in tissue and to correct for biological effect.

Additional risk from neutron contamination is also examined. The production of neutrons may induce radioactivity in other materials. The medical linear accelerator (linac) used to produce the treatment x-rays may itself become radioactive when it is operated at high energies. The induced activity is low level and is mainly of concern for radiotherapy staff rather than patients as they spend much greater time in proximity to the linac. Implants within the patient may also interact in unexpected ways. Metallic implants such as prosthetic hips can become radioactive from exposure to neutrons or high energy x-rays. This is primarily of concern for patients, as it potentially induces a low level internal source of radiation.

Many existing peer reviewed publications investigate the degree of neutron exposure to patients undergoing high energy radiotherapy, but there is no consensus amongst experts regarding the risk. This stems from the high degree of uncertainty in neutron measurement techniques. This thesis discusses the challenges of neutron dosimetry and proposes a methodology for correcting for detector energy dependence. An investigation of the indirect risks of neutron production is also presented.

This thesis offers a comprehensive analysis of existing neutron detectors and dosimeters with an in-depth discussion of their properties in relation to their suitability for use in high energy radiotherapy. The energy dependence of LiF TLD response to neutron radiation is carefully examined for calibration sources and for photoneutrons from medical linacs. The energy dependence should be considered for calibration sources, but is shown to be less critical for the energies produced by linacs. The energy dependence of activation foils depends on the material chosen but can be accounted for by calculating an energy spectrum weighted interaction probability, or cross section. Converting neutron measurements to values representing dose to human tissue for a given exposure must be corrected for the energy of the neutrons.

This thesis also presents a summary of neutron dose equivalent values from peer reviewed publications and compares the effects of a number of parameters on the neutron dose. Comparison between studies is made difficult by a lack of detail on the magnitude of energy corrections used in published papers.

The indirect risk from secondary activations is considerably lower, however may be reduced by employing the existing collimation devices within linacs as shielding. A small amount of activation in hip prostheses does occur, but does not result in a significant dose to surrounding tissue.

1. Introduction

Radiotherapy involves the use of radiation energy to treat tumours. Many types of tumour cells are more sensitive to damage from radiation than healthy cells, and this inherent difference is exploited to reduce the size of and inhibit the growth of tumours. In Australia, the most common type of radiotherapy is external beam radiotherapy (EBRT) which is most often delivered by a medical linear accelerator (linac) operating with acceleration potentials in the mega-voltage (MV) range. The most commonly used acceleration potential is 6 MV which produces x-rays with a spectrum of energies up to a maximum of 6 MeV.

Any external beam of radiation incident on a patient inevitably delivers some radiation to un-targeted organs and tissues. The central goal of radiotherapy is to deliver enough radiation energy in the form of a radiation *dose* to a tumour to completely eradicate it. It is equally important to simultaneously reduce, as much as possible, the amount of dose delivered to healthy tissue. While the healthy tissue is fortunately inherently less sensitive, it is not immune to damage from radiation.

Multiple beams delivered from different entry angles, geometries and energies are used to optimise the dose distribution such that the tumour volume receives sufficient eradication dose and the surrounding tissues receive as little as physically possible. The type and location of the tumour to be treated dictate the energy of the beam which should be used. Higher energy x-rays will penetrate more deeply in tissue, and are often desired for deeply seated tumours or larger patients. Whilst the same dose may be delivered to a tumour using a lower energy beam, it can only be done so at the expense of the healthy tissues.

A risk factor in the use of high energy radiotherapy beams is the undesirable production of contaminant particles. An x-ray with enough energy may interact with the materials it encounters in a linac, causing the emission of nucleons from ordinarily stable nuclei. This phenomenon is known as the *photonuclear effect.* The energy from an x-ray can cause protons, neutrons or heavy particles to be ejected from a nucleus. A positively charged particle, such as a proton or heavy particle has a limited range and will most likely not reach a patient. Charge neutral neutrons however, are a very penetrating type of radiation, and will likely irradiate the patient.

Modern radiotherapy is highly successful in the treatment of cancer. Improved geometric conformity and advanced dynamic techniques such as intensity modulated radiotherapy (IMRT), volumetric modulated arc therapy (VMAT), deep inhalation breath hold (DIBH) and so forth, have all resulting in improved outcomes for patients. Increased life span for cancer survivors results in an increased likelihood of observable manifestations of stochastic radiation effects. These are low dose effects where a biological effect is observed with some probability proportional to the dose received by a given population. The increase in life expectancy for cancer patients has resulted in a renewed interest in the unavoidable dose received by un-targeted healthy tissue in radiotherapy. Contaminant neutrons in particular may be of concern because of their high radiation weighting factor compared to other types of radiation. Radiation weighting factors are published by the International Commission on Radiological Protection (ICRP103 2007) and are used to evaluate the risk resulting from radiation exposure (ICRP116 2010).

The dose to patients resulting from neutron contamination is not only an unwanted dose received by healthy tissues; it is also an unknown quantity. Treatment planning systems (TPS) predict and calculate doses to patients for given beam configurations. This allows the crucial prescription dose for a tumour volume to be determined and delivered. The doses to proximate un-targeted tissues are also calculated and organs at risk (OAR) adjacent to treatment target volumes are checked and limited. TPS algorithms which calculate these doses do not at present include any information about the dose deposited by

neutrons produced in high energy radiotherapy. The data required to inform the algorithms and allow calculation of the neutron dose is not yet available.

To provide TPS with enough information to calculate neutron doses for specific beam geometries incident on patients, the degree of neutron contamination must be quantified. Neutrons are neutrally charged, and do not easily interact with materials. This fundamental property makes them very difficult to detect.

A neutron may interact with the nuclei in matter in a nuclear reaction. If the probability of interaction is known, the number of incident neutrons can be calculated from the number of detections. The probability of a neutron interacting with a material to produce a measurable response is strongly dependent on the energy of the neutrons. In order to determine the energies of the neutrons present under the measurement conditions, Monte Carlo radiation transport modelling can be used. A series of particle interactions are calculated and the number of neutrons in specified energy ranges are calculated.

Many researchers have investigated the degree of neutron contamination produced by medical linear accelerators operating at high energies. Despite this, there is still controversy amongst experts regarding the levels of neutron contamination in high energy beams. The high uncertainty in neutron detection and dosimetry is the main factor contributing to the disunity, but there are also significant complexities in translating the information gathered from measurement into an actual risk to a patient. The quantity of *absorbed dose* (energy absorbed per unit mass) is used because in general it correlates with observable biological effects. *Equivalent dose* is a weighted absorbed dose which accounts for the varying degrees of biological damage done by different types of radiation. These parameters cannot be directly measured. Absorbed dose to tissue differs from the absorbed dose to whichever detector material is used because different types of nuclear interactions occur in the different materials. All interactions are energy dependent and it is not necessarily possible to relate dose in one material to dose in another.

The radiation weighting factor for neutrons is determined from experimental data for the relative biological effectiveness (RBE) and is the only radiation type to have an energy dependent radiation weighting factor (ICRP103 2007). The energy dependence of the radiation weighting factor contributes to the uncertainty when comparing results reported in published literature. Authors may state the function used to determine the weighting factor, without explicitly stating the assumptions made of the neutron energies used to evaluate the weighting factor in their study. Many published papers do not provide enough detail to extract comparable quantities. The values which are published for measurements taken under similar conditions vary over several orders of magnitude, due to differences in methodology to convert the output or response of their detectors to a dose equivalent, which is the quantity needed to evaluate the risks.

Aside from the direct exposure to the patient from neutrons produced, the photonuclear interactions which occur at high energies may contribute to other risks. Photonuclear interactions occurring in the components of the linear accelerator can cause those otherwise stable nuclei to become radioactive. After long periods of time using high energy beams, components of the machine may have built up radioactivity. This is generally most relevant to radiotherapy staff rather than patients, as the levels are very low. It may add up to a significant amount for staff who spend a lot of time in close proximity to the machines.

There is also a risk from implants and foreign objects within patients. The composition of human tissue is overwhelmingly made up of lighter elements which generally have lower probability of interacting with neutrons and becoming radioactive. Heavier elements which may be present in prostheses, pace-makers or other implants are more susceptible to activation by incident neutron radiation.

1.1 Thesis objectives

The key objectives of this thesis are as follows:

- To present a comprehensive review of methods of neutron detection and their advantages and disadvantages
- To assess the suitability and considerations for use of neutron detectors for measurements in high energy radiotherapy
- To perform systematic measurements of neutron dose and consider the risk resulting from contaminant neutrons
- To quantify the indirect risk from secondary radiation caused by activation in the linac and in hip prostheses within the patient
- To provide relevant clinical recommendations for the use of TLDs for neutron dosimetry and the radiation protection of staff from induced radioactivity for high energy beams

1.2 Thesis structure

A technical introduction to some necessary physical concepts is given in chapter 2. Chapter 3 presents a comprehensive review of methods of neutron detection which have been used in medical physics to evaluate neutrons produced by high energy medical linacs. An in-depth analysis of the properties of the detectors and their suitability is given. Additional detailed information on the two most common detectors: thermoluminescence dosimeters (TLDs) and activation foils is included.

A deeper investigation of the properties of TLDs and activation foils is presented in Chapter 4. Methodology is developed for the use of these two detectors. Some results to support the proposed techniques are presented to assist in interpretation of the responses of the detectors and how that response can be most accurately related to neutron fluence and absorbed dose. Monte Carlo modelling is used to investigate the neutron energy spectrum produced by medical linear accelerators to aid the interpretation of the detector responses.

Chapter 5 gives the results of neutron measurements taken on medical linear accelerators operating at 18 MV. Measurements of neutron fluence as a function of depth in solid water and as a function of the distance from the treatment beam field edge are presented. The neutron fluence determined with different detectors are compared and converted into absorbed dose to tissue and neutron equivalent dose.

The indirect risks arising from photonuclear interactions are discussed in chapter 6. Here, the results of measurements investigating activation of linear accelerators are presented as well as measurements of the activation of prostheses irradiated with radiotherapy beams.

Chapter 7 presents a detailed discussion of the results and the resultant risks. The neutron dose equivalents determined are compared to values reported in peer reviewed published papers for measurements taken under similar circumstances and the consequences for the assessment of the overall risk are discussed.

The final conclusions of the thesis are given in chapter 8.

1.3 Publications and presentations arising from this work

1.3.1 Refereed publications

2015 S Keehan, ML Taylor, RL Smith, L Dunn, T Kron, RD Franich
Dose and gamma-ray spectra from neutron-induced radioactivity in medical linear accelerators following high-energy total body irradiation
Radiation Protection Dosimetry 172(4): 327-332

2017 S Keehan, RL Smith, J Millar, M Esser, ML Taylor, P Lonski, T Kron, RD Franich
Activation of hip prostheses in high energy radiotherapy and resultant dose to nearby tissue
Journal of Applied Clinical Medical Physics **18** 100-105

2017 P Lonski, S Keehan, S Siva, D Pham, RD Franich, ML Taylor, T Kron
Out-of-field in vivo dosimetry using TLD in SABR for primary kidney cancer involving mixed photon fields Physica Medica **37** 9-15

1.3.2 Conference presentations

2016 S Keehan, P Lonski, ML Taylor, T Kron, RD Franich
Calibration and energy corrections for LiF based thermoluminescence dosimetry (TLD) neutron measurements
Engineering and Physical Sciences in Medicine (EPSM), 6 – 10 November 2016, Sydney

2016 S Keehan, P Lonski, ML Taylor, T Kron, RD Franich
Energy dependence of ^{6}LiF and ^{7}LiF TLD response to neutron radiation
Australasian Radiation Protection Society (ARPS), 11 – 14 September 2016, Adelaide

2015 S Keehan, RD Franich, ML Taylor, P Lonski, T Kron
SU-E-T-90 Accuracy of calibration of lithium-6 and -7 enriched LiF TLDs for neutron measurements in high energy radiotherapy
American Association of Physicists in Medicine (AAPM), 12 – 16 July 2015, Anaheim, CA

2015 S Keehan, RL Smith, J Millar, M Esser, ML Taylor, T Kron, RD Franich
SU-E-T-612 Photonuclear activation of prosthetic hips in radiotherapy
American Association of Physicists in Medicine (AAPM), 12 – 16 July 2015, Anaheim, CA

2015 S Keehan, ML Taylor, RL Smith, L Dunn, T Kron, RD Franich
TU-F-CAMPUS-T-01 Dose and energy spectra from neutron induced radioactivity in medical linear accelerators following high energy total body irradiation
American Association of Physicists in Medicine (AAPM), 12 – 16 July 2015, Anaheim, CA

2014 S Keehan, ML Taylor, T Kron, RD Franich
Method for interpretation of TLD600H and 700H neutron response for use with medical linear accelerators
AIR, RANZCR, ACPSEM Combined Scientific Meeting, 4 – 7 September 2014, Melbourne

2014 S Keehan, M Cyster, T Wright, D Butler, P Lonski, T Kron, ML Taylor, RD Franich
Do TLDs have a role in assessment of neutron dose? The importance of spectral variations for ^{6}LiF and ^{7}LiF materials.
Australasian Radiation Protection Society (ARPS), 26 – 29 October 2014, Hobart

2014 P Lonski, RD Franich, S Keehan, ML Taylor, T Kron
Out-of-field radiation dose during radiotherapy for breast cancer: improvement of dose estimation by addition of a correction for leakage dose
Australasian Radiation Protection Society (ARPS), 26 – 29 October 2014, Hobart

2014 P Lonski, RD Franich, S Siva, S Keehan, ML Taylor, T Kron
In vivo neutron detection in patients undergoing stereotactic ablative radiotherapy (SABR) for primary kidney cancer using Li-6 and Li-7 enriched TLD pairs
American Association of Physicists in Medicine (AAPM), 20 – 24 July 2014, Austin, TX

2013 S Keehan, RL Smith, J Millar, M Esser, ML Taylor, T Kron, RD Franich
Photonuclear activation of prosthetic hips in radiotherapy
Engineering and Physical Sciences in Medicine (EPSM), 3 – 7 November 2013, Perth

2013 S Keehan, ML Taylor, RL Smith, L Dunn, T Kron, RD Franich
Dose and spectral distribution of neutron induced gamma radiation in medical linear accelerators
Engineering and Physical Sciences in Medicine (EPSM), 3 – 7 November 2013, Perth

2013 ML Taylor, S Keehan, M Cyster, S Kry, T Kron, RD Franich
The photonuclear effect (Invited paper)
Engineering and Physical Sciences in Medicine (EPSM), 3 – 7 November 2013, Perth

2012 T Kron, D Wanigaratne, P Lonski, D Butler, S Keehan, A Rosenfeld, P Johnston
Neutron Dosimetry Around A Medical Linear Accelerator Using A Combination of ^{6}Lif and ^{7}LIF MCP Thermoluminescence Dosimeters
World Congress on Medical Physics and Biomedical Engineering, May 26 – 31 2012, Beijing, China

1.3.3 Invited seminars

2016 *Neutron dosimetry in radiotherapy*
Victorian Tasmanian Branch of the Australasian Radiation Protection Society

2016 *Risks posed by neutron contamination in radiotherapy*
Australian Radiation Protection and Nuclear Safety Agency (ARPANSA), Melbourne

2013 *Photonuclear activation around medical linear accelerators*
William Buckland Radiotherapy Centre, The Alfred Hospital, Melbourne

2. Background

This chapter is included to introduce some necessary physical concepts which are the foundation for the propositions put forward by this thesis. It provides an outline of the modern applications of high energy radiotherapy and those techniques to which neutron contamination is most relevant. The physics of high energy photon interactions is discussed such that the reader may know the origin of the neutron contamination. The probabilities or 'cross sections' of these interactions are shown in section 2.2 for some relevant materials. Some relevant radiation protection concepts are also introduced to illuminate the significance of the results presented later in the thesis and to engage further discussion of the ultimate risks to patients and staff.

2.1 Neutrons in high energy radiotherapy

High energy photons interacting via the photonuclear effect can cause the emission of contaminant neutrons in radiotherapy beams. Neutrons have a high relative biological effectiveness (RBE) (ICRP116 2010) and even a relatively small neutron fluence may pose a significant risk to patient safety. A conference was held in Gaithersburg, Maryland USA almost forty years ago to address contaminant neutron production in medical electron accelerators (Heaton and Jacobs 1979). Although modern medical linear accelerators (linacs) have dramatically improved in design and function since then, neutron contamination is still a factor in evaluating the risks of radiotherapy (Romero-Expósito *et al* 2015). Modern treatment techniques such as Intensity Modulated Radiation Therapy (IMRT), Volumetric Modulated Arc Therapy (VMAT) and Stereotactic Ablative Body Radiotherapy (SABR) can involve higher dose rates and longer beam times than conformal radiotherapy. High dose rates and longer beam times increase the probability of neutron production and may lead to an unavoidable higher patient risk (Kry *et al* 2005a). Although outside the scope of this thesis, the methods discussed are relevant to quantifying the risks from contaminant neutrons in proton and heavy ion therapy, the viability of which is currently under investigation in Australia.

In order to accurately quantify the risks posed by neutrons for various treatment techniques, accurate characterisation of the neutron field produced by a medical linear accelerator is required. To quantify the primary risk of neutron incidence on a patient, a number of neutron dosimetry and detection techniques are available, each with extraordinary challenges and uncertainties. Aside from the direct risk to the patient who may be exposed to neutron radiation, other materials exposed may become radioactive. Neutron activation in components of the linear accelerator and even metallic prostheses within the patient may pose a further risk to patients and staff.

2.2 The photonuclear effect

The photonuclear effect is a photon interaction with a nucleus. If a photon has sufficient energy, it may be absorbed by a nucleus, which in turn emits a nucleon or heavy particle. The interaction was first observed by Chadwick and Goldhaber (1934) who likened the "photodisintegration" of nuclei to the ionisation of atoms by light. They studied the photodisintegration of the deuterium nucleus, because of its low binding energy and simple nuclear structure. The incident photons used were the 2.6 MeV γ-rays of ^{208}Tl, which they acquired from the decay chain of ^{232}Th (L'Annunziata 2007). Chadwick and Goldhaber also noted that the 1.6 MeV γ-rays of ^{212}Bi were not of sufficient energy to cause disintegration. The energy of the incident photons must have energy greater than the nucleon binding energy to cause the emission of nucleons. These results allowed the calculation of the binding energy of the deuterium nucleus and thus calculation of an estimate of the mass of the neutron of 1.0080 ± 0.0005 atomic mass units, which is very close to the currently accepted value of 1.0087 atomic mass units. (Kessler Jr *et al* 1999).

The probability, or *cross section*, of an interaction occurring depends on the material in which the interaction occurs. Medical linear accelerators are manufactured from numerous materials, and contain a wide variety of nuclear species. The predominant elements by mass are tungsten and lead, which make up the primary collimator, jaws, multi-leaf collimator (MLC) and shielding. The most abundant isotopes of these elements are ^{184}W and ^{208}Pb (Rosman and Taylor 1999). The cross sections for the emission of neutrons through photonuclear interactions (γ,n) with these nuclei are shown in Figure 1. A typical 18 MV linac photon energy spectrum is also shown for comparison.

These isotopes of tungsten and lead have photonuclear thresholds between 7.0 and 8.2 MeV, which means that linacs operating in photon mode with an accelerating potential above 7-8 MeV may produce contaminant neutrons in addition to the treatment beam. The maximum probability for photoneutron production occurs between 12 and 15 MeV (Shibata *et al* 2011), as shown in Figure 1, which is easily encompassed by medical linacs, with high accelerating potentials.

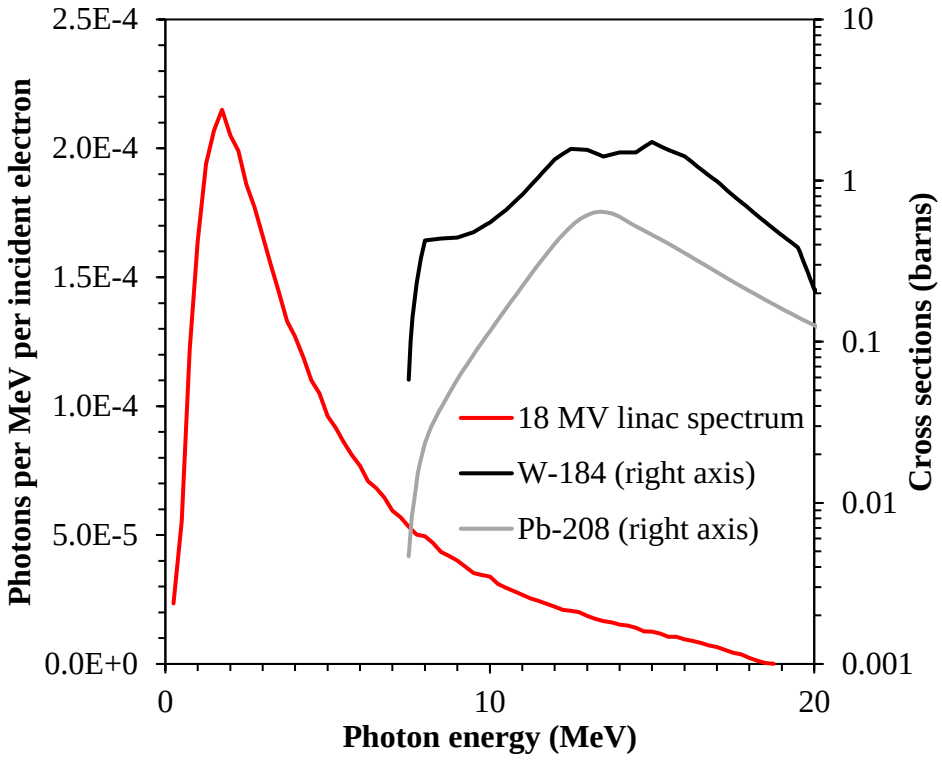

Figure 1: The photonuclear interaction cross sections (Shibata *et al* 2011) for the most naturally abundant isotopes of tungsten and lead; the main elements in a medical linear accelerator. The photon energy spectrum produced by an 18 MV Varian medical linear accelerator calculated at 100 cm source to surface distance (SSD) using the BEAM user code of EGSnrc by Sheikh-Bagheri and Rogers (2002) is shown for comparison.

2.3 Risk posed by neutrons in the context of radiotherapy

As modern radiotherapy techniques improve, patient life expectancy following treatment increases. Whilst this is excellent news for patients, a corollary is the increased importance of dose delivered to the patient outside of the target volume and the associated health risks (Taylor and Kron 2011). In the context of radiotherapy, the untargeted doses are a small percentage of the prescribed dose; however, from a radiation protection point of view, these relatively small doses may be significant in some circumstances.

2.3.1 Direct risks posed by neutron production

Neutrons are a highly penetrating radiation. Those produced in a linac easily penetrate the tungsten or lead shielding designed to attenuate photons and electrons. The cross sections for neutron capture in these materials are very low and neutron attenuation is minimal. Energy lost through scatter is also minimal because of the large mass difference. The intensity of high energy neutrons can even increase due to (n,2n) reactions in these materials (McCall *et al* 1979). Neutrons emitted following photonuclear interactions are incident on the entire patient, exposing both the radiotherapy target volume and the untargeted healthy tissues.

The biological effect of neutron radiation is much greater than that of photons and electrons. The *absorbed dose, D,* is a measurable quantity equal to the energy absorbed from a radiation per unit mass of material. The *equivalent dose, H,* accounts for the differences in the biological effects caused by different types and energies of radiation. Each radiation type, *R,* is assigned a *radiation weighting factor, w_R,* which is multiplied by the dose deposited by that type of radiation, D_R, to calculate the equivalent dose, see equation 1 (ICRP116 2010). Neutrons have a high radiation weighting factor, w_R, of up to 20 (Figure 2) compared to the weighting factor of 1.0 assigned to photons and electrons, reflecting the significance of their biological effect.

$$H_T = \sum_R w_R D_R \qquad [1]$$

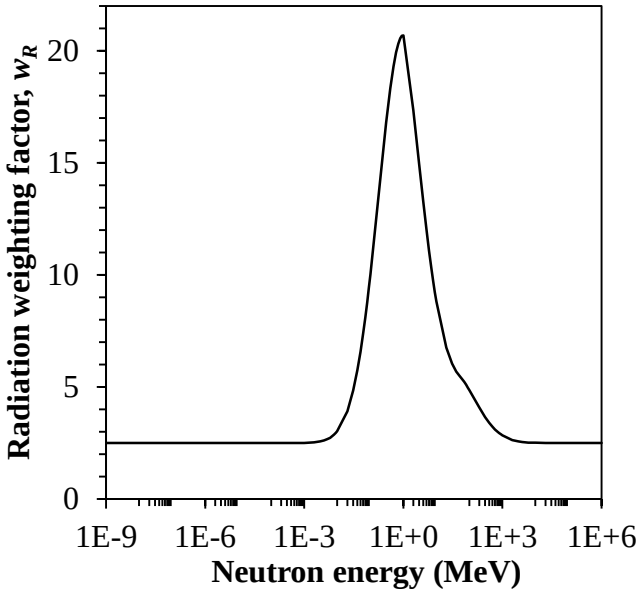

Figure 2: The ICRP116 (2010) energy dependent radiation weighting factor for neutron radiation.

2.3.2 Indirect risks posed by neutron production

The interactions which cause neutron emission may also result in the production of radioisotopes. This induced radioactivity can pose an additional risk to patients and staff. Materials which are exposed to high energy photons may emit neutrons and become activated as a result. Materials which are in turn exposed to the emitted neutrons may also become activated. The components in the linear accelerator are in the vicinity of a large fluence of high energy photons and can become radioactive from exposure to high energy beams. The patient exposed to the beam may also be activated, but this is typically less likely for the light elements which compose the bulk of biological material. Patients with implanted devices, such as prostheses or pace makers may be at a greater risk of activation because of the incorporation of heavier elements from which these are typically manufactured.

2.3.2.1 Activation of the medical linear accelerator

Delivery of high energy radiotherapy treatments may cause the linac itself to become radioactive and hence present potential health risks. Neutrons produced in high energy radiotherapy beams are ejected from nuclei primarily in the components of the linac where the photon treatment beam is produced, directed and shaped. Nuclei losing a neutron may be unstable and consequently decay via emission of other radiations. The activation of a linac following the delivery of high energy radiotherapy beams is primarily a risk to staff, who spend the greatest cumulative time in close proximity to linacs. The dose resulting from activation products is expected to be low, and patients would only be exposed for a short period of time at the end of each fraction they receive. Staff members may deliver multiple high energy treatments daily and could potentially receive a significant cumulative exposure. Israngkul-Na-Ayuthaya *et al* (2015) measured a dose of 4.14 μSv/hour at 100 cm source to surface distance (SSD) following a 1000 MU 15 MV photon beam delivered at 400 MU per minute. Annual estimates of dose to staff resulting from activation following high energy conventional 3D conformal radiotherapy range from 0.7 mSv (Almen *et al* 1991) and 0.9 mSv (Donadille *et al* 2008) up to 2.5 mSv (Perrin *et al* 2003) and 5 mSv (Ho *et al* 2012). Data from Rawlinson *et al* (2002) shows that for IMRT which requires longer beam times activation may result in an annual dose of up to 17 mSv compared to 3 mSv for conventional radiotherapy. The annual dose estimates determined by different clinics are obviously dependent on local clinical practice and frequency of high energy treatments.

2.3.2.2 Activation of prostheses

Devices implanted within patients such as prostheses, spine support or pacemakers may also become activated by exposure to neutrons. These devices are typically manufactured from heavier elements which generally have much higher cross sections for neutron interactions than the typically light elements predominantly present in biological material. Hip prostheses are of particular interest because of their proximity to beams during external beam prostate radiotherapy which benefits from the use of higher energy beams. Hip prostheses pose a number of challenges, even for low energy radiotherapy. The dose distribution can be strongly influenced by the presence of a high-Z material between the beam entry and the target volume (Reft *et al* 2003). Treatment planning systems are generally not commissioned appropriately nor intended to accurately calculate doses near high-density, high-Z materials. Keall et al (2003) compare the performance of various Monte Carlo, superposition and pencil beam treatment planning algorithms for patients and phantoms containing high-Z, high density implanted devices. The pencil beam algorithm shows particularly poor compensation for the altered charged particle equilibrium conditions around the few millimetres near the tissue-metal interface. Treatment planning is also hindered by the quality of imaging it is possible to achieve with large masses of metal in the field of view. Streaking artefacts and greater attenuation reduce the quality of CT images and make delineation and contouring of structures more difficult.

The use of high energy radiotherapy beams on patients with implanted materials carries the additional risk of neutron activation of the implanted material. Metallic objects typically have a high cross section

for neutron activation. It is also possible that incident x-rays of high enough energy could also produce more neutrons from within the patient. Prostheses are typically avoided in treatment planning to prevent attenuation of the dose kernel before it reaches the target, however the beam may be allowed to pass through a prosthesis on exit from the patient. Neutrons are not effectively collimated by the treatment beam shaping components, meaning that even prostheses kept outside of trajectories of any beams may be exposed to neutron radiation, and activated. Depending on the number of MU and the geometry of the irradiation, the dose resulting from such activation is expected to be very low relative to the prescription dose and even the doses from scattered and leakage photon radiation. Prostheses directly irradiated by high energy beams and secondary neutrons may become more radioactive and detailed analysis of the isotopes produced, their half-lives and their quantities is required to determine the overall risk to patients.

2.4 Conclusion

This chapter presents some fundamental physics definitions and concepts which will assist the readers understanding of the ideas which follow in the remainder of the thesis. The provided introduction to photonuclear physics and radiation protection will allow the reader to fully engage with the subject matter presented by this thesis. This will allow for a deeper understanding of the significance of the following literature review and analysis of the techniques of neutron detection and their suitability for high energy radiotherapy applications. An introduction to these core concepts of radiation protection is required in order to present the reader with a thorough exploration of the direct and indirect risks resulting from neutron exposure,

3. Comprehensive evaluation of literature

3.1 Contention in literature

There is a wealth of literature pertaining to the evaluation of photoneutrons produced by high energy linacs, but there is still a high degree of uncertainty in the field. Clinics wishing to initiate advanced treatment technologies at high energies understand that there may be an increased risk due to neutron contamination. A comprehensive review of literature reveals no clear directive on the implementation of advanced high energy treatments requiring long beam times and large monitor units. Stereotactic Ablative Body Radiotherapy (SABR), Intensity Modulated Radiotherapy (IMRT), Total Body Irradiation (TBI) and Volumetric Modulated Arc Therapy (VMAT) are of particular concern from this perspective. Some clinics are cautiously proceeding with high energy treatments, while others are refraining from implementing potentially beneficial techniques from fear of the unknown neutron field (Verellen and Vanhavere 1999). Higher energy treatment fields can provide improved tumour coverage and skin sparing for deep-seated tumours (Shambira and Lazarus 2015), but clinicians are wary of implementing them because of a lack of trustworthy data to inform the magnitude of the risk posed by contaminant neutrons. Data sets supporting both points of view have been recently published. Data published by de Gonzalez *et al* (2015) shows no significant difference in the development of secondary cancers between patients treated with high and low energy radiotherapy, whereas Bednarz *et al* (2010) concluded that there was an excess risk attributable to neutron contamination.

Professor David Followill of the MD Anderson Cancer Centre, Texas and Professor Fridtjof Nüsslin of the University Hospital, Munich have debated the contaminant neutron issue in 2007 (Followill and Nüsslin). Each acknowledged the presence and potential risk posed by neutron contamination in high energy radiotherapy beams. The point of disagreement between the two authors is whether or not the benefits of using higher energy beams outweigh the risks posed by neutron contamination. Followill's argument is that as patient survival improves it becomes more important to consider the risk of untargeted dose inducing a secondary cancer later in life. Kry *et al* (2005a) have published data showing a 2 – 5 % increase in absolute risk of fatal secondary malignancy resulting from the use of high energy beams in IMRT. Nüsslin's argument focussed on the benefits of high energy treatments; deep penetration, steeper dose gradients and skin dose reduction. He rejects the increased risk of cancer attributed to the use of higher energy beams, pointing out that only around 10% of secondary cancers are radiation induced.

Without a consensus on the risk benefit analysis of high energy beams and neutron contamination, clinicians are left with a level of uncertainty regarding the safety of high energy beams particularly with IMRT, VMAT, TBI and SABR techniques. The neutron risk needs to be more accurately quantified to deliver a conclusion to the question of high energy radiotherapy.

The difficulty with accurate quantification of the neutron risk lies in the difficulty of neutron dosimetry. In the environment of a medical linear accelerator, the high photon fluence can overwhelm the response of detectors even with low photon sensitivity. The dosimetry of neutrons is further complicated by the strong energy dependence of interaction cross sections in most materials. Additionally, binding energy from target nuclei is often released during neutron interactions, and the amount is highly dependent on the target nuclide species. The lack of equivalence between neutron detectors and human tissue requires the application of a conversion factor to the response of the detector to acquire the dose to tissue under the same conditions. The difficulty arises in the energy dependence of this conversion factor.

The challenges of neutron dosimetry in the radiotherapy environment have long been recognised. [13] McCall *et al* (1979) provides a list of the difficulties in neutron measurement which have frequently led to errors in reported data. The main points are summarised here;

1. The response of detectors to the high photon flux is often ignored.
2. Assumptions made about the neutron energy spectrum, leading to incorrect values for detector efficiency when measuring fluence.
3. Assumptions made about the neutron energy spectrum, leading to incorrect interpretation of dosimeter response when measuring dose equivalent.
4. Assumptions made about the neutron energy spectrum, leading to incorrect conversion of fluence to dose equivalent.
5. Assumptions made about the inverse square relationship between the source intensity and the distance from the source. The scattered component of the neutron field is nearly uniform throughout the room and a measurement at a given distance cannot be simply extrapolated to the source strength.

Although the susceptibilities of neutron dosimetry to errors were raised as early as 1979, the main sources of uncertainty and error in neutron dosimetry remain in the assumption of neutron energy spectra. So many aspects of detector characteristics, neutron interaction cross section, and the conversion of signal to dose, rely on accurate information of the energy of the neutrons to be measured. It is impossible to correctly interpret the response of a detector without evaluating the energy dependence of the detector. To then deduce the resulting risk to tissue, the strong energy dependence of the interactions in tissue must be well understood.

3.2 Neutron detection

3.2.1 Neutron interactions in matter

Neutron detection and dosimetry is more challenging than the photon or electron case. Neutron interactions may be classified as elastic, inelastic, non-elastic, capture and spallation interactions (Auxier *et al* 1968). Neutrons elastically scattered by nuclei maintain their kinetic energy in the centre of mass reference frame, but may change direction. They impart kinetic energy in the form of recoil to the target nucleus. Inelastic scattering places the target nucleus in an exited state, often resulting in the emission of a secondary gamma-ray. The neutron is re-emitted with a different kinetic energy and direction and the excited target nucleus recoils accordingly. Non-elastic scatter refers to nuclear interactions in which a secondary particle other than a neutron is emitted. These interactions can be exothermic or endothermic, depending on the binding energies of the target nuclei and secondary particles. Neutron capture is a non-elastic interaction occurring at a low neutron energy (Alpen 1997).

Elastic and inelastic scattering interactions provide the most efficient energy exchange when target nuclei are of a similar size. The ^{1}H nucleus is the most effective example, composed of only a single proton, which is almost identical in mass to a neutron, the energy exchange from a knock on type collision is highly effective in transferring energy from the neutron to the system. Materials high in hydrogen e.g. water, are highly effective as neutron moderators, materials which “slow down” neutrons, absorbing their kinetic energy. Neutrons which have been moderated to the point of equilibrium with the surrounding medium are referred to as thermal neutrons. Neutrons are categorised into energy or temperature regimes according to their kinetic energies (shown in Table 1). The value assigned to “thermal” neutron energy is calculated from the Maxwell-Boltzmann distribution function of velocities at 293 K.

Table 1: Neutron temperature categories and their corresponding energy ranges (Carron 2006).

Neutron temperature	Energy
Cold	< 0.025 eV
Thermal	0.025 eV
Epithermal	0.025 – 0.4 eV
Cadmium	0.4 – 0.6 eV
Epicadmium	0.6 – 1 eV
Slow	1 – 10 eV
Resonance	10 – 300 eV
Intermediate	300 eV – 1 MeV
Fast	1 – 20 MeV
Relativistic	> 20 MeV

A neutron detector can be designed to measure the recoil energy deposited by neutrons as they undergo elastic or inelastic scattering. Neutrons may also interact *via* a nuclear interaction such as neutron capture or neutron absorption with the emission of another particle, such as (n,α) or (n,p) interactions. Nuclear interactions such as these can result in the release of a significant quantity of nuclear binding energy. This may result in a mismatch between the dose to the detector material and the dose which would be received by human tissue under the same conditions.

3.2.2 Neutron detectors and dosimeters

The quantity *absorbed dose* is useful because it can be measured and correlated with biological effects. Dosimetry, the measurement of dose, in the case of neutron radiation is complicated by the nuclear energy released by interactions with specific nuclei. In addition, the dose absorbed by a detector must be correlated with the dose to human tissue, which is made up of nuclei which generally differ from those found in neutron dosimeters. Neutron interactions in tissue involve a completely different set of nuclear reactions, releasing different amounts of energy, resulting in a different *absorbed dose.* The difference between the absorbed dose to the detector and the absorbed dose to tissue is dependent on the energy of the neutrons.

Alternatively, the energy deposited in a detector material can be interpreted in terms of the incident neutron fluence, and operated therefore as a *detector* rather than a *dosimeter*. The incident neutron fluence can be used to determine the dose that would be absorbed by tissue under the same exposure conditions if the energy deposition profile in tissue is known. Figure 3 shows the neutron detectors and dosimeters used in the reviewed literature to evaluate the photoneutron contamination from high energy medical linear accelerators. A summary of the advantages and disadvantages of each detector is given in Table 2.

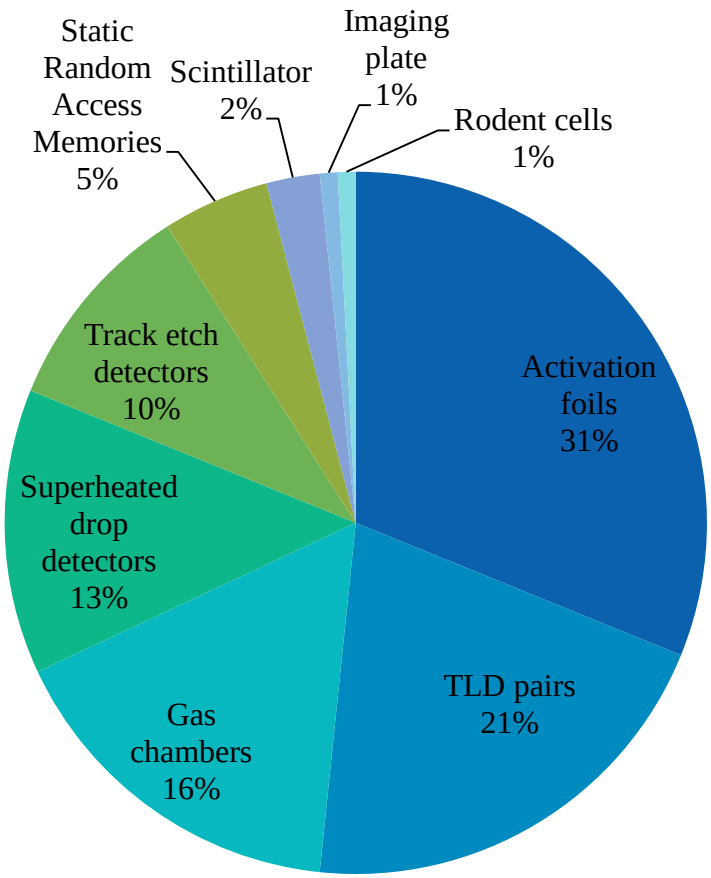

Figure 3: The popularity of various neutron detectors and dosimeters for the evaluation of photoneutrons produced by medical linear accelerators from 130 reviewed publications from 1973 to 2015.

Activation foils can be used to determine neutron fluence. The induced activity is related to the neutron cross section (interaction probability) and the fluence of incident neutrons. It is thus possible to calculate the neutron fluence from the measured activity of a sample exposed to a neutron source. Gold, indium and aluminium are commonly used as they have high neutron cross sections and half-lives ranging from minutes to hours for convenient read out time.

Thermoluminescence dosimeters (TLDs) are commonly used for radiotherapy dosimetry. Manufacturing TLDs from materials with differing neutron interaction cross sections provides a means for distinguishing between the thermoluminescence caused by photon radiation and that caused by neutron radiation. Lithium fluoride TLDs enriched in ^{6}Li and ^{7}Li used in pairs are ideal for this application.

Gas filled chambers, such as ionization chambers, proportional counters, Geiger-Müller tubes, and recombination chambers collect charge formed within the gas following radiation interactions. To measure neutrons this charge must be caused by secondary radiation formed following a neutron interaction. The walls of such chambers are often lined with boron to produce secondary alpha particles or a similar material with a high neutron cross section. They can be used paired with a chamber manufactured from low neutron cross section material and used in pairs to discriminate between photon and neutron doses (Fujii *et al* 2011).

Superheated drop detectors or bubble detectors are composed of materials in which gas bubbles are compressed into a superheated liquid. The liquid decompresses into macroscopic gas bubbles when exposed to neutrons (d'Errico 1999). They are particularly attractive to radiotherapy applications because they are insensitive to x-ray and electron radiation. The chemical composition of the detector

can be varied to produce detectors sensitive to neutrons of various kinetic energies. These can be used in conjunction to acquire information about neutron energy spectra (Apfel and d'Errico 2002).

Track etch detectors utilise the physical damage caused by neutrons incident on materials. Neutrons incident on the material cause "damage tracks" which can be chemically developed or electrochemically "etched" to improve visibility. In practise track etch detectors are usually combined with a radiator material, depending on the energy regime of the neutrons to be measured. Thermal neutrons are usually captured with a material such as lithium or boron, whereas polyethylene can be used for intermediate or fast neutrons (Fiechtner and Wernli 1999). The radiator material produces high energy recoil ions and these can inflict damage on the detector material. The tracks can be counted using commercially available automatic readers in which light transmission through the material is measured (Tanner *et al* 2005).

Neutrons incident on microelectronic devices may cause single event upsets and single-word multiple-bit upsets in static random access memories (Johansson *et al* 1999). The number of upsets can be correlated with the incident neutron fluence. The rate of occurrence of upsets is dependent on the incident neutron energy spectrum.

Scintillation detectors can be used to measure neutrons through the secondary charged particles produced by their interactions. Organic materials are often used because of their high hydrogen content which moderates the incident neutron energy spectrum and produces recoil protons. The scintillation material can also be doped with a high neutron cross section material such as lithium-6 or boron-10 to produce secondary alpha particles, which are then detected (Fischer *et al* 2006). Time-of-flight measurements can be used to provide energy spectra of the incident neutrons.

Imaging plates or radiochromic films have a low sensitivity to neutrons, but can be combined with a layer of conversion material such as boron-10 or lithium-6 which "converts" the incident neutrons into charged particles which can be more easily detected (Takahashi *et al* 1996).

Direct measurement of the biological effect caused by neutron irradiation is perhaps the least convoluted method for assessing the risk posed by neutron radiation. *In vitro* rodent cells have been used to quantify neutron effective dose in high energy radiotherapy (Hall *et al* 1995). However, there is a high degree of uncertainty in this technique because of the photon sensitivity of the cells and the inherent variations in biological processes leading to development of malignancies. There are also inherent differences between *in vivo* and *in vitro* results as well as the added complication of transferring a rodent model of radiation damage to a human biological system.

Although not neutron detectors in their own right, Bonner spheres are frequently used in neutron measurement. Polyethylene spheres of various diameters moderate neutrons to different degrees. By measuring the neutron fluence at the centre of different spheres using one of the aforementioned detectors, information about the energy spectrum of incident neutrons is obtained. The neutron spectrum is obtained by iterative "unfolding" from an initial "guess" spectrum, the accuracy of which has been tested by Vega Carrillo and Iñiguez de la Torre (2002).

A summary of the advantages and disadvantages of the heretofore described detectors are summarised in the following table.

Table 2: Summary of neutron detectors which have been used for measuring neutron contamination in high energy radiotherapy.

Detector	**Advantages**	**Disadvantages**
Activation foils	• Small in size, high resolution measurements can be made. • Photon insensitive, depending on the material chosen. • Reusable, following decay to background.	• Cross section dependence on neutron energy spectrum. • Secondary detector such as gamma spectroscopy system required. • Absolute efficiency for gamma detection must be determined.
TLD pairs	• Small in size, high resolution measurements can be made. • Reusable after annealing at high temperatures.	• Cross section dependence on neutron energy spectrum. • Photon sensitivity.
Gas chambers	• Familiar • Reusable. • Can be manufactured from "tissue equivalent" gas, such as methane.	• A 'conversion material' is required to convert the neutral neutron particles into ionising particles. • The interaction with the conversion material is energy dependent. • These detectors generally have a low efficiency.
Superheated drop detectors	• Can be specifically formulated to be sensitive to different energy regimes. • The gas bubbles can be recompressed for a reusable detector. • Bubbles can be automatically counted by an automatic reader.	• Manual counting of bubbles is time intensive. • Available energy regimes for customised sensitivity are coarse, and spectral information is not easily acquired. • Coarse spatial resolution.
Track etch detectors	• Small in size, high resolution measurements can be made. • Photon insensitive.	• Manual counting of tracks is time intensive. • Low sensitivity. • A 'conversion material' is required to convert the neutral neutron particles into ionising particles. • The interaction with the conversion material is energy dependent.
Static random access memories	• Photon insensitive. • Real time response.	• Low sensitivity. • Sensitivity is dependent on the neutron energy spectrum.

Scintillators	• Time-of-flight measurements can provide spectral information.	• Low efficiency. • Photon sensitive.
Imaging plate	• Can provide high resolution 2D information.	• A ‘conversion material’ is required to convert the neutral neutron particles into ionising particles. • The interaction with the conversion material is energy dependent.
Rodent cells	• Provides a direct measure of the biological damage inflicted.	• Requires facilities and expertise to culture and analyse cells. • Sensitive to photon radiation.

3.2.3 Choice of detector

To evaluate the risk posed by neutron contamination in high energy radiotherapy, neutron dosimetry in mixed γ-n fields is necessary. Radiotherapy linacs are designed to produce a very high fluence of x-rays which dwarfs the small fluence of contaminant neutrons produced. This presents challenges for neutron detection and dosimetry. A suitable detector and robust dosimetric methodology is required to achieve accurate results in the presence of the high x-ray fluence.

Ideally, neutron detectors for use with medical linear accelerators require a high sensitivity to neutrons and little or no sensitivity to x-ray or electron radiation. If detectors are not insensitive to x-rays, there needs to be a way to determine the proportions of the detector response caused by x-rays and caused by neutrons.

In an ideal world, detector response would not change with the energy of the neutrons. Neutron interaction cross sections for detector materials are always dependent on the energy of the neutrons to some extent. However, if the form of the energy dependence is relatively simple, an accurate result can be obtained without detailed information about the neutron energy spectrum of interest.

To achieve good spatial resolution, detectors should be as small as practicable. Spatially resolved dose information is necessary to evaluate the risk to patients. If *in vivo* neutron measurements such as those published by Lonski, Keehan *et al* (2017) are to be performed, it is useful if detectors are small, free of wires and do not perturb the treatment beams. If the detectors are required to be measured or "read out" following irradiation by neutrons it is important that the read out technique is reliable and practical. It is cost effective and convenient if detectors are reusable.

Table 3 gives a summary of these properties for the detectors discussed in §3.2.2. Activation foils and TLDs offer many of the desirable properties described above. The primary advantage of activation foils for radiotherapy applications is their insensitivity to photons. Activation foils are almost always photon insensitive, except for some materials like gold which can be activated by high energy photons as well as neutrons. The method for quantifying the neutron fluence from the activity of an exposed material can be derived from the first principles of radioactive decay. They are easy to read out following irradiation and can be reused following decay of the radioactive products produced, which can be quite soon after irradiation depending on the half-life of the isotope produced. The activation material can be chosen to optimise the parameters required for the intended use. High cross section materials can be chosen for a more sensitive detector, short half-life materials for faster read out and reusability. More abundant elements can be chosen for a cost effective solution. This makes them a dynamic and flexible choice of detector.

TLDs are well characterised for use as x-ray dosimeters. Protocols for measuring light emitted following irradiation and annealing at high temperatures are established in many radiotherapy departments. In radiotherapy their sensitivity to photons is a disadvantage for neutron dosimetry, however the availability of TLD materials enriched in specific isotopes, which can be used in pairs allows for distinction between the detector response caused by photons and by neutrons. Their existing common usage as *in vivo* dosimeters attests to their advantages in radiotherapy applications, their small size, reliability and accuracy are all benefits which apply also to their properties as neutron detectors.

Table 3: Summary of neutron detectors and their properties

Detector	**Photon sensitive**	**Read out**	**Reusable**	**Spatial resolution**	**Real time**	**Peripherals (cables etc.)**
Activation foils	No – material dependent	Gamma-ray spectroscopy	Yes – half-life dependent	Centimetres	No	None
Thermoluminescence dosimeters	Yes	Automatic TLD reader	Yes – annealed at high temperature	Millimetres	No	None
Superheated drop detectors	No	Light transmission	Yes – bubbles re-compressed	Centimetres	No	None
Track etch detectors	No	Light transmission	No	Centimetres	No	None
Ion chambers	Yes – material dependent	Charge collection	Yes	Centimetres to tens of centimetres	Yes	Yes

3.3 Activation foils

Enrico Fermi (1934) first reported on the production of radioisotopes following interaction with neutrons. He produced neutrons by bombarding beryllium powder with alpha particles. He observed radioactivity in aluminium and fluorine which remained even after the neutron source was removed. The amount of induced activity is related to the neutron cross section (interaction probability) and the fluence of incident neutrons. It is thus possible to calculate the neutron fluence from the measured activity of a sample exposed to a neutron source.

To accurately calculate the neutron fluence the sample and detector must be characterised. The isotopic fractional composition of the sample must be known. From this, the number of target nuclei can be calculated and the neutron interaction cross section for a given neutron energy spectrum can be determined. The total efficiency of the detector is needed to convert the number of detections to the absolute activity of the sample. The efficiency of the detector depends on the physical geometry of the source-detector arrangement as well as the type and energy of emissions emanating from the activated sample. The irradiation time, counting time and any cool off period in between are needed to correct for the decay of the activated sample.

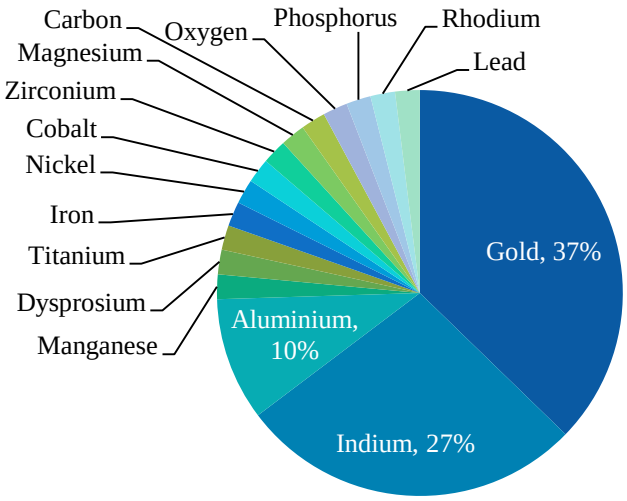

Figure 4: The relative popularity of activation foil materials for the measurement of photo-neutrons produced by medical linear accelerators as determined by literature review of peer reviewed work published between 1976 and 2015.

The materials used for neutron measurements in high energy radiotherapy are shown in Figure 4. Gold, indium and aluminium are the three most popular materials. These materials have relatively high cross sections for neutron capture interactions (see Figure 5) and half-lives ranging from minutes to days for convenient irradiation and measurement times (see Table 4). The detector used to measure the activity must be characterised so that the intrinsic efficiency of each emission energy of the activated isotope can be accounted.

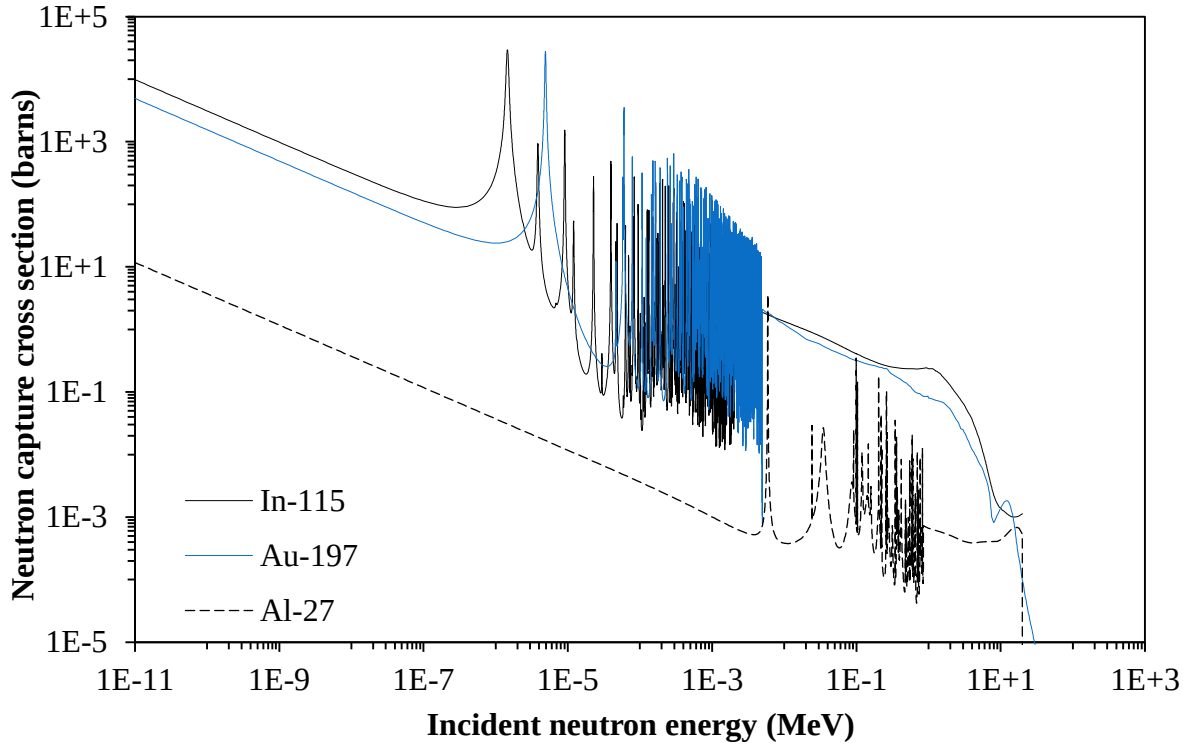

Figure 5: Neutron capture cross sections for the three most popular activation foil materials; ^{115}In, ^{197}Au and ^{27}Al (Chadwick *et al* 2011).

Table 4: Properties of the three most popular activation foil materials; ^{115}In, ^{197}Au and ^{27}Al.

Sample material	**Naturally occurring isotopes**	**Isotopic abundance** [1]	**Interaction**	**Emissions of activated isotope**	**Half-life of activated isotope**
Indium	^{113}In ^{115}In	4.29 % 95.71 %	$^{115}\mathrm{In} + \mathrm{n} \rightarrow {}^{116m}\mathrm{In}$	417, 819, 1097, 1294 keV γ-rays [2]	54.29 minutes [2]
Gold	^{197}Au	100 %	$^{197}\mathrm{Au} + \mathrm{n} \rightarrow {}^{198}\mathrm{Au}$	412 keV γ-rays [3]	2.6947 days [3]
Aluminium	^{27}Al	100 %	$^{28}\mathrm{Al} + \mathrm{n} \rightarrow {}^{29}\mathrm{Al}$	1179 keV [4]	2.245 minutes [4]

[1] Rosman and Taylor (1999), [2] Blachot (2010), [3] Xiaolong (2009), [4] Basunia (2013)

One of the main advantages of activation foils as a neutron detector for radiotherapy dosimetry is that they are typically photon insensitive. They can be manufactured as thin foils with small dimensions, to offer negligible perturbation of the neutron fluence and allow the potential for high resolution spatial data. They are easy to use provided there is a detector available to measure the absolute activity following irradiation. They are reusable, provided enough time is allowed for the sample to decay.

The limitation of using activation foils to quantify neutron fluence is the high uncertainty. The cross section for neutron activation in most materials varies strongly with the energy of the incident neutron fluence. The cross section is highest at lower neutron energies, decreasing as the neutron energy increases. There are nearly always a complex series of resonance peaks such as those seen in Figure 5, which make it difficult to select an accurate single value for the interaction probability. The more accurately the neutron energy spectrum is known, the more accurately the net cross section can be

determined. The neutron energy spectrum usually has an associated high degree of uncertainty, as it can only be determined from Monte Carlo modelling or de-convolution of Bonner sphere measurements. Another limitation of using activation foils in a clinical setting is the need for a detector which can measure absolute activity with a low uncertainty. Gamma spectroscopy with either a sodium iodide (NaI) or a high purity germanium (HPGe) detector is commonly used to measure the activity of activation foil samples. NaI detectors are typically higher efficiency where HPGe can offer higher resolution. For measuring low activity samples lead shielding is often employed around the detector to reduce the detection of background radiation.

3.4 Thermoluminescence dosimeters

Thermoluminescence dosimeters (TLDs) are commonly used for the dosimetry of photons and electrons in radiotherapy. TLDs are crystalline materials containing dopants which form electron traps. Incident radiation causes the transfer of an electron into a trap, where it remains until heat is applied to release it. When heat is applied the electrons return to the valence band emitting photons. The output photons are measured and the charge they produce in a photomultiplier tube is collected. The charge collected is directly proportional to the energy absorbed from incident radiation (McKeever *et al* 1995).

Lithium fluoride is a widely used TLD material for photon and electron dosimetry. There are two naturally occurring isotopes of lithium: ^{6}Li (7.59%) and ^{7}Li (92.41%). TLDs can be manufactured from lithium fluoride enriched in either of these two isotopes. ^{6}Li and ^{7}Li have differing neutron interaction cross sections (see Figure 6) which result in different responses in TLDs enriched in either isotope. TLDs enriched in ^{6}Li or ^{7}Li are also sensitive to photon and electron radiation and their total response is the sum of the responses caused by each radiation type (Spurný *et al* 1976). In this work LiF TLDs doped with magnesium, copper, and phosphorus have been used, because they have higher sensitivity than the traditionally available magnesium-titanium doped LiF TLDs. This allows them to be used out-of-field for *in vivo* dosimetry of low doses as published in Lonski, Keehan *et al* (2017).

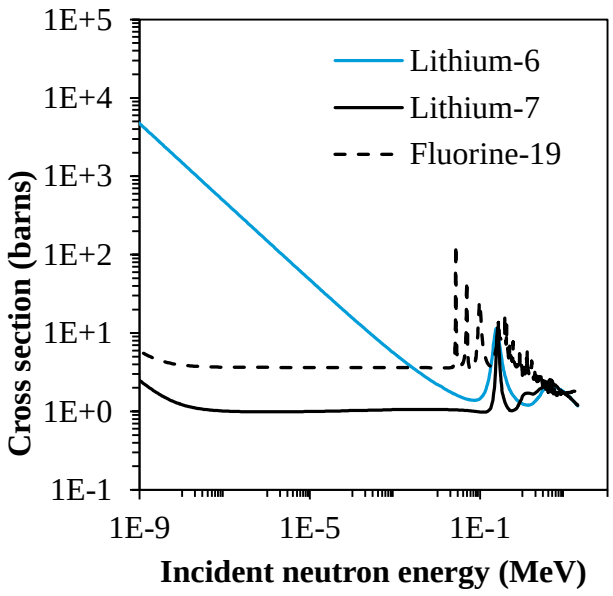

Figure 6: The total neutron interaction cross sections (Chadwick *et al* 2011) for lithium-6, lithium-7 and fluorine-19, the only naturally occurring isotopes of lithium and fluoride (Rosman and Taylor 1999).

Most publications using LiF TLDs enriched in ^{6}Li and ^{7}Li state that ^{6}LiF TLDs are sensitive to both neutron and photon radiations and that ^{7}LiF TLDs are sensitive to photon radiation only (Barquero *et al* 2002, Chu *et al* 2011, Esposito *et al* 2008, Gregori *et al* 2002). It follows that if the photon sensitivity of each material is identical; the component of the response caused by incident neutrons is the difference

between the responses of each material irradiated together. However, the responses of the two materials are dependent on the energy of the incident neutrons.

Figure 6 shows the total neutron cross sections for ^{6}Li, ^{7}Li and ^{19}F. The probability of neutron interaction with ^{6}Li is ~ 5000 barns compared to ~ 2.5 barns in ^{7}Li for 1 meV neutrons (Chadwick et al 2011). However at higher energies, the cross sections of ^{6}Li and ^{7}Li don't differ a great deal, and the resonance peaks in the ^{19}F cross section begin to dominate. The energy deposited by a neutron which does interact with one of these three nuclei varies depending on the type of interaction which takes place (Spurný et al 1976, Tanaka and Takeuchi 1975). The dominating mode of neutron energy deposition in LiF TLDs is the (n,α) interaction with ^{6}Li, which has a Q value of 4.78 MeV.

The challenge of using TLDs for neutron dosimetry arises from this energy dependence. The validity of taking the difference between the responses of paired ^{6}LiF and ^{7}LiF TLDs is justifiable only at low neutron energies. Calibration of the TLD response to a given dose delivered by a standard neutron source of a given energy spectrum is only valid for measurements taken under an identical energy spectrum. Assuming ^{7}LiF insensitivity at higher neutron energies results in underestimation of the calibration factor, and therefore underestimation of the dose to be measured.

Glow curve analysis can be a useful mechanism for distinguishing between photon and neutron exposures for LiF:Mg,Ti materials. There is an interesting paper by Youssian and Horowitz (1998) which demonstrates a method for using glow curve analysis, specifically peak 4 to peak 5 ratios, to determine gamma dose for mixed field irradiations. However, the technique is only useful for scenarios where the gamma dose is less than 10% of the total dose, which is not usually the case in high energy radiotherapy. Salah *et al* (2007) provide a comparison of the glow curves of LiF:Mg,Cu,P, LiF:Mg,Ti, and 7LiF:Mg,Cu,P. The Mg,Cu,P doped TLD materials have a much simpler structure than the Mg,Ti doped TLDs, with only a single prominent dosimetry peak which is proportional to the exposure dose. This makes glow curve analysis less useful for the Mg,Cu,P materials which were used in this thesis. The advantage of using the newer Mg,Cu,P material is their higher sensitivity, which was useful for measuring doses outside the primary photon field of the linac.

However, TLDs offer many advantages for radiotherapy dosimetry. Small and wireless, with a robust readout and annealing technique well established, they are commonly used for photon and electron dosimetry. Radiotherapy clinics often employ TLDs for routine dosimetry and many clinics have the capability to use, read and anneal these dosimeters. The use of TLDs for neutron dosimetry is complicated by their energy dependence and release of nuclear binding energy. If these can be properly accounted for, TLDs have potential as a promising tool for evaluating neutron risks in radiotherapy.

3.5 Conclusion

This chapter has provided an up-to-date evaluation of the relevant issues caused by neutron production in high energy radiotherapy. Although this has been the subject of scientific study for many years, there is by no means a consensus amongst experts. In order to begin addressing the challenge, a broad introduction is given covering a variety of neutron detectors and a deeply considered and extensive analysis of the properties of each detector is given. A discussion of the advantages and disadvantages of each detector type for use in the context of high energy radiotherapy is used to explain the choice of detectors used in this thesis. Finally a detailed discussion of the underlying physics for two specific detectors is given so that the reader may be prepared for the development of a robust methodology for calibration and use presented in the following chapter.

4. Methods for neutron detection and dosimetry

In order to determine the risk resulting from contaminant neutrons in high energy radiotherapy, the degree of neutron contamination must be quantified. The density of neutrons in a given area is known as the *fluence*, ϕ. The *flux* is the rate at which neutrons pass through an area. Fluence and flux are often used interchangeably in peer reviewed publications to describe the quantity which is technically the *fluence rate* or *flux density* with units of $cm^{-2} \cdot s^{-1}$. The simplest quantification of a neutron field is the fluence rate, which simply provides a measure of the number of neutrons. This cannot be directly related to the risk posed by a given neutron field and thus the quantity *dose* is needed. The absorbed dose, *D*, deposited in a material is the energy absorbed per unit mass of the material. The equivalent dose, *H*, is weighted to account for the different amount of damage done by different radiation types depositing the same amount of energy.

The measurement of neutrons is far more complex than the measurement of photon or electron dose which are more commonly required in radiotherapy. Thermoluminescence dosimeters (TLDs) are often used for routine dosimetry in medical physics. Selection of specific isotopes for use in the manufacture of TLDs allows neutron sensitivity to be enhanced or diminished to provide means for quantification of the neutron field, but not necessarily the quantity of interest, dose equivalent. Activation foils are a common method of neutron fluence measurement in which the amount of activation produced in a material can be used to calculate neutron fluence. Conversion of a measured neutron fluence to an absorbed dose or dose equivalent requires calculation of the energy deposited in tissue for a given neutron fluence. This conversion is strongly dependent on the energy distribution of the neutron fluence, and so the energy spectrum is also required.

Whilst this chapter is primarily a "methods" chapter, some results are included to support the techniques chosen to acquire the bulk of results obtained in later chapters of this thesis. The development of robust methodology for neutron detection in mixed γ-n fields is presented here. This requires interpretation of the responses of ^{6}Li and ^{7}Li enriched LiF TLDs irradiated in pairs and the response of irradiated activation foils. To evaluate risk, absorbed dose or dose equivalent is the quantity of interest and for this the energy spectrum of the neutrons to be measured is required, which is obtainable from accurate Monte Carlo modelling of the measurement scenario.

4.1 Lithium-6 and lithium-7 enriched lithium fluoride dosimeters

Lithium fluoride thermoluminescence dosimeters (TLDs) are well established for measuring x-ray doses (Kron 1999). Lithium has two naturally occurring isotopes; ^{6}Li (7.59 %) and ^{7}Li (92.41 %) (Rosman and Taylor 1999), which have extremely different neutron interaction cross sections (see Figure 6). LiF TLDs can be manufactured from material enriched in either isotope and have very different probabilities for neutron interaction. The responses of ^{6}LiF and ^{7}LiF TLDs exposed to neutrons reflect the difference in probability of interaction.

For low energy neutrons, the cross section for ^{6}Li greatly exceeds that of ^{7}Li. Thermal neutrons with kinetic energy of 2.53×10^{-2} eV have a total interaction cross section of 939 barns with ^{6}Li and only 1.09 barns with ^{7}Li. For ^{6}LiF and ^{7}LiF TLDs exposed to a mixed γ-n field where the neutrons are low energy neutrons only, the component of the response caused by the neutron radiation only, R_n, can be determined from the difference in response between a ^{6}LiF and ^{7}LiF TLD exposed together (see equation 2). I.e. ^{7}LiF TLDs are insensitive to thermal neutrons.

$$R_n = R_{^{6}LiF} - R_{^{7}LiF} \qquad [2]$$

4.1.1 Neutron interactions with ^{6}Li, ^{7}Li and ^{19}F

As well as differing interaction probabilities, there are also differences in the types of interactions which occur between the incident neutrons and the three isotopes present in the LiF TLDs (see Table 5). These interactions are predominantly endothermic, with the exception of the ^{6}Li(n,αt) reaction which is exothermic with a Q value of +4.78 MeV. Despite the prevalence of endothermic interactions, all these interactions cause a net release of kinetic energy when the incident neutrons have sufficient kinetic energy.

Table 5: Neutron interactions which occur with ^{6}Li, ^{7}Li and ^{19}F nuclei.

^{6}Li	**^{7}Li**	**^{19}F**
Elastic scatter [1,2]	Elastic scatter [1,2]	Elastic scatter [1,2]
Inelastic scatter [1,2]	Inelastic scatter [1,2]	Inelastic scatter [2]
(n,ndα) [1,2]	(n,nαt) [1,2]	(n,p) [1,2]
(n,2n) [1,2]	(n,2n) [1,2]	(n,α) [1,2]
(n,p) [1]	(n,2nαd) [1,2]	(n,2n) [2]
(n,αt) [1,2]	(n,d) [1,2]	
(n,2npα) [2]		

[1]Interaction included by Tanaka and Takeuchi (1975) [2]Interaction included by Spurný *et al* (1976)
n is a neutron, *p* is a proton or ^{1}H nucleus, *d* is a deuteron or ^{2}H nucleus, *t* is a triton or ^{3}H nucleus and *α* is an alpha or ^{4}He nucleus.

The papers by Tanaka and Takeuchi (1975) and Spurný *et al* (1976) each posit that the response measured from TLDs is directly proportional to the kerma, *K*, released by neutrons of specific energies, E_n, in the material. Thus, the ratio of the responses caused by neutrons in two TLD materials will be equal to the ratio of the kerma deposited by neutrons of a given energy in the materials.

$$\frac{R_{^{6}LiF,n}}{R_{^{7}LiF,n}} = \frac{K_{^{6}LiF,n}}{K_{^{7}LiF,n}} \qquad [3]$$

The average kerma per neutron can be calculated using equation 4 for each of the interactions shown in Table 5. The kerma, *K*, is the sum of the mean energy ε_{lji} released by interactions with nuclear species *l*, by interactions *j*, with interaction products *i* multiplied by the cross section σ_{lj} for that interaction. This is then multiplied by the number of nuclei N_l and summed over all nuclear species present.

$$K(E_n) = \sum_l N_l \sum_j \sum_i \overline{\varepsilon_{lji}(E_n)} \cdot \sigma_{lj}(E_n) \qquad [4]$$

The neutron interactions are considered to take the form;

$$n + l \rightarrow i + i' \qquad [5]$$

Where *n* is the incident neutron, *l* is the target nucleus, *i* interaction product whose energy is being calculated and *i'* is the sum of the remaining interaction products.

For elastic scatter neutron interactions, the kinetic energy of the neutron is unchanged (in the centre of mass reference frame), but its velocity vector may change direction, causing recoil of nuclei in the TLD material. The average recoil energy can be calculated from simple kinematics (see equation 6) if the neutron energy is below relativistic. A neutron velocity of 10% of the speed of light corresponds to a neutron kinetic energy of 9.26 MeV, so neutrons below this can be considered non-relativistic (Walker 2008). Some sample neutron energy spectra produced by linacs will be presented in §4.1.4, for now, consider a mean neutron energy of about 0.5 MeV. This corresponds to only ~3 % of the speed of light and may be safely considered non-relativistic.

$$\overline{\varepsilon_{lji}(E_n)} = \frac{2m_n m_i}{(m_n + m_i)^2} \cdot E_n \cdot \left(1 - \overline{\cos\theta}\right) \qquad [6]$$

Equation 6 gives the average recoil energy from elastic scatter of neutrons where *l*, is the target nucleus which scatters the neutron, *n*, and *i*, the interaction product will be the neutron. θ is the scattering angle in the centre of mass reference frame. Equation 7 gives the average energy released by an *inelastically scattered neutron*. *Q* is the excitation energy of the scattered nucleus (given in Table 6).

$$\overline{\varepsilon_{lji}(E_n)} = \frac{2m_n m_i}{(m_n + m_i)^2} \cdot E_n + Q \qquad [7]$$

Table 6: The Q values for inelastic scatter of neutrons with ^{6}Li, ^{7}Li and ^{19}F nuclei (Spurný *et al* 1976).

Nucleus	**Q (MeV)**
^{6}Li	-3.560
^{7}Li	-0.478
^{19}F	-0.109

The average energy deposited by the other interactions which release charged particles is given by equation 8;

$$\overline{\varepsilon_{lji}(E_n)} = \frac{m_n m_i + m_l m_{i'}}{(m_n + m_l)(m_i + m_{i'})} \cdot E_n + \frac{m_{i'}}{m_n + m_l} Q \qquad [8]$$

The mean energy must be calculated separately for each charged particle *i* produced by the interaction, where *i'* is the sum of the other products of the interaction. For example, in the interaction ^{6}Li(n,α)t, there are two charged interaction products; the alpha particle and the triton. The mean energy of the alpha and of the triton must be calculated separately using equation 8 and summed in equation 4.

Applying equations 4 – 8 to the interactions given in Table 5 gives the kerma in MeV/g per incident neutron of a given energy. This can also be calculated using Monte Carlo radiation transport modelling. To validate the analytical method used in this study MCNP6 has been used to model 3 × 3 × 1 mm^3 TLD

chips composed of ^{Nat}LiF, ^{6}LiF and ^{7}LiF. A spherical source (Ø = 1 cm) of isotropic monoenergetic neutrons was placed 10 cm from the TLDs. The total energy deposition averaged over a cell and the neutron fluence averaged over the cell were scored and these results were used to calculate the dose deposited per incident neutron. The MCNP6 results are obtained from standard tally 4, which scores the average flux over a cell in particles/cm^2 and standard tally 6+ which scores the total heating over a cell in (MeV/g). The kerma per incident neutron is the tally 6+ result divided by the tally 4 result. The ENDF/B-VII.1 Release 0 was used for all simulations throughout this work.

4.1.2 Kerma in ^{Nat}Li, ^{6}LiF and ^{7}LiF

The results of the analytical method of calculating the kerma per neutron (using equations 4 – 8) are shown in Figure 7. A constant ratio between ^{6}LiF and ^{7}LiF is apparent below ~ 2 keV. Above this energy the resonance peaks in the ^{19}F elastic scatter cross section begin to dominate. The ^{6}Li and ^{7}Li resonance peak at ~ 220 keV is also an obvious feature. There is a sharp rise in the kerma in ^{6}LiF at around 4 MeV. There is clearly strong energy dependence in the kerma released in ^{6}LiF and ^{7}LiF TLDs exposed to neutrons. To validate these calculations, the dose per neutron in TLD materials has also been modelled using MCNP6. The dose in the three TLD materials is calculated for a number of monoenergetic neutron sources and the results are shown in Figure 8. The difference between the two calculation methods is shown in Figure 9. There is approximately a 50 % mismatch between the two data sets around the ^{19}F elastic scatter resonances. The main difference comes from the absence of the steep increase above 4 MeV in the MCNP6 calculated results.

This arises from the physical differences between the quantities calculated. The analytic calculation determines the kerma, kinetic energy released to mass, whilst the Monte Carlo model determines the energy deposition averaged over the cell. The cell in this case was a 3 × 3 × 1 mm^3 TLD chip. In the analytical calculation any interactions within the cell, which release energy are counted toward the total. In the Monte Carlo simulation only those interactions which result in energy being deposited within the cell contributed. The larger values in Kerma seen above 4 MeV indicate energy which has been released within the cell, but where the dose is deposited outside of the volume. The Monte Carlo simulation accurately reflects this. Kerma is approximately equal to dose under some circumstances, where the energy of the radiation is sufficiently low and charged particle equilibrium is valid. For TLD chips of 3 × 3 × 1 mm^3 kerma is equal to dose only for neutron radiation below 4 MeV.

The analytic method of calculation is much less computationally demanding (in the order of one second compared to one day) and is sufficiently accurate for neutron energies below about 4 MeV. This could potentially be advantageous in provided a quick analytical estimate for the energy dependence of TLDs rather than full scale Monte Carlo modelling, which may be time consuming.

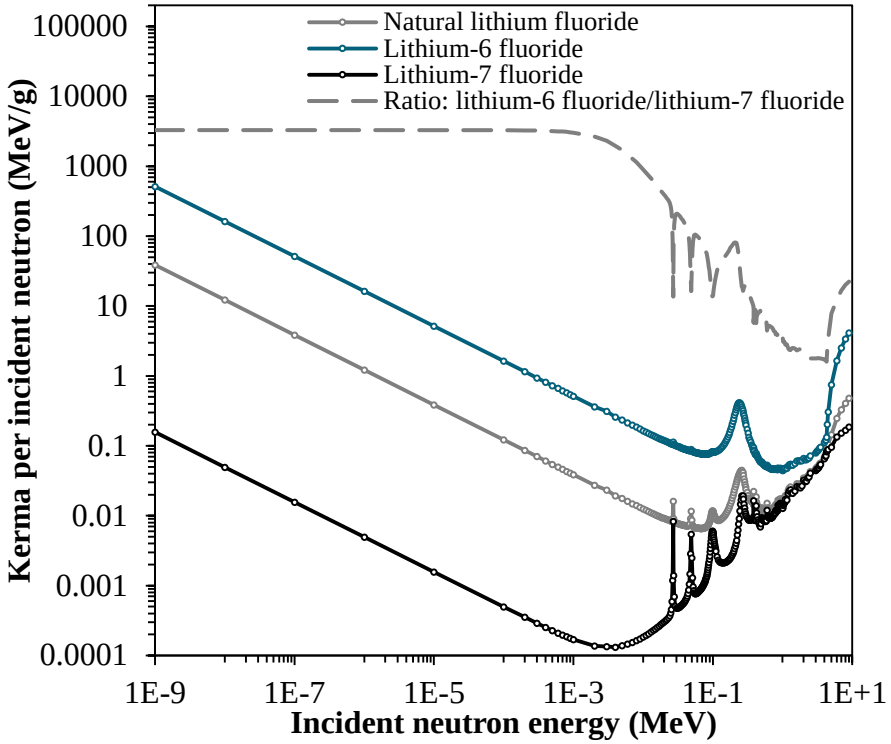

Figure 7: The kerma per incident neutron in ^{Nat}LiF, ^{6}LiF and ^{7}LiF calculated analytically using equations 4 – 8 for the reactions given in Table 5.

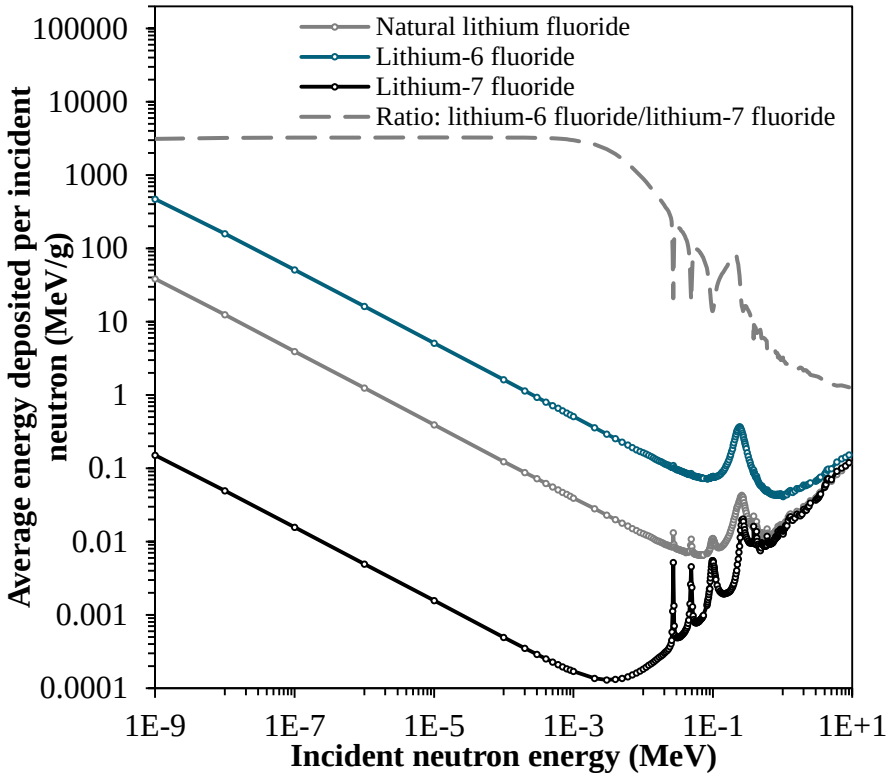

Figure 8: The average energy deposited per incident neutron in ^{Nat}LiF, ^{6}LiF and ^{7}LiF calculated using MCNP6 total heating tally t6+ and neutron fluence tally 4.

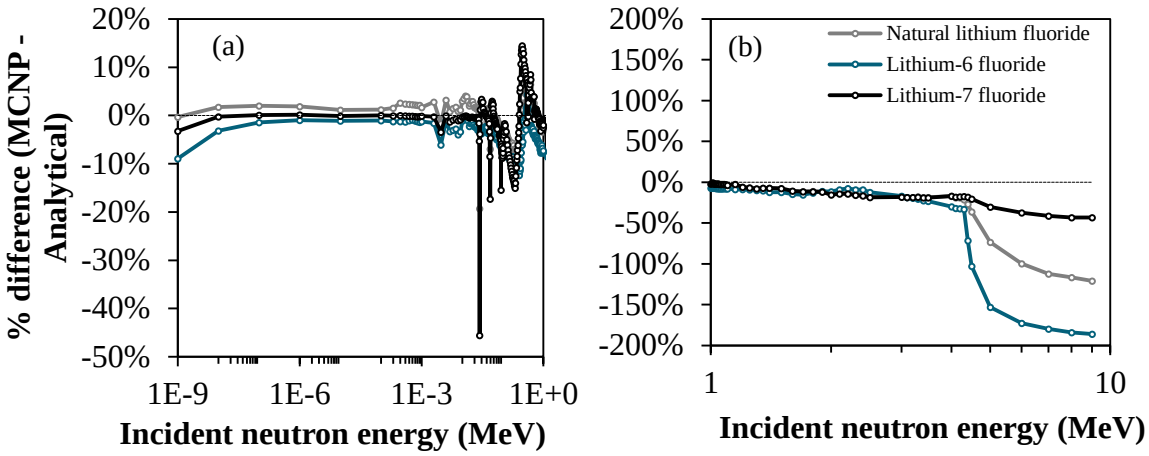

Figure 9: The percentage difference (MCNP minus Analytic) between the two methods of calculation. Panels (a) and (b) show different scales to illustrate the details in the data at low energies (a) and the larger discrepancy in the above about 4 MeV (b).

The TLDs used in this study were doped with magnesium, copper, and phosphorus for extra sensitivity. Previous work in the field has usually used magnesium-titanium doped LiF TLDs. The dopant materials are present in very low quantities and neutron interactions with these materials have been excluded from the above calculations due to the negligible contribution to dose absorbed in the dosimeters. The relative concentrations of all isotopes present in ^{nat}LiF, ^{6}LiF and ^{7}LiF doped with either Mg,Ti or Mg,Cu,P are given in Table 7. The cross sections for neutron interaction with each isotope are shown in Figure 10 and Figure 11. The cross section, or interaction probability, has been weighted according to the amount of material present in ^{6}LiF:Mg,Ti and ^{6}LiF:Mg,Cu,P for demonstration. The cross sections for the lithium and fluorine nuclei, which are present in the highest quantities, are several orders of magnitude higher than those of the dopants. It is assumed that interactions with the dopant materials do not present a significant contribution to the ratio of the signal read out from the TLDs following exposure to neutron radiation. The methods used in the thesis might be more difficult to apply to Mg,Ti doped TLDs because of the supralinear behaviour above 2 Gy. The Mg,Cu,P doping provides a higher signal, and has a very linear dose-response behaviour. The superior properties of this material will likely cause it to replace the older Mg,Ti materials in the future. The neutron spectra produced by medical linear accelerators are investigated in §4.1.4.

Table 7: The isotopic composition of natural and enriched LiF TLD materials for Mg,Ti and Mg,Cu,P dopants. The amount of dopant was determined from the elemental concentrations published by Bilski (2002) weighted according to their natural abundance (Rosman and Taylor 1999).

Isotope	^{nat}LiF:Mg,Ti TLD100	^{nat}LiF:Mg,Cu,P TLD100H	^{6}LiF:Mg,Ti TLD600	^{6}LiF:Mg,Cu,P TLD600H	^{7}LiF:Mg,Ti TLD700	^{7}LiF:Mg,Cu,P TLD700H
^{6}Li	3.79 %	3.7 %	47.79 %	47.08 %	0.015 %	0.015 %
^{7}Li	46.20 %	45.51 %	2.20 %	2.17 %	49.98 %	49.24 %
^{19}F	49.99 %	49.25 %	49.99 %	49.25 %	49.99 %	49.25 %
^{24}Mg	0.0095 %	0.16 %	0.0095 %	0.16 %	0.0095 %	0.16 %
^{25}Mg	0.0012 %	0.02 %	0.0012 %	0.02 %	0.0012 %	0.02 %
^{26}Mg	0.0013 %	0.02 %	0.0013 %	0.02 %	0.0013 %	0.02 %
^{46}Ti	0.0001 %	-	0.0001 %	-	0.0001 %	-
^{47}Ti	0.0001 %	-	0.0001 %	-	0.0001 %	-
^{48}Ti	0.0010 %	-	0.0010 %	-	0.0010 %	-
^{49}Ti	0.0001 %	-	0.0001 %	-	0.0001 %	-
^{50}Ti	0.0001 %	-	0.0001 %	-	0.0001 %	-
^{31}P	-	1.25 %	-	1.25 %	-	1.25 %
^{63}Cu	-	0.035 %	-	0.035 %	-	0.035 %
^{65}Cu	-	0.015 %	-	0.015 %	-	0.015 %

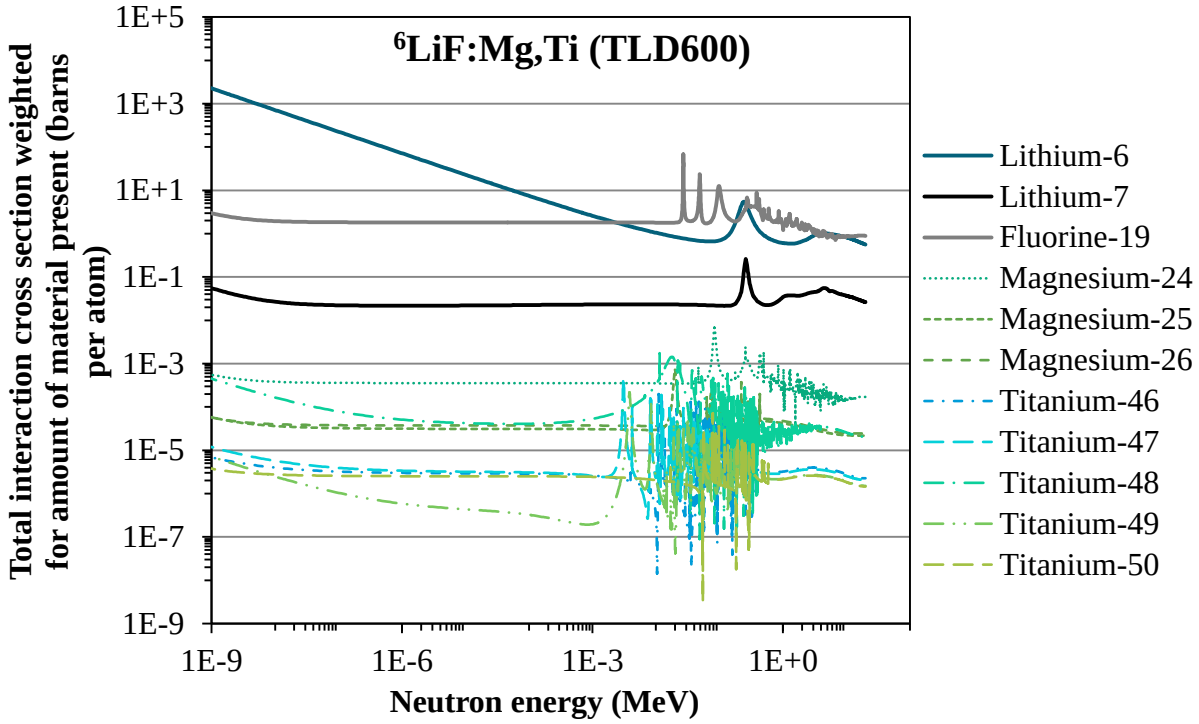

Figure 10: The neutron interaction cross sections (Chadwick *et al* 2011) for all nuclei present in ^{6}LiF:Mg,Ti, also known as TLD600, are shown. They are weighted according to the amount of each material present as shown in Table 7. The dominant materials are shown by solid lines and the dopants as dashed or dotted lines. These are not intended to be individually considered, but rather are shown to illustrate the magnitude difference in the interaction probabilities for the bulk and dopant materials.

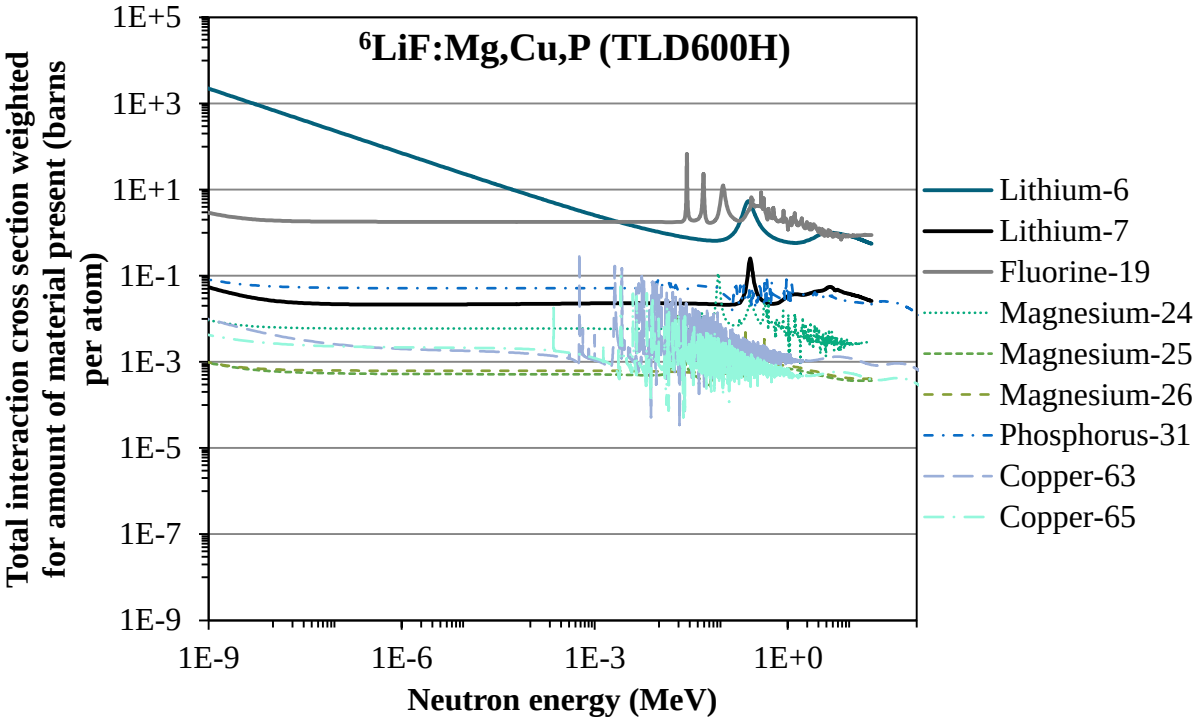

Figure 11: The neutron interaction cross sections (Chadwick *et al* 2011) for all nuclei present in ^{6}LiF:Mg,Cu,P, also known as TLD600H, are shown. They are weighted according to the amount of each material present as shown in Table 7. The dominant materials are shown by solid lines and the dopants as dashed or dotted lines. These are not intended to be individually considered, but rather are shown to illustrate the magnitude difference in the interaction probabilities for the bulk and dopant materials.

4.1.3 Calibration of ^{6}LiF and ^{7}LiF for neutron dosimetry

The energy dependence of the neutron response of TLDs has implications for their calibration and use as detectors or dosimeters. The assumption that ^{7}LiF TLDs are "insensitive" to neutrons is only valid for neutron energies below about 2 keV. Isotopic and fission neutron sources such as californium-252, americium-beryllium and americium-boron predominantly emit neutrons with higher energies (see Figure 12). The TLD response becomes more complex to interpret under these circumstances as ^{7}LiF becomes more sensitive to neutrons as the energy increases. MCNP6 has been used to calculate the average energy deposited per incident neutron in ^{nat}LiF, ^{6}LiF and ^{7}LiF from incident neutrons of the spectra shown in Figure 12 in the same geometry as described in §4.1.1. The neutron spectra produced by medical linear accelerators are presented in §4.1.4.

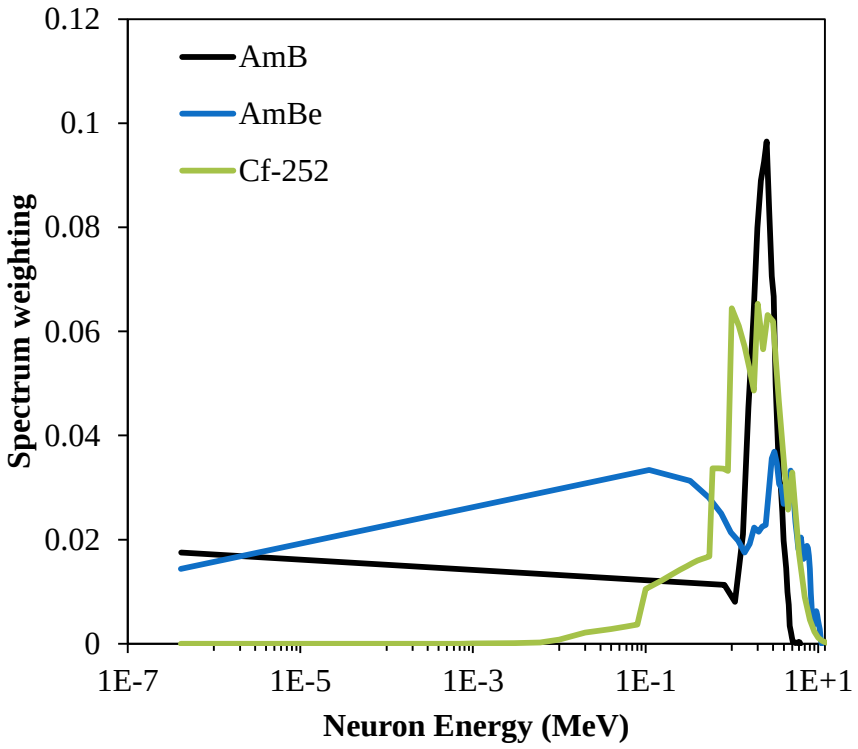

Figure 12: The neutron energy spectra of ^{241}AmB, ^{241}AmBe and ^{252}Cf neutron sources (ISO8529-1 2001).

If TLDs are given a known dose from a standard isotopic or fission neutron source, the difference between the responses of ^{6}LiF and ^{7}LiF is smaller than the proportion of the response caused by neutrons (see Figure 13). A calibration factor determined under these conditions could be overestimated by as much as 131 % (see Table 9). If the TLDs are to be used for dosimetry under the same neutron spectrum as the calibration source, the calibration factor can be applied without consideration of the energy dependence. But care should be taken that the calibration factor is only applied to measurements made under the exact same conditions as the calibration. The source should have the same energy spectrum, and the exposure geometry should also be kept constant. The presence of scattering and moderating materials has the effect of reducing the kinetic energy of the neutrons therefore changing the response behaviour of the TLDs.

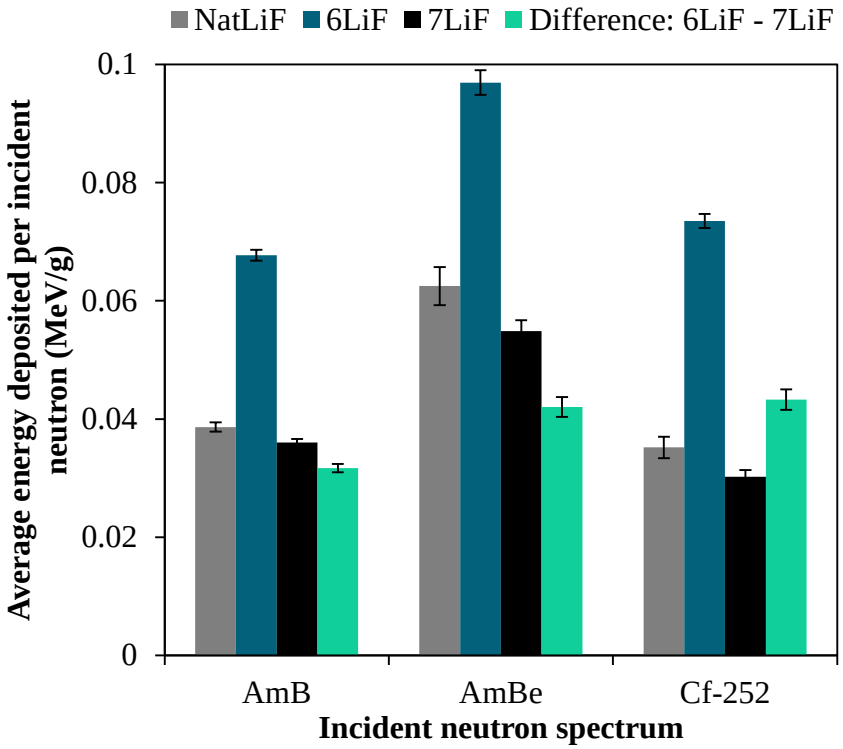

Figure 13: The average energy deposited per incident neutron calculated for the neutron energy spectra shown in Figure 12 calculated using MCNP6.

The response of LiF TLDs exposed to mixed γ-n fields also includes a component due to the photon dose. The total response of the TLD is the sum of the neutron and photon components of response (see equation 9). If the energy spectrum of the neutrons is known, the ratio of the energies deposited from neutron interactions in each material can be calculated. The ratio of the energies deposited by neutrons in each material is assumed to be directly proportional to the ratio of the TL responses of each material (see equation 3). The neutron component of the response of TLD600H can be calculated as shown in equation 10. *k(E)* is defined in equation 11 and functions as an energy dependence correction factor for TLDs irradiated by neutrons with energies above ~ 2 keV.

$$R_{^6LiF} = R_\gamma + R_{^6LiF,n}$$
$$R_{^7LiF} = R_\gamma + R_{^7LiF,n} \qquad [9]$$

$$R_{^6LiF,n} = \frac{R_{^6LiF} - R_{^7LiF}}{1 - \frac{K_{^7LiF,n}}{K_{^6LiF,n}}} \qquad [10]$$

$$\text{let } k(E) = \frac{1}{1 - \frac{K_{^7LiF,n}}{K_{^6LiF,n}}} \qquad [11]$$

$$R_{^6LiF,n} = k\left(R_{^6LiF} - R_{^7LiF}\right) \qquad [12]$$

The *k* factors for three reference spectra (^{241}AmB, ^{241}AmBe and ^{252}Cf) have been calculated using the MCNP6 results shown in Figure 13 and are shown in Figure 14 and Table 8. The mean energy of each spectrum has been calculated according to Khan and Gibbons (2014) and is also shown in Table 8. The energy spectrum of ^{241}AmBe has the highest mean energy (4.05 MeV) and gives the highest *k* factor (see Table 8). This is consistent with the incident energy vs. energy deposited relationship shown in Figure 8, where the lower energy neutrons show a constant ratio of energy deposited in ^{6}LiF to energy deposited in ^{7}LiF but which varies strongly as incident energy increases.

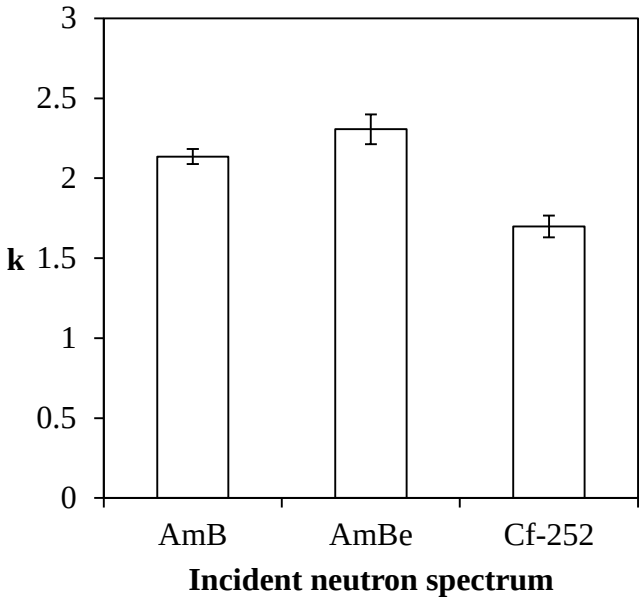

Figure 14: The energy correction factor *k* which is multiplied by the difference between the responses of ^{6}LiF and ^{7}LiF to attain the component of the TL response of ^{6}LiF attributable to neutrons. (See equations 10, 11 and 12).

Table 8: MCNP calculated energy deposition in ^{nat}LiF, of ^{6}LiF and ^{7}LiF as well as the energy correction factor *k* for ^{241}AmB, ^{241}AmBe and ^{252}Cf neutron sources.

Neutron spectrum	**Mean energy (MeV)**	**Energy deposited per incident neutron (MeV/g)**			$k\left(=\frac{1}{1-\frac{K_{^{7}LiF}}{K_{^{6}LiF}}}\right)$
		^{nat}LiF	**^{6}LiF**	**^{7}LiF**	
^{241}AmB	2.63	3.86×10^{-2}	6.77×10^{-2}	3.60×10^{-2}	2.14 ± 0.05
^{241}AmBe	4.05	6.25×10^{-2}	9.69×10^{-2}	5.49×10^{-2}	2.31 ± 0.09
^{252}Cf	1.98	3.52×10^{-2}	7.35×10^{-2}	3.02×10^{-2}	1.70 ± 0.07

If the TLDs can be calibrated under the same neutron energy spectrum as that which they will be exposed to as dosimeters, then the calibration factor can be applied without correction for energy dependence. However, if the TLDs are to be used for dosimetry of neutrons of a different energy spectrum, particularly neutrons moderated or scattered to lower energies, the error will propagate directly into the final estimate of dose. The resulting discrepancy for neutrons produced by medical linear accelerators will be discussed in the next section. Table 9 is included to highlight the magnitude of the error that arises from not correcting for the neutron energy dependence of TLD600H and TLD700H when calibrating with AmB, AmBe or ^{252}Cf sources. Many studies reporting on the neutron contamination present in high energy radiotherapy beams report calibration by isotopic neutron sources. If no energy correction is applied, the calibration factor determined in this way *overestimates* the component of the TLD response caused by neutrons by between 70 and 131 %. The percentage difference is calculated as the corrected value minus the uncorrected value as a fraction of the uncorrected value.

Table 9: The % difference ((corrected – uncorrected)/uncorrected) between calibration factors determined with and without appropriate energy correction factors. The uncorrected value will overestimate the neutron fluence.

Neutron spectrum	**Mean energy (MeV)**	**% difference**
^{241}AmB	2.63	114 %
^{241}AmBe	4.05	131 %
^{252}Cf	1.98	70 %

A set a ^{6}LiF and ^{7}LiF TLDs doped with magnesium, copper and phosphorus (TLD600H and TLD700H from Harshaw (KS, USA)) were exposed to a calibrated ^{241}AmBe neutron source. The source has a nominal activity of 370 GBq with a National Physics Laboratory (UK) calibration certificate stating emissions of 2.062×10^7 n/s (± 5 %) as of 28th September 1995. Fifty TLD600H and 48 TLD700H were exposed for 94.3 hours at a distance of 615 mm from 3rd – 7th of September 2015. The neutron fluence was corrected for decay, attenuation through air, solid angle and anisotropy. The neutron fluence at the location of the TLDs was 440 ± 25 n/s/cm^2. The TLDs were read out using a Harshaw automatic reader and corrected for individual chip variations relative to the average of the TLD batch as determined in a 6 MV photon beam. The results are shown in Figure 15.

The mean TLD600H response was 930 nC with a standard uncertainty of 2 nC and the mean TLD700H response was 840 nC with a standard uncertainty of 3 nC. Using the MCNP6 calculated *k* value for ^{241}AmBe of 2.31 ± 0.09, the neutron component of the response of TLD600H was 210 ± 8 nC. This results in a calibration factor of 7.1×10^5 ($\pm 5 \times 10^4$) neutrons/cm^2 for every nC of response measured for this set of TLD600H. The total uncertainty in the calibration factor is determined by quadratic addition of the uncertainties in the calibration of the activity of the source and the standard uncertainties of the mean of the readings of the TLD600H and TLD700H (JCGM 1995). The uncertainty is quite high because of the relatively small difference between the responses of TLD600H and TLD700H and the 5 % uncertainty in the calibration of the AmBe source.

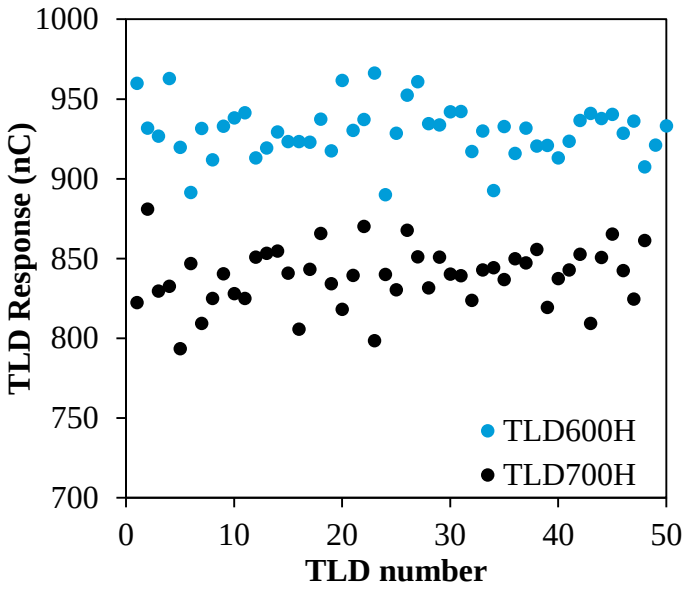

Figure 15: The measured responses of fifty ^{6}LiF TlD600H and forty-eight ^{7}LiF TLD700H following exposure to a standard ^{241}AmBe neutron source. These values are corrected for individual chip variations relative to the average of the TLD batch as determined in a 6 MV photon beam.

4.1.4 Measurement of neutron fluence produced by medical linear accelerators

The energy spectrum of neutrons produced by a medical linear accelerator differs from the spectra produced by isotopic and fission neutron sources. The neutron spectrum of a linac varies with a number of factors including; beam energy, distance from field, distance from scattering materials and type of scattering materials. To investigate the effect of variation in neutron energy spectra on the TLD response, a sample of spectra chosen from published literature will be used.

A number of authors have published calculated and measured linac neutron spectra under specific conditions. Esposito *et al* (2008) measured the neutron spectrum produced by an Elekta Precise operating at 18 MV. Gold foils and LiF TLD pairs were placed inside polyethylene Bonner spheres and the spectrum was acquired from the FRUIT unfolding code. The detectors were placed at four positions within the linac bunker; point 1, at isocentre, point 2, one metre to the right of isocentre, point 3, 1.5 metres from isocentre (away from the gantry) and point 4 at the beginning of the maze. The reported spectra at points 1 – 3 are shown in Figure 16. Kry *et al* (2009a) used MCNPX to calculate the neutron spectrum produced by a Varian 2100 Clinac operating at 18 MV. The neutron energy spectrum was modelled at the patient plane in air without any phantom present, as well as at several depths within tissue. Figure 16 shows the in air spectrum and the spectrum at 1 mm depth in tissue. These spectra will be used as test cases to calculate the TLD response to neutrons of spectra representative of those which may be produced by medical linear accelerators. Their mean energies are given in Table 10.

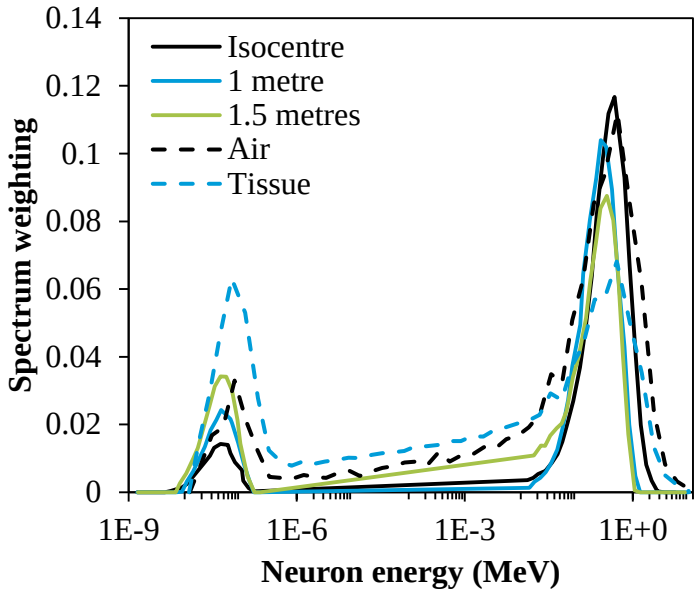

Figure 16: Linac produced neutron energy spectra. The spectra at isocentre, 1 metre and 1.5 metres were measured by Esposito *et al* (2008). The spectra in air and at 1 mm depth in tissue were calculated by Kry *et al* (2009a). The spectra are normalised such that the area under each is equal to one.

The energy deposited in ^{Nat}LiF, ^{6}LiF and ^{7}LiF have been calculated using MCNP6 for the incident energy spectra shown in Figure 16. The geometry described in section 4.1.1 was used in the model, i.e. 3 × 3 × 1 mm^3 TLD chips composed of ^{Nat}LiF, ^{6}LiF and ^{7}LiF with a spherical source (Ø = 1 cm) of isotropic neutrons 10 cm from the TLDs. The neutron source emitted neutrons with the energy spectra shown in Figure 16. Since these spectra are normalised to have a total area of one, the value in each energy bin is effectively a probability of emission within that energy bin. The total energy deposition averaged over a cell and the neutron fluence averaged over the cell were scored and these results were used to calculate the dose deposited per incident neutron. The MCNP6 results are obtained from standard tally 4, which scores the average flux over a cell in particles/cm^2 and standard tally 6+ which scores the total heating over a cell in (MeV/g). The kerma per incident neutron is the tally 6+ result divided by the tally 4 result. The value of *k* was calculated from these results using equation 11.

The energy deposited in each material varies significantly with differing neutron energies (see Figure 17, note the logarithmic scale on the vertical axis). However the energy correction factor, *k*, needed to acquire the neutron component of TLD response is equal to 1.00 for all variations of the linac neutron spectra tested (see Figure 18 and Table 10). This allows the assumption of ^{7}LiF insensitivity to be applied to measurements of linac produced neutrons. The neutron component of the TLD response can be calculated by a simple subtraction of the ^{7}LiF response from the ^{6}LiF response as per equation 2.

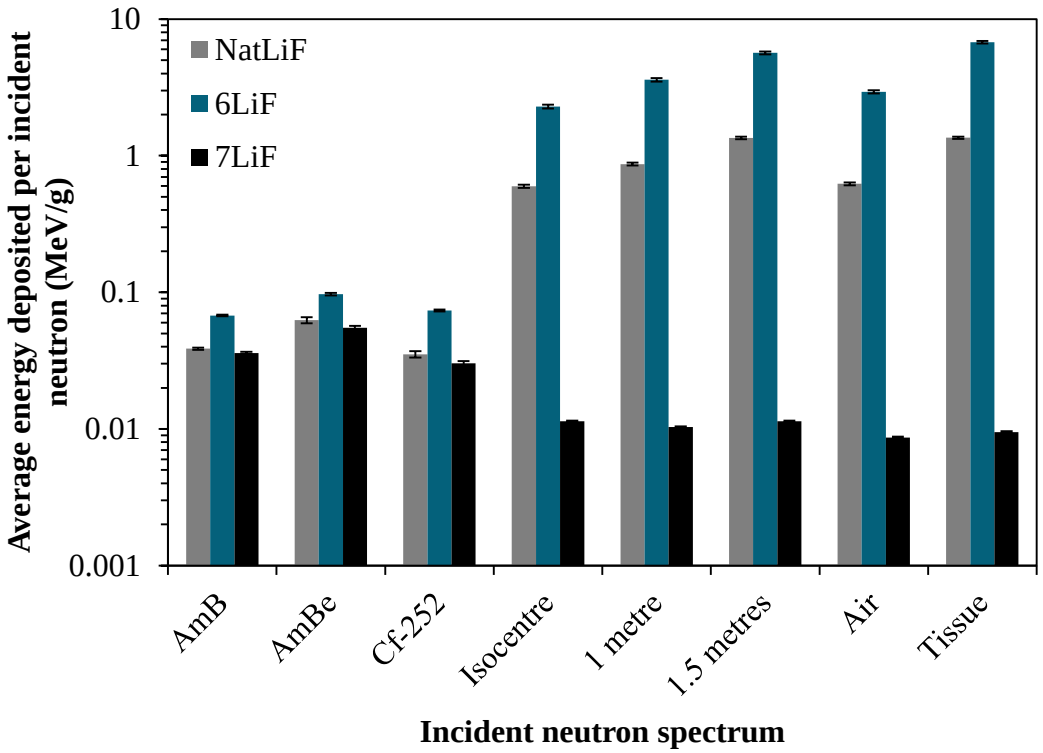

Figure 17: The average energy deposited per incident neutron in ^{Nat}LiF, ^{6}LiF and ^{7}LiF for a variety of incident neutron spectra. The isotopic and fission neutron source results from Figure 13 are shown again for comparison with the spectra from published literature shown in Figure 16. Note the vertical axis is logarithmic.

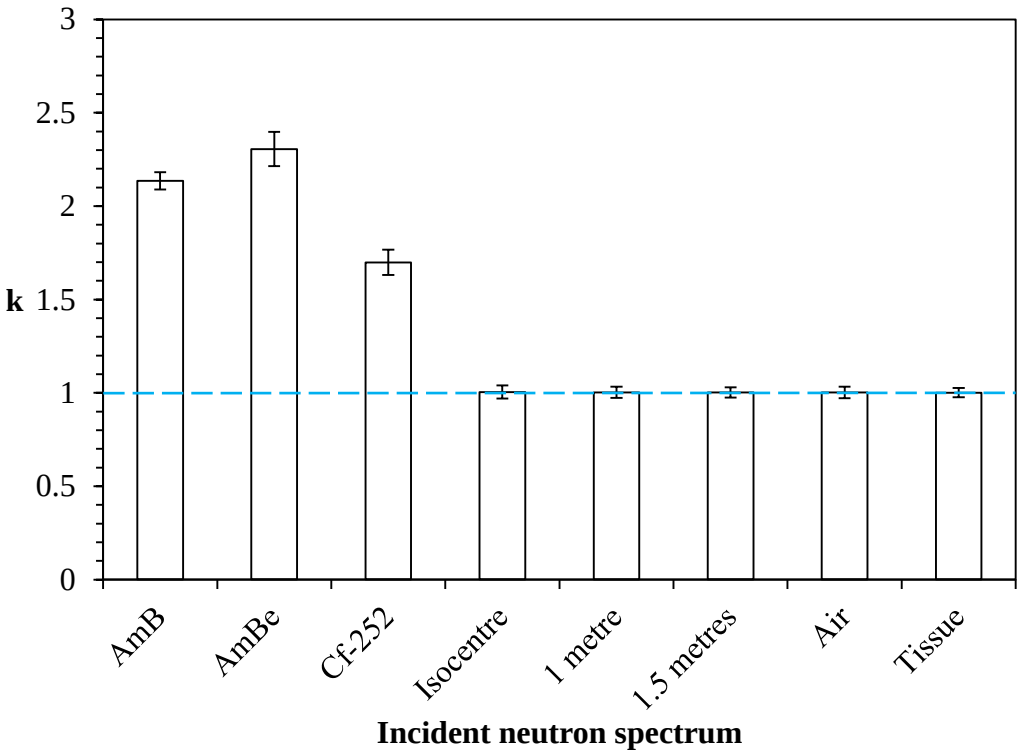

Figure 18: The *k* energy correction factor, defined in equation 11, to account for the variation in energy dependence in ^{6}LiF and ^{7}LiF for various neutron spectra including five sample spectra produced by medical linear accelerators.

Table 10: MCNP calculated energy deposition in ^{nat}LiF, of ^{6}LiF and ^{7}LiF as well as the energy correction factor *k*.

Neutron spectrum	**Mean energy (MeV)**	**Energy deposited per incident neutron (MeV/g)**			**k** $\left(= \frac{1}{1 - \frac{K_{^7LiF}}{K_{^6LiF}}} \right)$
		^{nat}LiF	**^{6}LiF**	**^{7}LiF**	
^{241}AmB [(1)]	2.63	3.86×10^{-2}	6.77×10^{-2}	3.60×10^{-2}	2.14 ± 0.05
^{241}AmBe [(1)]	4.05	6.25×10^{-2}	9.69×10^{-2}	5.49×10^{-2}	2.31 ± 0.09
^{252}Cf [(1)]	1.98	3.52×10^{-2}	7.35×10^{-2}	3.02×10^{-2}	1.70 ± 0.07
Isocentre [(2)]	0.510	0.598	2.29	1.14×10^{-2}	1.00 ± 0.04
1 metre [(2)]	0.310	0.869	3.59	1.03×10^{-2}	1.00 ± 0.03
1.5 metres [(2)]	0.267	1.35	5.66	1.14×10^{-2}	1.00 ± 0.03
Air [(3)]	0.249	0.623	2.94	8.65×10^{-3}	1.00 ± 0.03
Tissue [(3)]	0.146	1.35	6.77	9.47×10^{-3}	1.00 ± 0.03

[(1)] (ISO8529-1 2001) [(2)] (Esposito *et al* 2008) [(3)] (Kry *et al* 2009a)

4.1.5 Determining neutron dose to tissue using TLDs

The neutron energy spectrum produced by medical linear accelerators is of sufficiently low energy that the ratio between the responses of ^{6}LiF and ^{7}LiF is constant. This allows the accurate measurement of neutron fluence without needing detailed information about the energy spectrum. To determine the dose to tissue, the neutron interactions in tissue need consideration. Tissue is primarily composed of ^{1}H (63% w/w), ^{16}O (24% w/w) and ^{12}C (12% w/w) (Valentin 2002). Neutron interactions with these nuclei have very different cross section and energy deposition functions as compared to TLDs. For neutrons below ~ 10 keV, the primary interactions which deposit dose to tissue are ^{1}H(n,γ) which produces a 2.2 MeV gamma-ray and ^{14}N(n,p) which releases 0.58 MeV (ICRP116 2010).

Tissue also differs in that the energy spectrum is rapidly moderated as the neutrons penetrate the material. In this study MCNP6 has been used to calculate the fluence and energy deposited in 1 cm depth increments in ICRP soft tissue (Valentin 2002). A 30 × 30 × 1 cm^3 neutron source was modelled 10 cm from one surface of a 30 × 30 × 30 cm^3 tissue phantom. The neutrons were initiated in the source cell with direction vectors toward the cube of tissue. The scoring cells were 1 × 1 × 1 cm^3 cubes at the centre of the phantom at 1 cm increments from the surface facing the source. This was to ensure adequate scattering material surrounding the scoring voxels. The fluence and energy deposition resulting from monoenergetic neutron sources of different energies are shown in Figure 19, Figure 20 and Figure 21. The fluence and energy deposited in tissue resulting from the test case spectra given in Figure 12 and Figure 16 are shown in Figure 22 and Figure 23 respectively.

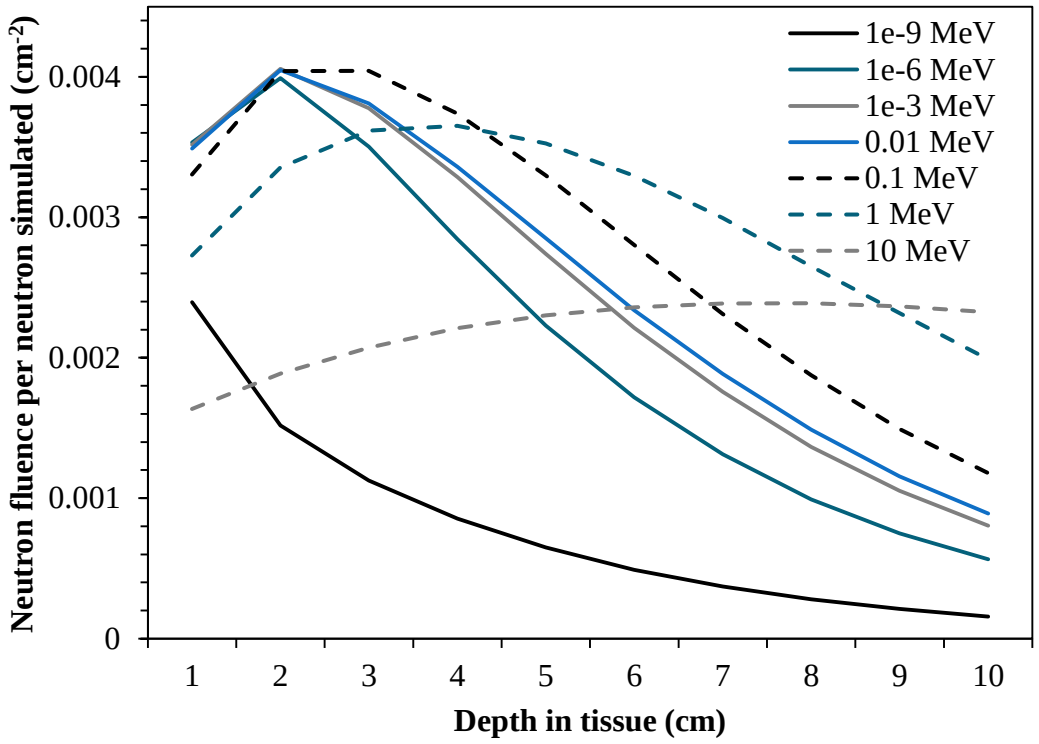

Figure 19: Neutron fluence as a function of depth in tissue in 1 cm increments calculated with MCNP6. Each curve is a different sample neutron source of a given energy.

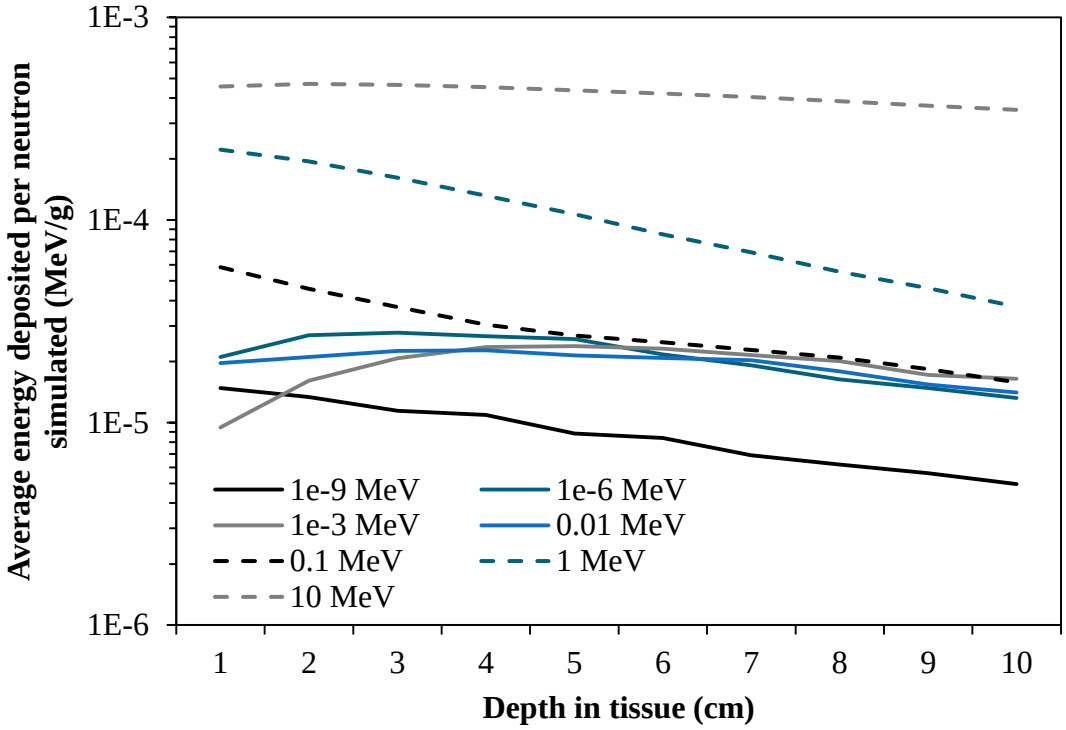

Figure 20: Average energy deposited as a function of depth in tissue in 1 cm increments calculated with MCNP6. Each curve is a different sample neutron source of a given energy.

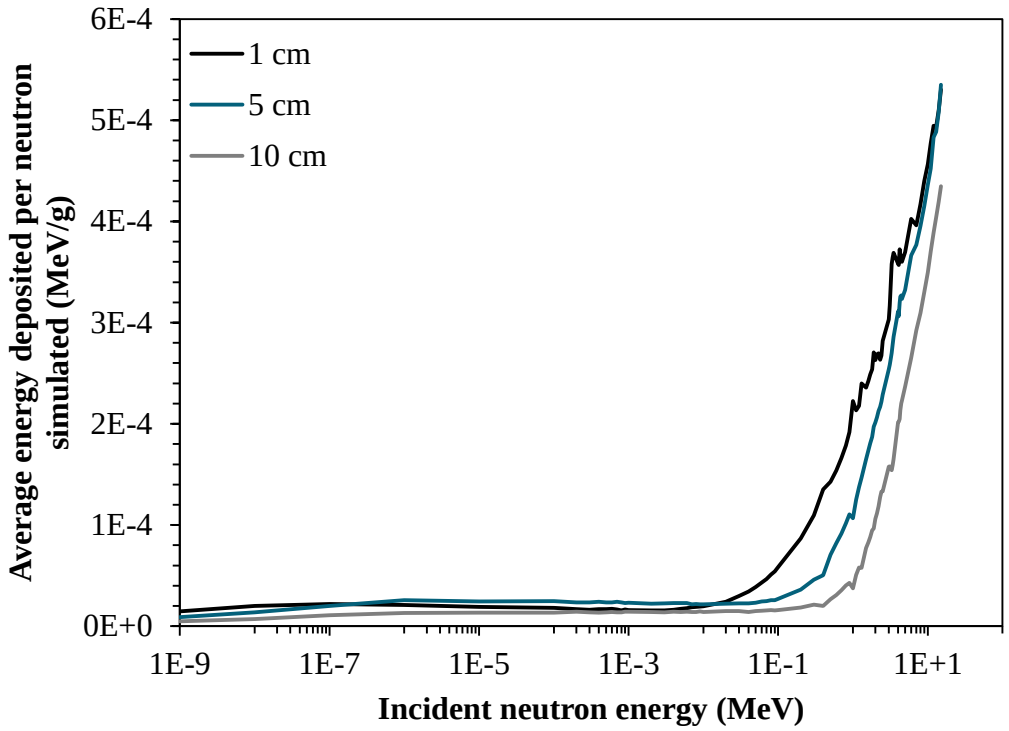

Figure 21: The average energy deposited by incident neutrons as a function of energy at three depths in tissue.

The fluence and energy deposited by a selection of the modelled monoenergetic neutron sources are shown in Figure 19 and Figure 20 respectively. The depth in tissue at which the maximum fluence occurs differs with the incident energy of the neutrons. Higher energy neutrons penetrate tissue more easily and have deeper fluence maxima. The lowest energy modelled, 1×10^{-9} MeV (1 meV), shows no build up behaviour since these neutrons are almost completely thermalised and the cross section for absorption rapidly increases at these low energies. The higher energy neutrons are more likely to undergo scattering interactions. Multiple scattering events within the phantom and (n,2n) interactions cause the fluence to maximise at a given depth in tissue.

The energy deposited as a function of depth in tissue for a selection of monoenergetic neutron sources is shown in Figure 20. Here the behaviour is quite different, with the build-up on entry to the denser medium completely absent. The dose gradient is almost flat as a function of depth. The main mechanism of dose deposition in tissue comes from capture-type interactions which emit secondary radiations. Scattering interactions also result in some energy deposition, but the dominating effect is neutrons which are captured following moderation.

The energy deposited as a function of incident neutron energy for a selection of depths in tissue is shown in Figure 21. These show a rapid increase in the energy released for incident neutrons with energies above a threshold energy of around 10 keV. The threshold varies with depth in tissue, increasing as the depth increases due to moderation. Incident neutrons are further reduced in energy the deeper they penetrate. Neutrons with energy below 10 keV release similar amounts of energy, around 0.19 eV per neutron locally. Above 10 keV interactions which release larger amounts of energy to tissue begin to dominate.

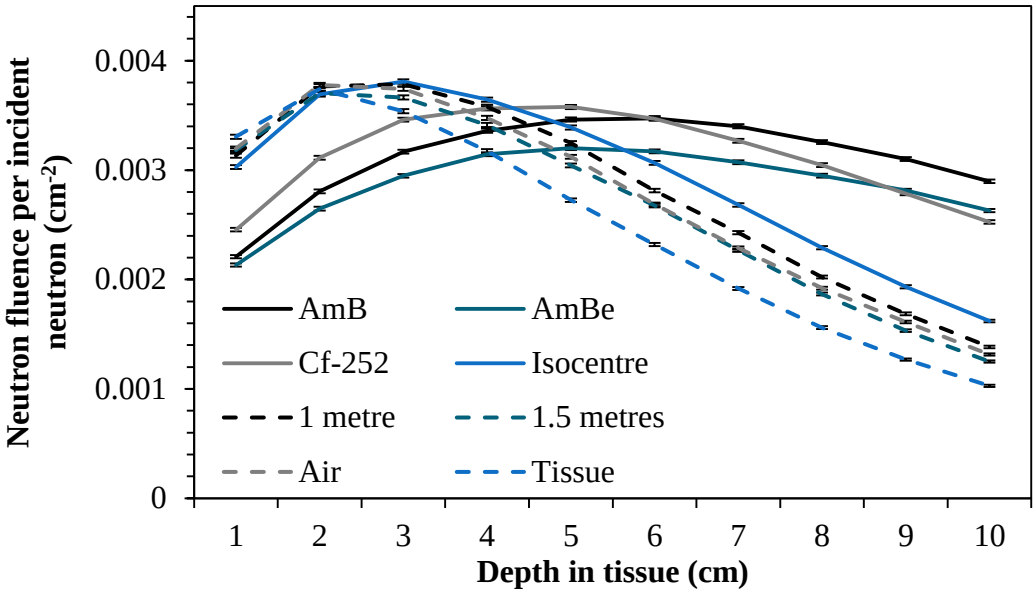

Figure 22: Neutron fluence as a function of depth in tissue for various incident neutron spectra. The isocentre, 1 metre and 1.5 metre spectra are taken from Esposito *et al* (2008) and the air and tissue spectra are taken from Kry *et al* (2009a).

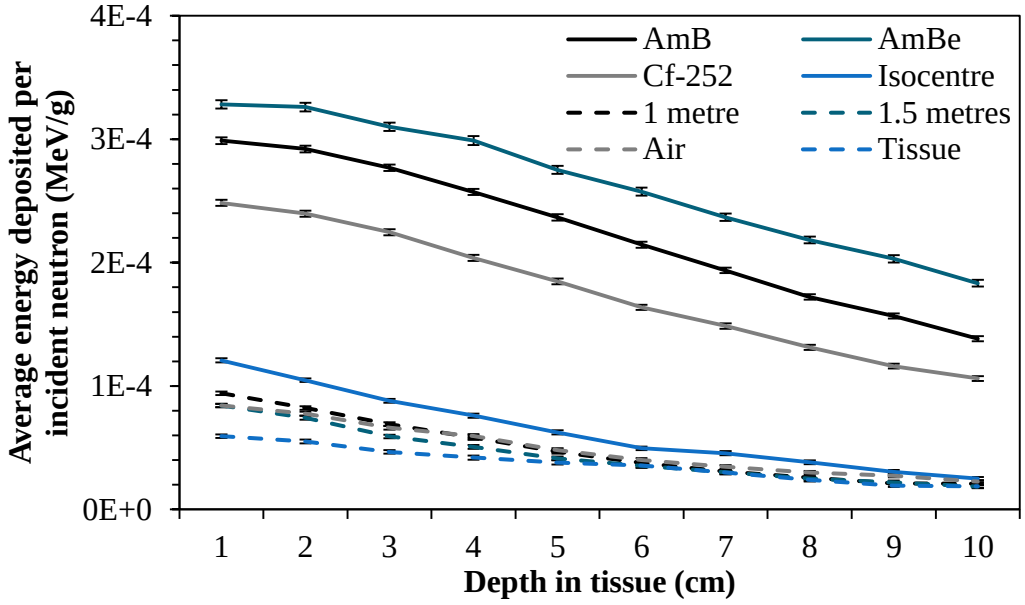

Figure 23: Energy released by neutrons as a function of depth in tissue for various incident neutron spectra. The isocentre, 1 metre and 1.5 metre spectra are taken from Esposito *et al* (2008) and the air and tissue spectra are taken from Kry *et al* (2009a).

The fluence and energy calculated as a function of depth in tissue for various energy spectra are shown in Figure 22 and Figure 23 respectively. The fluence function shows similar behaviour to the monoenergetic fluence functions of Figure 19, with the spectra of higher mean energies penetrating more deeply in tissue. The lower energy spectra reach a maximum at around 2 cm depth and fall off with a steeper gradient (see Figure 22). The energy deposited at different depths shows a simple drop off, with the maximum energy released within the first centimetre of tissue and a steady drop off with depth.

The energy deposited in tissue varies with the incident neutron energy spectrum, with greater energy released by incident neutrons of higher energies. The depth-energy deposition curves calculated for the various linac produced neutron energy spectra show differences in the magnitude of energy released. So, although the energy deposited (Figure 17) in the TLD materials (and therefore their responses) does not vary significantly with these differences in neutron energy, the dose to tissue *does* vary with small differences in neutron energy. Whilst the neutron *fluence* can be easily measured using ^{6}LiF and ^{7}LiF TLD pairs, the dose to tissue cannot be determined unless the neutron energy spectrum is well known for the specific measurement conditions. ^{6}LiF and ^{7}LiF "thermoluminescence dosimeters" should therefore be used as *detectors* rather than *dosimeters* in this context. Only if the neutron energy spectrum is known can the fluence be converted to dose.

4.2 Activation foils

Neutrons incident on a material may cause it to become radioactive. If the material has a high neutron interaction cross section, particularly for neutron capture, a measurable amount of radioactivity can be produced. If the mass and composition of the material are well known, the degree of induced radioactivity can be used to calculate the neutron fluence. Indium and copper foils have been used here; chosen for their high cross sections. Neutron interaction cross sections typically have a strong dependence on the neutron energy spectrum. A small error in the assumed neutron energy can result in a large error in the estimation of the corresponding cross section value, which in turn, propagates to the final flux result. Care must be taken in determining an appropriate cross section value, and the spectral distribution of neutron energies should be considered.

4.2.1 Calculation of neutron fluence

A neutron activation foil sample is placed in the neutron fluence to be measured. Krane (1987) gives the rate of activation, *R*, in a sample as;

$$R = N_0 \sigma \phi \qquad [\ 13\ ]$$

where N_0 is the number of target nuclei of the isotope of interest, σ is the cross section in cm^{-2} and ϕ is the neutron fluence rate in cm^{-2}·s^{-1}.

For an elemental sample, the number of target nuclei, N_0, can be calculated from stoichiometry as follows;

$$N_0 = \frac{m \eta \alpha}{w} \qquad [\ 14\ ]$$

where *m* is the mass of the sample in grams, η is Avogadro's number, α is the fraction of target nuclei in the sample (often the natural abundance of the isotope) and *w* is the molar mass of the isotope in grams·mol^{-1}.

These combine such that the rate of activation can then be written;

$$R = \frac{m\eta\alpha\sigma\phi}{w} \qquad [15]$$

It is generally accepted that the number of radioactive nuclei produced, N_1, can be described by the following differential equation;

$$dN_1 = Rdt - \lambda N_1 dt \qquad [16]$$

where λ is the decay constant for the isotope produced. A solution for this differential equation follows;

$$N_1 = \frac{R}{\lambda} \cdot \left(1 - e^{-\lambda t_i}\right) \qquad [17]$$

where t_i is the time since the sample was placed in the neutron flux (Krane 1987).

This can be extended for when the sample is removed from the neutron flux and the radioisotope ceases to be produced. The number of nuclei begins to decrease exponentially as follows;

$$N_1 = \frac{R}{\lambda} \cdot \left(1 - e^{-\lambda t_i}\right) \cdot e^{-\lambda t_c} \qquad [18]$$

where t_c is the cooling time (time since the sample was removed from the neutron flux).

The activity of the sample is then measured via gamma spectroscopy. The net area of a photopeak, A_{net}, is related to the true number of disintegrations N_d as follows;

$$N_d = \frac{A_{net} t_r}{t_l \varepsilon f} \qquad [19]$$

where t_r and t_l are the real and live count times of the detector respectively, ε is an efficiency factor accounting for the intrinsic efficiency of the detector for the energy of the gamma emission and the geometric efficiency of the sample and detector arrangement. f is the fraction of emissions for a given gamma energy per decay of the radioisotope.

The number of disintegrations during the measurement time (t_r) can also be calculated from the earlier expression for N_1 (equation 18);

$$N_d = \frac{R}{\lambda} \cdot \left(1 - e^{-\lambda t_i}\right) \cdot e^{-\lambda t_c} \cdot \left(1 - e^{-\lambda t_r}\right) \qquad [20]$$

Thus, from the counts in a photopeak, the neutron flux density can be determined;

$$\phi = \frac{A_{net} t_r \lambda w}{t_l \varepsilon f m \eta \alpha \sigma \cdot \left(1 - e^{-\lambda t_i}\right) \cdot e^{-\lambda t_c} \cdot \left(1 - e^{-\lambda t_r}\right)} \qquad [21]$$

Where the quadratic addition of uncertainties (JCGM 1995) gives;

$$\Delta\phi = \sqrt{\begin{aligned}&\left(\frac{\partial\phi}{\partial A_{net}}\Delta A_{net}\right)^2 + \left(\frac{\partial\phi}{\partial t_r}\Delta t_r\right)^2 + \left(\frac{\partial\phi}{\partial\lambda}\Delta\lambda\right)^2 + \left(\frac{\partial\phi}{\partial w}\Delta w\right)^2 + \left(\frac{\partial\phi}{\partial t_l}\Delta t_l\right)^2 + \ldots \\ &\ldots + \left(\frac{\partial\phi}{\partial\varepsilon}\Delta\varepsilon\right)^2 + \left(\frac{\partial\phi}{\partial f}\Delta f\right)^2 + \left(\frac{\partial\phi}{\partial m}\Delta m\right)^2 + \left(\frac{\partial\phi}{\partial\eta}\Delta\eta\right)^2 + \left(\frac{\partial\phi}{\partial\alpha}\Delta\alpha\right)^2 + \ldots \\ &\ldots + \left(\frac{\partial\phi}{\partial\sigma}\Delta\sigma\right)^2 + \left(\frac{\partial\phi}{\partial t_i}\Delta t_i\right)^2 + \left(\frac{\partial\phi}{\partial t_c}\Delta t_c\right)^2\end{aligned}} \qquad [22]$$

$$\Delta\phi = \sqrt{\begin{aligned}&\left(\frac{\phi}{A_{net}}\Delta A_{net}\right)^2 + \left(\frac{\phi\cdot\left(1-e^{-\lambda\cdot t_r}-t_r\cdot\lambda\cdot e^{-\lambda\cdot t_r}\right)}{t_r\cdot(1-e^{-\lambda\cdot t_r})}\Delta t_r\right)^2 + \left(\frac{\partial\phi}{\partial\lambda}\Delta\lambda\right)^2 + \left(\frac{\phi}{w}\Delta w\right)^2 + \ldots \\ &\ldots + \left(\frac{-\phi}{t_l}\Delta t_l\right)^2 + \left(\frac{-\phi}{\varepsilon}\Delta\varepsilon\right)^2 + \left(\frac{-\phi}{f}\Delta f\right)^2 + \left(\frac{-\phi}{m}\Delta m\right)^2 + \left(\frac{-\phi}{\eta}\Delta\eta\right)^2 + \ldots \\ &\ldots + \left(\frac{-\phi}{\alpha}\Delta\alpha\right)^2 + \left(\frac{-\phi}{\sigma}\Delta\sigma\right)^2 + \left(\frac{\phi\cdot\lambda\cdot e^{-\lambda\cdot t_i}}{(1-e^{-\lambda\cdot t_i})}\Delta t_i\right)^2 + \left(\phi\cdot t_c\Delta t_c\right)^2\end{aligned}} \qquad [23]$$

Where, [24]

$$\frac{\partial\phi}{\partial\lambda} = \frac{\phi\cdot\left[e^{-\lambda\cdot(t_i+t_r)}\cdot(\lambda\cdot t_i+\lambda\cdot t_r+\lambda\cdot t_c+1)-e^{-\lambda\cdot t_i}\cdot(\lambda\cdot t_i+\lambda\cdot t_c+1)-e^{-\lambda\cdot t_r}\cdot(\lambda\cdot t_r+\lambda\cdot t_c+1)+\lambda\cdot t_c+1\right]}{\lambda\cdot\left(1-e^{-\lambda\cdot t_i}\right)\cdot\left(1-e^{-\lambda\cdot t_r}\right)}$$

4.2.2 Calculation of net photopeak counts

The counts in a photopeak should be corrected for “background”. A background spectrum should be acquired for an appropriate length of time and subtracted from the activation spectrum. Aside from this, a background of Compton scatter exists for lower photopeak energies, as shown in Figure 24, the channels either side of the peak do not have zero counts.

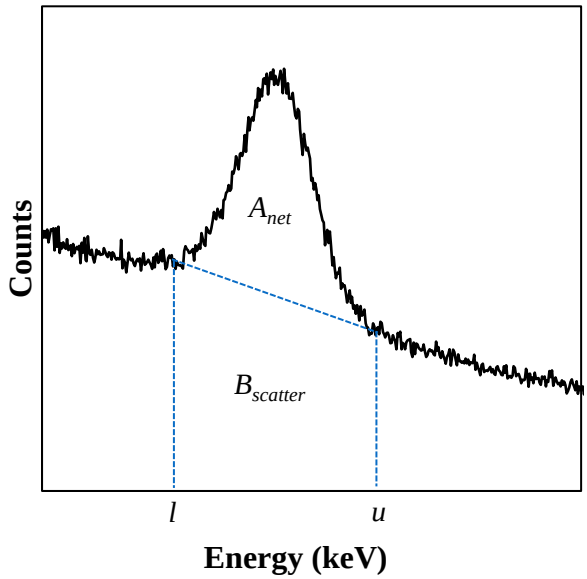

Figure 24: A sample gamma spectroscopy peak. l and u are the lower and upper channels of the peak width, $B_{scatter}$ is the Compton scatter background and A_{net} is the net peak area.

A Region Of Interest (ROI) is set around the photopeak for which the area is to be calculated. The lower energy edge of the ROI is designated l and the upper edge u. The net area of the photopeak can be calculated as follows (Ortec 2006):

$$A_{net} = A_{gross} - B_{scatter} \qquad [25]$$

where;

$$A_{gross} = \sum_{i=l+3}^{u-3} C_i \qquad [26]$$

and;

$$B_{scatter} = \left(\sum_{i=l}^{l+2} C_i + \sum_{i=u-2}^{u} C_i \right) \frac{u-l+1}{6} \qquad [27]$$

where i is the channel number.

In this method, the first three channels on each side within the ROI selected are used to calculate the baseline level outside of the photopeak, which is then subtracted from the data in the remaining channels inside the ROI. If the ROI limits are set too narrowly and there is a steep gradient between the three points taken inside each side of the ROI the number of counts in the baseline will include some genuine photopeak counts and will result in calculation of a net area lower than what was detected. The ROI

should be carefully set so that the first three points inside the ROI on each side have a relatively flat gradient. This may result in the ROI being slightly wider than the photopeak, but this is corrected for as the net area is calculated from the fourth channel inside the ROI.

The uncertainty in the net photopeak area can be calculated from the following (Ortec 2006);

$$\Delta A_{net} = \sqrt{A_{gross} + B_{scatter} \cdot \left(\frac{u-l-5}{6}\right) \cdot \left(\frac{u-l-5}{u-l+1}\right)} \qquad [\ 28\ ]$$

4.2.3 Calculating the gamma detection efficiency

The detection efficiency of the detector is essential to the accurate calculation of the neutron fluence. Two sodium iodide (NaI(Tl)) scintillators were used to measure the activity of activation foils. To convert the number of counts measured to the activity of the material, the total detector efficiency is required. The total efficiency is a combination of the intrinsic efficiency of the detector and the geometric efficiency of the physical source-detector arrangement. The intrinsic efficiency of the detector depends on the energy of the gamma-rays to be measured.

A ^{137}Cs point source with a calibrated activity of 10.37 μCi (± 3.7 %) was used to measure the total efficiency of the two NaI(Tl) detectors for 662 keV gamma-rays. The reference date of the activity calibration is 1st June 1976, and the efficiency measurements were carried out on 16th March 2015. The half-life of ^{137}Cs is 30.08 years and for the elapsed time of 38.79 years, the activity of the source on the day of measurement was 4.242 μCi or 1.570×10^5 Bq. Recordings of 1002 and 1153 counts per second (± 3 %) were recorded on detectors A and B respectively. The total efficiency, ε, is defined as the measured count rate divided by the activity corrected for the emission intensity of the gamma-ray measured. The emission intensity of the 662 keV gamma-ray of ^{137}Cs is 0.8510 (Browne and Tuli 2007), meaning ~85 662 keV gamma-rays will be emitted for every 100 decays of ^{137}Cs nuclei. This results in total efficiencies of 7.50×10^{-3} ± 5 % for detector A and 8.63×10^{-3} ± 5 % for detector B.

Although both detectors are seemingly identical, with identical electronics, shielding and geometries, there are obviously some differences affecting the overall efficiency. Small differences in source-to-detector distance can make a large difference to the solid angle of emissions intersecting the detector and the geometric efficiency difference contributes to an overall difference in total efficiency. An MCNP model of the source, detector and its shielding was used to calculate the total detection efficiency (see Figure 25). The ^{137}Cs point source was modelled as a cylinder with thickness and radius of 0.1 mm. The indium activation foils are rectangular with dimension of 2.5 × 2.5 cm^2 and thickness of 1 mm and are modelled as such. The copper activation foils are cylindrical with radii of 1.25 cm and thicknesses of 0.1 mm are were modelled as such.

Intrinsic differences between the two detectors can be caused by differences in detector size and volume, or differences in applied bias voltage. In the absence of detailed knowledge of the cause of the difference between the two detectors, MCNP calculations were performed for different source to detector distances and an inverse square fit of the results was used to determine the source to detector distance for each detector. Detector A was simulated with a source to detector distance of 11.942 cm and calculated a total efficiency of $(7.49 \pm 0.01) \times 10^{-3}$ and detector B was modelled at a distance of 10.944 cm from the source to achieve a total efficiency of $(8.63 \pm 0.01) \times 10^{-3}$.

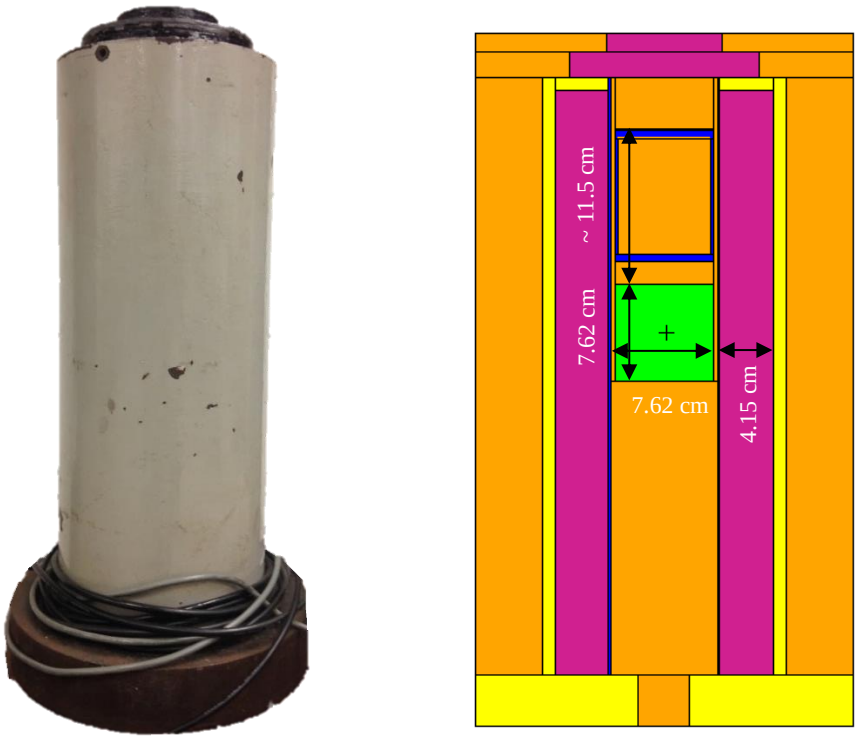

Figure 25: Left: photo of the shielding and support assembly of the NaI detector. Right: MCNP model of the NaI detector (green), lead shielding (pink), stainless steel supports (yellow) and PVC source support (blue). Orange is the air surrounding the detector.

The models with optimised source to detector distances for each detector were then used to calculate the efficiency of detection for the gamma emissions produced by indium and copper following neutron capture. The results are shown in Table 11 and Figure 26 along with the previous stated values calculated for the 662 keV gamma emission of the ^{137}Cs source of known activity which was also used to verify the models of each detector. The measured results are also shown for comparison.

Table 11: The MCNP calculated total detection efficiencies for the ^{137}Cs 662 keV gamma-ray used to measure the efficiency and the gamma-rays emitted by the indium and copper following neutron activation.

Detector	**A**	**B**
Source to detector distance (cm)	11.942	10.944
Gamma-ray energy	**Measured total detection efficiency**	
^{137}Cs: 662 keV	$7.50 \times 10^{-3} \pm 5$ %	$8.63 \times 10^{-3} \pm 5$ %
Gamma-ray energy	**Calculated total detection efficiency**	
^{137}Cs: 662 keV	$(7.49 \pm 0.01) \times 10^{-3}$	$(8.63 \pm 0.01) \times 10^{-3}$
^{116}In: 417 keV	$(1.079 \pm 0.001) \times 10^{-2}$	$(1.245 \pm 0.001) \times 10^{-2}$
^{116}In:818 keV	$(6.31 \pm 0.01) \times 10^{-3}$	$(7.25 \pm 0.01) \times 10^{-3}$
^{116}In:1097 keV	$(4.992 \pm 0.008) \times 10^{-3}$	$(5.723 \pm 0.009) \times 10^{-3}$
^{116}In:1294 keV	$(4.366 \pm 0.009) \times 10^{-3}$	$(5.004 \pm 0.009) \times 10^{-3}$
^{64}Cu: 511 keV	$(9.24 \pm 0.01) \times 10^{-3}$	$(1.064 \pm 0.001) \times 10^{-2}$

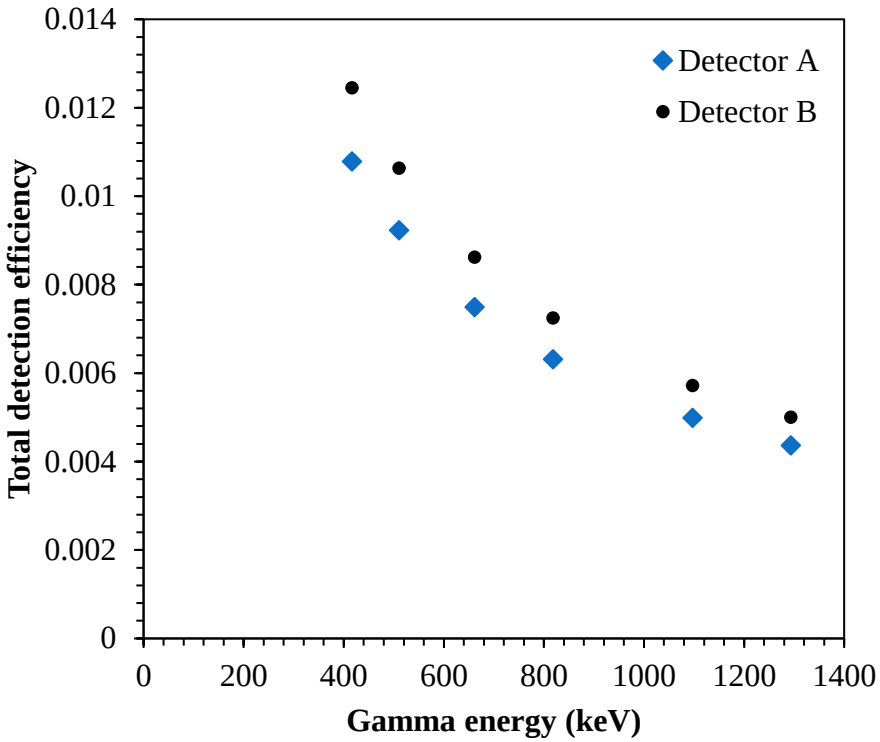

Figure 26: The MCNP calculated total detection efficiencies as a function of gamma-ray energy. The difference between detector A and detector B arises purely from the different source to detector distance modelled.

4.2.4 Calculating the cross section

The neutron capture cross section is strongly dependent on the energy of the incident neutrons. As shown in Figure 27, it may vary over eight orders of magnitude in the relevant energy range. Accurate knowledge of the neutron energy spectrum at the point of measurement is required to calculate the neutron flux. For the use of activation foils with standard neutron sources, the neutron spectra are readily available in published data, such as ISO8529-1 (2001). However, for moderated sources or photoneutrons from linear accelerators, simulations are required to obtain this data.

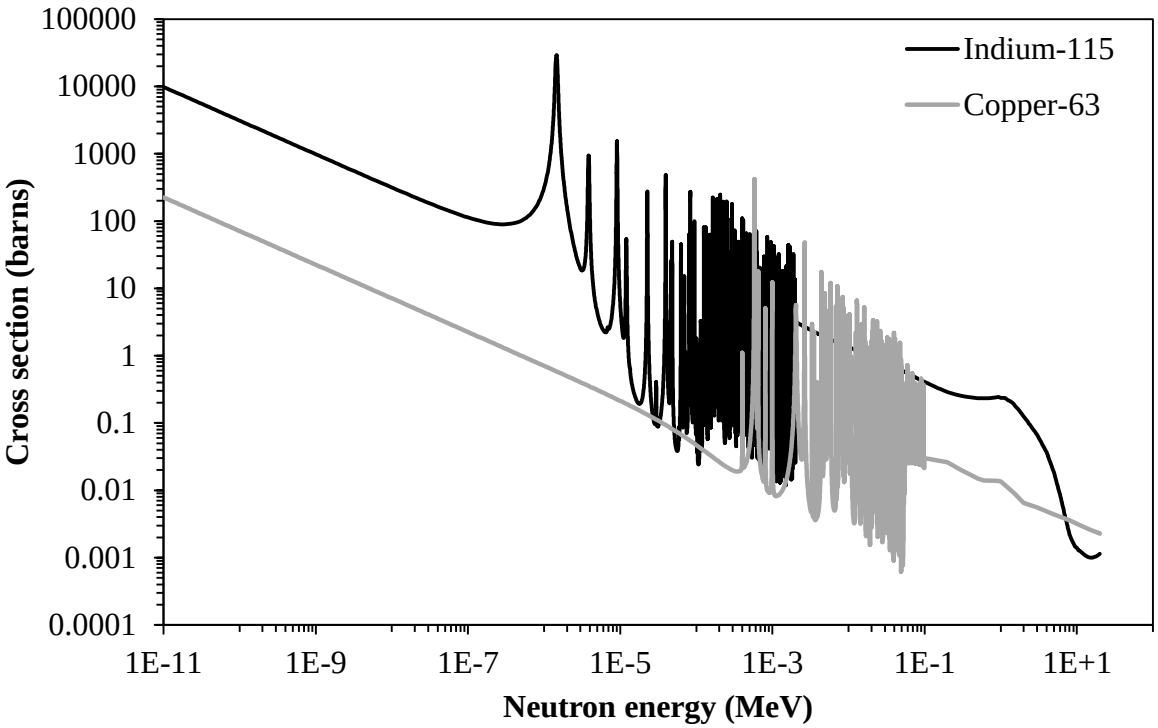

Figure 27: The neutron capture cross sections for indium-115 and copper-63 as a function of incident neutron energy from ENDF/B.VII.1 (Chadwick *et al* 2011)

The total energy weighted reaction probability for a specific neutron flux can be calculated;

$$P_{total} = \int_{E_{\min}}^{E_{\max}} B(E) \cdot \sigma(E) \cdot dE \qquad [\ 29\ ]$$

where B is the emission probability for a given energy bin. The energy resolution of the cross section data and the energy bins of the neutron spectrum data are nearly always different. The cross section data can be resampled to match the energy bins in the spectrum data. For cross section data of finer resolution a weighted average across the bin is taken. An example is provided in Figure 28. The energy weighted probability can then be calculated by multiplying the weighted average cross section value in each bin (blue) by the fraction of neutrons emitted with energy in that bin (grey). The total probability for a neutron fluence of a given spectrum is the sum of the energy weighted reaction probability (green). The calculated cross sections for neutron capture in indium-115 and copper-63 for neutrons of the energy spectra given in Figure 16 are given in Table 12.

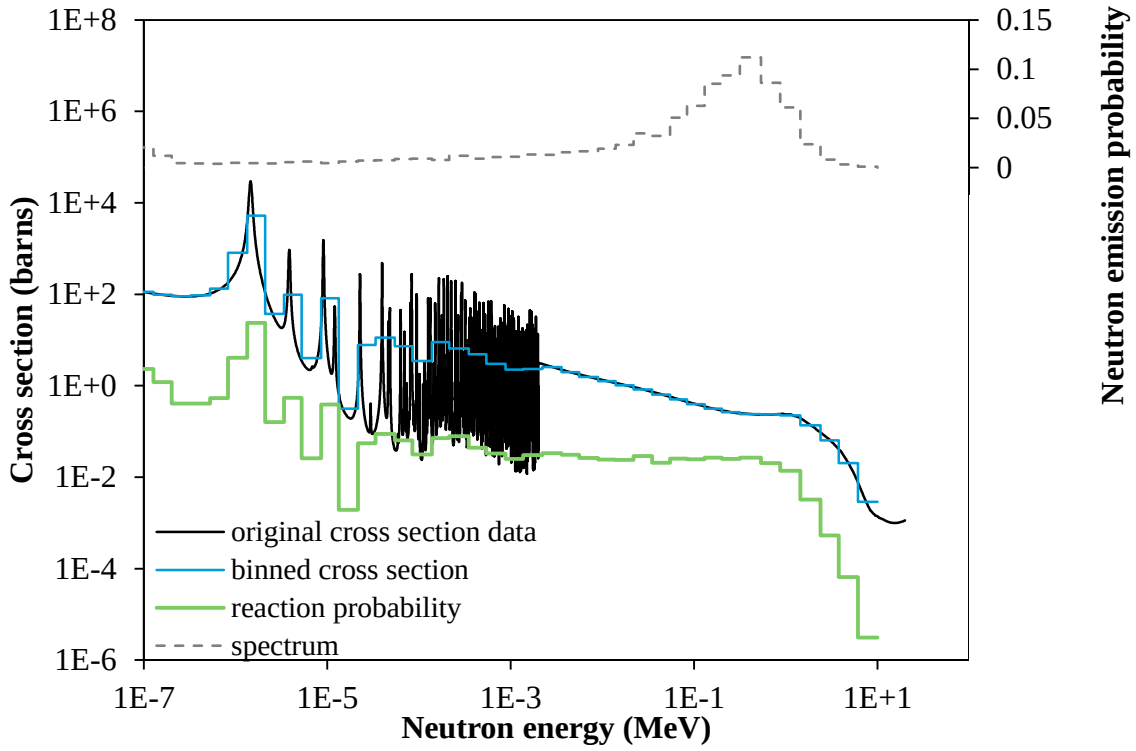

Figure 28: The neutron capture cross section of indium-115 is labelled "original cross section data". The energy spectrum of linac neutrons in air (Kry *et al* 2009a) is shown as "spectrum" and is plotted against the right-hand vertical axis. The spectrum is normalised such that its integral is one, so that the value in each bin is the probability of neutron emission within that energy range. The "binned cross section" shows the original cross section data resampled into bins equal to those in the spectrum data. The "reaction probability" is the resampled, interpolated cross section multiplied by the probability of neutron emission within that energy range.

Table 12: Energy weighted interaction probabilities for neutron capture in indium-115 and copper-63 calculated for various neutron energy spectra. The spectra of standard ^{241}AmB, ^{241}AmBe and ^{252}Cf are taken from ISO8529-1 (2001). The spectra at isocentre, 1 metre and 1.5 metres were measured by Esposito et al (2008). The spectra in air and in tissue were calculated by Kry et al (2009).

Neutron Energy Spectrum	**Indium-115 neutron capture cross section (cm^2)**	**Copper-63 neutron capture cross section (cm^2)**
^{241}AmB	9.137×10^{-26}	6.505×10^{-27}
^{241}AmBe	8.374×10^{-26}	7.792×10^{-27}
^{252}Cf	1.568×10^{-25}	1.045×10^{-26}
Isocentre	1.629×10^{-23}	3.568×10^{-25}
1 metre	2.338×10^{-23}	5.037×10^{-25}
1.5 metres	3.587×10^{-23}	7.705×10^{-25}
Air	4.788×10^{-23}	4.704×10^{-25}
Tissue	9.898×10^{-23}	9.440×10^{-25}

4.2.5 Calculating fluence

Once the area of the detected gamma-ray peak has been calculated and values for neutron interaction cross section and total detection efficiency of the produced gamma-rays have been selected, the neutron fluence can be easily calculated. The irradiation time, cooling time, detector "live" and "real" times are easily measured. The mass of the sample is easily measured and the isotopic ratio can be found in reference data. The emission intensity of each gamma-ray energy emitted by the sample can also be easily found in reference data. Equation 20 from §4.2.1 is repeated below. A summary of the terms required is given in Table 13.

From this information the neutron fluence causing the activation can be calculated.

$$\phi = \frac{A_{net} t_r \lambda w}{t_i \varepsilon f m \eta \alpha \sigma \cdot \left(1 - e^{-\lambda t_i}\right) \cdot e^{-\lambda t_c} \cdot \left(1 - e^{-\lambda t_r}\right)} \qquad [\ 30\ ]$$

Table 13: Summary and description of parameters needed to calculate neutron fluence from activation foils.

Parameter	**Notes**	**Parameter**	**Notes**
ϕ ($cm^{-2} \cdot s^{-1}$)	Neutron fluence rate	f	^{116}In: 416 keV: 0.272 818 keV: 0.1213 1097 keV: 0.585 1294 keV: 0.848 (Blachot 2010) ^{64}Cu: 511 keV: 0.352 (Singh 2007)
A_{net} (s^{-1})	Measured and calculated according to §4.2.2	m (g)	Measured with a laboratory balance
t_r (s)	Measured in detector software (Ortec 2006)	η (mol^{-1})	$6.02214129 \times 10^{23}$ (Krane 1987)
λ (s^{-1})	^{116}In: 2.128×10^{-4} (Blachot 2010) ^{64}Cu: 1.516×10^{-5} (Singh 2007)	α	^{115}In: 0.9571 ^{63}Cu: 0.6917 (Rosman and Taylor 1999)
w ($g \cdot mol^{-1}$)	^{115}In: 114.903878 ^{63}Cu: 62.929601 (Audi and Wapstra 1993)	σ (cm^2)	Calculated according to §4.2.3 *NB:* depends strongly on the neutron energy spectrum
t_l (s)	Measured in detector software (Ortec 2006)	t_i (s)	Measured with a stopwatch
ε	Calculated according to §4.2.4	t_c (s)	Measured with a stopwatch

4.3 Converting neutron fluence to dose using MCNP6

The two methods of neutron detection described in §4.1 and §4.2 offer the measurement of neutron fluence and not of dose. The correct interpretation of the responses of lithium fluoride thermoluminescence dosimeters and of indium and copper activation foils depends strongly on an accurate and detailed knowledge of the energy spectrum of the neutrons to be measured. The response of the detectors can be used to calculate the neutron fluence to which they were exposed. Whilst an accurate measurement of the neutron fluence is useful, it doesn't allow the evaluation of the risk to a patient or staff member exposed to the neutron fluence from a medical linear accelerator. Absorbed dose is often used as a proxy to describe risk because the dose and risk can be linked through observable biological effects.

MCNP6 was used in §4.1.5 to investigate the differences between energy deposited by neutrons in TLD materials and in tissue materials. The results for energy deposited in the first 1 cm of a $30 \times 30 \times 30$ cm^3 ICRP soft tissue phantom per unit neutron fluence in that volume are shown in Figure 29. These values can be used to determine fluence to dose conversion factors for neutron exposures to soft tissue if the energy spectrum of the neutrons is known.

MCNP6 is used in this chapter to investigate factors affecting the neutron energy spectrum. Accurate knowledge of the neutron energies is absolutely essential for converting the measured neutron fluence to dose equivalent, which can then be used to evaluate the degree of risk associated with the exposure.

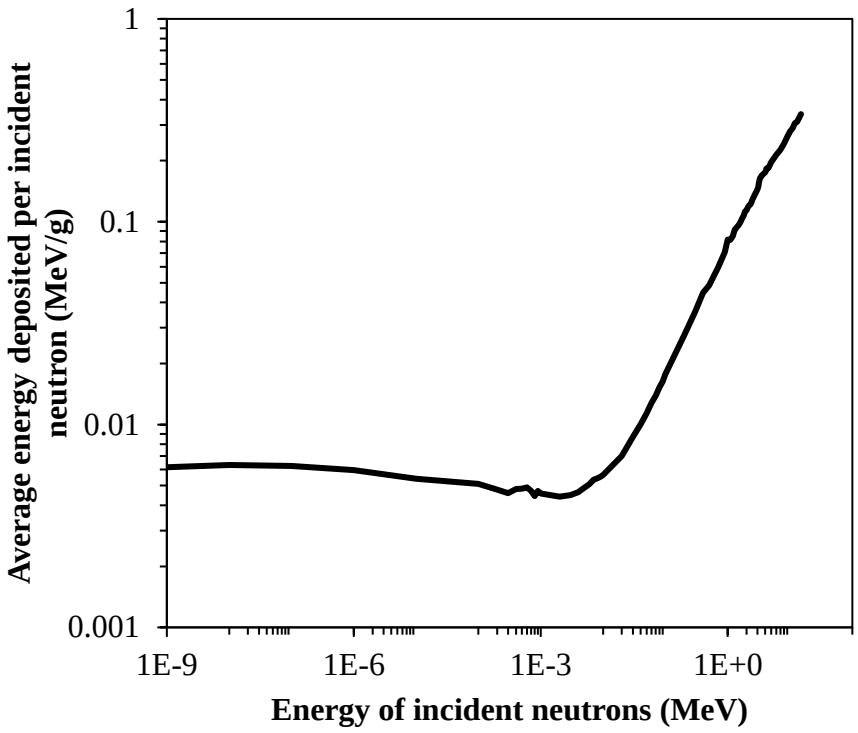

Figure 29: MCNP calculated energy deposited per unit incident neutron fluence in the first centimetre of tissue for monoenergetic neutron sources.

4.3.1 MCNP modelling of a medical linear accelerator

Monte Carlo N-Particle transport code MCNP6 (2013) was used to calculate the energy spectrum of neutrons produced by the photonuclear effect in high energy medical linear accelerators. The production and transport of neutrons in a Varian 21EX operating in 18 MV photon mode were modelled. The model was developed using detailed information about the linac components responsible for the production and collimation of the photon beam (see Figure 30a). This is adequate for simulations which require accurate calculation of the properties of photon or electron beams. For simulations of neutrons, the surrounding materials have great impact on the fluence and energy spectrum of neutrons. Materials adjacent to the neutron producing components scatter and moderate the neutrons and need to be properly accounted for in order to correctly characterise neutron production.

The bremsstrahlung x-ray target is a thin 0.6 mm slab of tungsten attached to a 1.1 cm slab of copper. The electron beam is incident on the tungsten surface and produces photons. The primary collimator is a cylindrical tungsten component with a conical opening for forward transport of photons. The conical angle is 11.3° and the thickness is 7.5 cm. This absorbs any photons not travelling in the forward direction, producing a collimated, directional beam. The open conical region of the primary collimator is under vacuum and so the photon beam must pass through a thin (0.25 mm) beryllium vacuum window. An iron flattening filter with a tantalum core is used to produce a photon beam of uniform fluence. The geometry of the flattening filter is designed to reduce the fluence in the centre where the highest fluence is produced from the target. It has a complex geometry which is modelled explicitly (Varian 1996); the overall shape is approximately conical. The beam then passes through a monitor chamber composed of air, with thin layers of tantalum, kapton, copper and gold. An additional filter, or mirror composed of mylar is placed at an angle of 60° to the beam. Tungsten jaws provide further collimation. There are two sets of opposing slabs 7.6 cm thick which move in the x and y direction to create rectangular field shapes. Below this a multileaf collimator (MLC) which is composed of many independently moving tungsten "leaves" 6.8 cm thick, which can produce photon fields in more complex geometries.

However, there is relatively little information available regarding the shielding and other internal components of linacs. Information useful for the purposes of modelling photon and electron transport (such as phase space files and component geometry) are readily available from linac manufacturers, however the details of out of field shielding components, which are required for neutron transport calculations are difficult to obtain. Measurements were made of the external shielding structure of a Varian 21EX during a scheduled engineering maintenance period (see Figure 30b). Despite these additional details, there was still large spatial volume of which the contents were largely unaccounted for. In practise, this volume is likely a complex mixture of electronic components, vacuum pumps, rails and drivers for the beam shaping components. Without knowing the detailed dimensions and compositions of these components, it is not possible to explicitly model them and calculate their effect on neutron transport and possible influence on the neutron energy spectrum at the patient plane. To assess the magnitude of the effect such components may have, three separate geometries were developed. In the first; the volume between the beam production components and the external shielding components was composed of air (see Figure 31a). In the second it was filled with stainless steel (see Figure 31b) and in the third it was filled with stainless steel at half the density of regular stainless steel to approximate a mixture of components and empty space close to that which probably exists. The scoring region was a 5 cm thick cylinder of air at the face of the linac. The in-field scoring was a rectangular shape lining up with the inner coordinates of the jaws used to create a field size of 10×10 cm^2 at isocentre (defined at 100 cm from the target). Thus, the in-field scoring volume was a cuboid of $5.4 \times 5.4 \times 5$ cm^3. The out-of-field scoring region was a cylinder of radius equal to the outer shielding of the linac head 36.5 cm, and height of 5 cm. It excluded the overlapping volume which was defined as the in-field scoring volume.

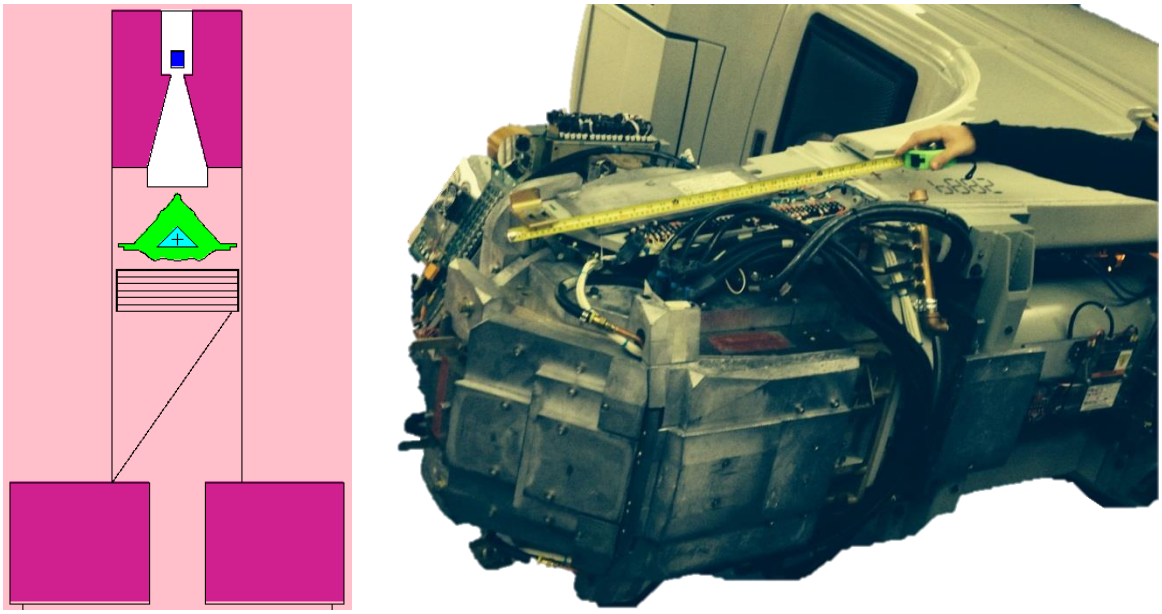

Figure 30: Left: Geometry of the simulated Varian 21EX. Only the primary components used to produce and shape the beam are shown. Right: Photograph of a Varian 21EX with the external covers removed. The shielding in the model was estimated from measurements of the visible components with the external cover of the machine removed.

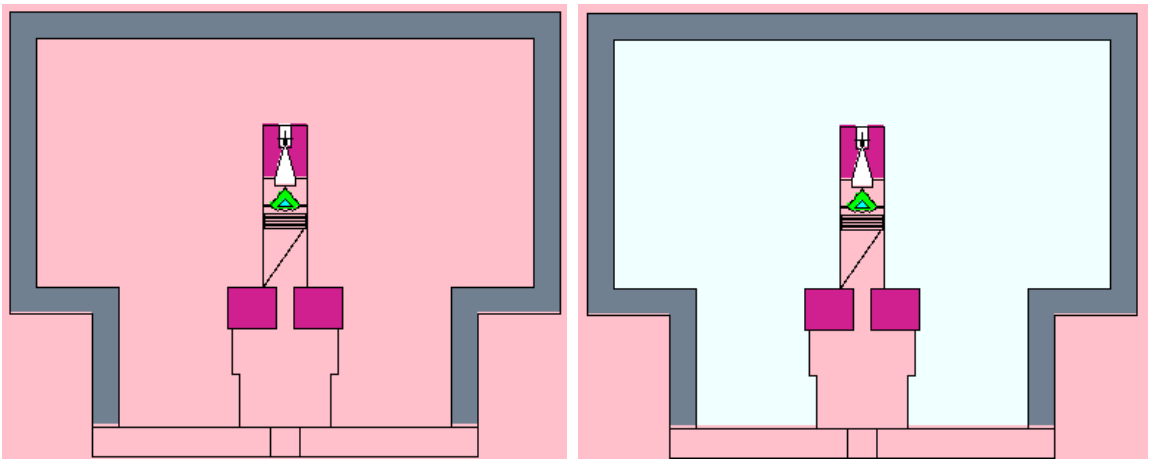

Figure 31: MCNP models of a Varian 21EX with approximate shielding. The space between the shielding and the beam production and shaping components is filled with air (left) and stainless steel (right). A third geometry was also modelled where the stainless steel was modelled with half the density of regular steel.

4.3.2 Variance reduction

The photonuclear yield from bremsstrahlung photons up to 18 MV is relatively low. To achieve a low statistical uncertainty and reduce overall computation time, a number of variance reduction techniques were applied. Table 14 shows the energy thresholds for photonuclear events with target nuclei present in the components of the linear accelerator. For the modelling of the neutron energy spectrum the photon and electron cut off energies were set to 1.6654 MeV which is the threshold for photoneutron production in ^{9}Be, the lowest threshold of the nuclides present. This allows any photons or electrons below this energy to be disregarded, which is justified because they cannot produce any neutrons.

Table 14: Thresholds of nuclides present in MCNP model of Varian 21EX linear accelerator. These values were used to select photon and electron cut off energies. The lowest threshold is for neutron production from ^{9}Be nuclei at 1.6654 MeV (Chadwick *et al* 2011).

Nuclide	Threshold (MeV)	Nuclide	Threshold (MeV)
^{9}Be	1.6654	^{181}Ta	7.57637
^{12}C	18.722	^{182}W	8.2
^{14}N	10.554	^{184}W	7.41138
^{16}O	15.664	^{186}W	7.19537
^{54}Fe	13.4	^{197}Au	8.07137
^{56}Fe	11.1984	^{206}Pb	8.08837
^{63}Cu	10.8524	^{207}Pb	6.73837
^{65}Cu	9.90937	^{208}Pb	7.36737

The secondary particle biasing (SPABI) option in MCNP6 was also utilised to reduce simulation time and improve uncertainties. Secondary neutrons produced by incident photons between 0 and 25 MeV were multiplied by 10^{9} with a corresponding reduction in statistical weight.

4.3.3 Neutron energy spectra

The neutron energy spectra were calculated in a cylindrical cell at the face of the linac. The in-field and out-of-field spectra were scored separately. A 10 × 10 cm^2 field was defined at 100 cm from the target. This corresponded to an MLC opening of 5.4 cm at the linac face. The in-field scoring cell was defined as a 5.4 × 5.4 × 5.4 cm^3 cube at the linac face and the out-of-field scoring cell was a cylinder of the same diameter as the linac face with a height of 5.4 cm. The resultant neutron energy spectra are shown in Figure 32 and Figure 33. The material used to fill the space between the outer shielding and the inner beam producing components has an effect on the overall energy spectrum of neutrons. Most neutrons are produced in the primary collimator (Pena *et al* 2005), but the surrounding material has an effect on the scattering of neutrons, the type and frequency of scattering interactions changes the energy of the neutrons. The results shown here do not show the lower energy peak observed at around 0.05 – 0.08 eV in the spectra reported in literature and shown in Figure 16. However, they agree with the trends shown in the results of Howell *et al* (2006), where the neutron energy spectrum was measured using gold activation foils inside Bonner spheres for a number of treatment energies and modalities at isocentre and at 40 cm superior to isocentre.

The low energy peaks arise from scattering and moderation of the neutron spectrum throughout the treatment room (McCall *et al* 1979). The spectra modelled here show the only the "direct" component of the neutron field at the exit window of the linac head, before ambient scattering has occurred. They are useful to demonstrate the importance of the accuracy of the components modelled. Differences in materials within the linac head have an effect on the energy spectrum calculated. Table 15 shows the mean energies of the in-field and out-of-field spectra calculated with different materials surrounding the linac components. In this high energy range, small differences in neutron energy result in large differences in fluence to dose conversion factors (see Figure 29), and in the response function of LiF TLDs (see Figure 7). The cross sections of activation materials don't generally vary rapidly in this region (see Figure 27).

Approximations in the modelling of a linac, which would have no effect on the more commonly sought photon or electron beam information, can have an effect on the spectrum of neutrons produced. The size and contents of the entire bunker have an effect on the neutron fluence and energy spectrum at the patient plane. The scattered low energy component of the neutron field is inversely proportional to the surface area of the room (McCall *et al* 1979). Larger bunkers, containing more scattering surfaces will have lower neutron fluence overall, however the neutrons present will have a higher mean energy.

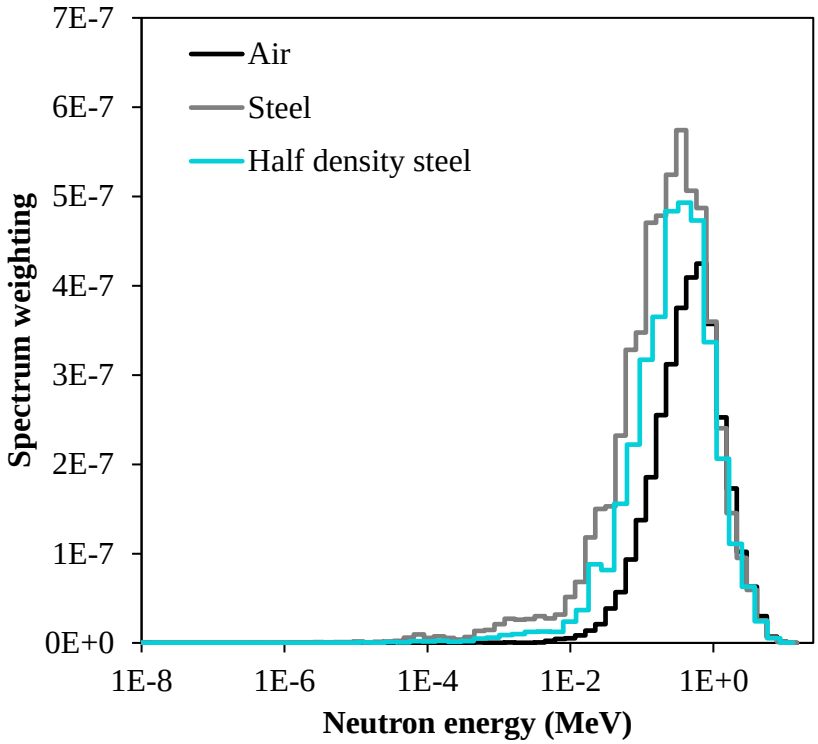

Figure 32: The neutron energy spectrum scored inside the photon field with air, steel and half-density steel filling the space between the linac components producing and shaping the beam and the externally visible shielding components. The spectrum weighting is the number of neutrons within the scoring volume per initial electron simulated on the linac target.

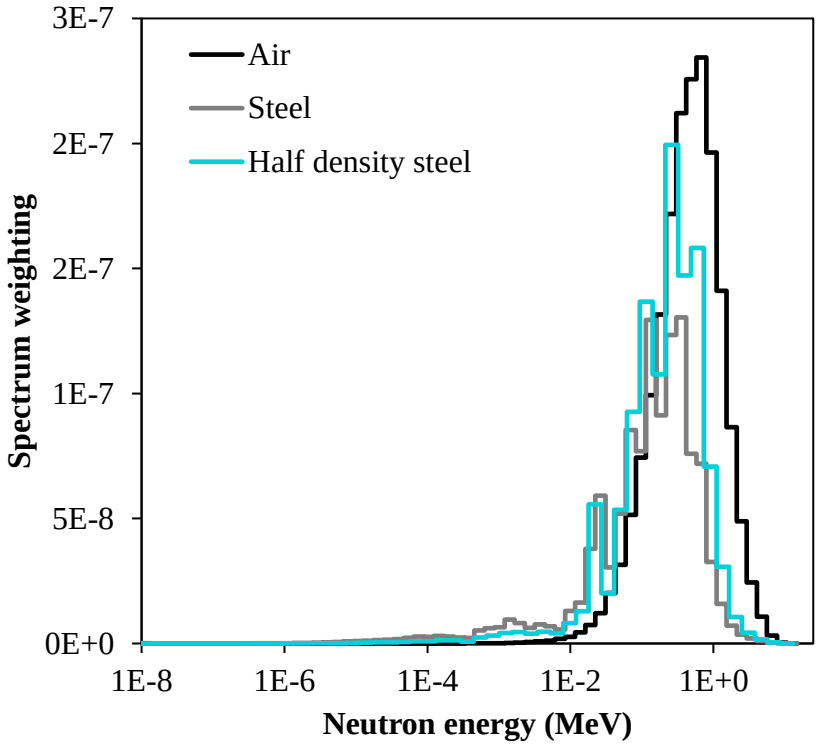

Figure 33: The neutron energy spectrum scored outside the photon field with air, steel and half-density steel filling the space between the linac components producing and shaping the beam and the externally visible shielding components.

Table 15: The mean energies (in MeV) of the spectra shown in Figure 32 and Figure 33.

Energy spectrum	**Mean energy (MeV)**	
	In-field	**Out-of-field**
Air	0.62	0.59
Steel	0.40	0.23
Half density steel	0.43	0.29

The neutron energy spectrum produced by a medical linear accelerator depends on the amount, material and geometry of the shielding surrounding the internal components of the linac. In order to accurately calculate the energy spectrum of neutrons produced in the head reaching the patient plane, detailed information about the shielding is required. In lieu of the required level of detail, a less accurate estimation must be adopted. The size, geometry and composition of the bunker containing the linac also affects the energy spectrum of scattered neutrons. For an accurate measurement of the neutron fluence, as much detail as possible should be included in Monte Carlo models used to determine the neutron energy spectrum produced by a medical linear accelerator.

A best estimate of the neutron energy spectrum will be used in this work to interpret measurements made with thermoluminescence dosimeters and activation foils. Neutron fluence can be measured without knowing the detailed energy spectrum using ^{6}LiF and ^{7}LiF TLD pairs. However, the calibration factor must be corrected for the energy dependence of the higher energy neutrons from the calibration source. The activity of an activated sample can be used to calculate the neutron fluence only if the neutron energy spectrum at the point of measurement is known.

A dose equivalent can be calculated from a fluence and energy spectrum using the fluence to dose function shown in Figure 29. The dose equivalent may then be determined using the ICRP116 (2010) radiation weighting function for neutrons (as shown in Figure 2). These values may then be used for comparison with values reported in literature and evaluation of the risk to the patient resulting from contaminant neutron radiation.

4.4 Relevance to risk from neutron contamination

The methods for implementing neutron dosimetry with ^{6}Li and ^{7}Li enriched LiF TLD pairs and indium and copper activation foils in 18 MV radiotherapy are developed in this chapter. The underlying physics of the chosen detectors is deeply investigated resulting in a robust methodology for interpreting the signals produced by TLDs and activation foils. Monte Carlo simulations of medical linear accelerators and of neutron interactions in detector materials and ICRP soft tissue are presented to give an insight into the complexity of the energy dependence of neutron interactions, neutron dose and therefore the risk from neutrons.

5. Direct risks posed by neutron production

Neutron fluence has been measured as a function of depth in a solid water phantom and as a function of distance from isocentre using both TLDs and activation foils. The results of the two measurement techniques are compared and the differences are used to indicate the level of uncertainty in the measurement of neutrons. The measured fluence is converted to dose with Monte Carlo modelled neutron energy spectra at various depths in solid water and the fluence to dose conversion factors for neutron radiation (Figure 29).

This chapter presents the results of systematic depth and proximity phantom measurements of neutron fluence and the calculation and conversion to dose equivalent. In the previous chapter, the physical mechanisms of neutron interaction and detection were used to describe a robust approach for relating the detector response to neutron fluence. In this chapter, the more mundane details of the method used to perform the systematic measurements such as the irradiation geometry and read out of the detectors is presented to aid in the understanding of the fluence and dose results.

5.1 Methods

5.1.1 Exposure geometries

Two exposure geometries have been used to investigate the neutron fluence as a function of depth in solid water and as a function of distance from isocentre.

To determine the neutron fluence as a function of depth, ten solid water slabs 1 × 30 × 30 cm^3 were placed on the treatment couch and irradiated with a 10 × 10 cm^2 field incident on the one side (see Figure 34). TLD100H, TLD600H, TLD700H and indium and copper activation foils were placed at 1 cm depth increments 10 cm from field edge. This configuration was irradiated by an 18 MV x-ray beam with a $TPR_{20,10}$ of 0.784 from a Varian 21 EX at a gantry angle of 0°. For the TLD exposures the phantom was irradiated to 1,000 MU and for the activation foils the phantom was exposed to 10,000 MU, both at dose rates of 600 MU/min.

For the measurement of neutron fluence as a function of distance from isocentre, solid water slabs were arranged to form a phantom of 120 × 30 × 6 cm^3 in which detectors were placed at a depth of 5 cm (see Figure 35). TLDs were placed in 5 cm increments from the edge of a 10 × 10 cm^2 field and the phantom was irradiated at 18 MV by 1,000 MU at a dose rate of 600 MU/min from a Varian 21 EX at gantry 0°. Indium activation foils were placed in 10 cm increments from the edge of a 10 × 10 cm^2 field and irradiated at 18 MV by 10,000 MU at a dose rate of 600 MU/min from a Varian 21 EX. Two groups of TLDs were irradiated in two separate exposures, one with the collimators aligned at 0° and one with the collimators aligned at 90°. The activation foils were irradiated only once with the collimators aligned at 0°.

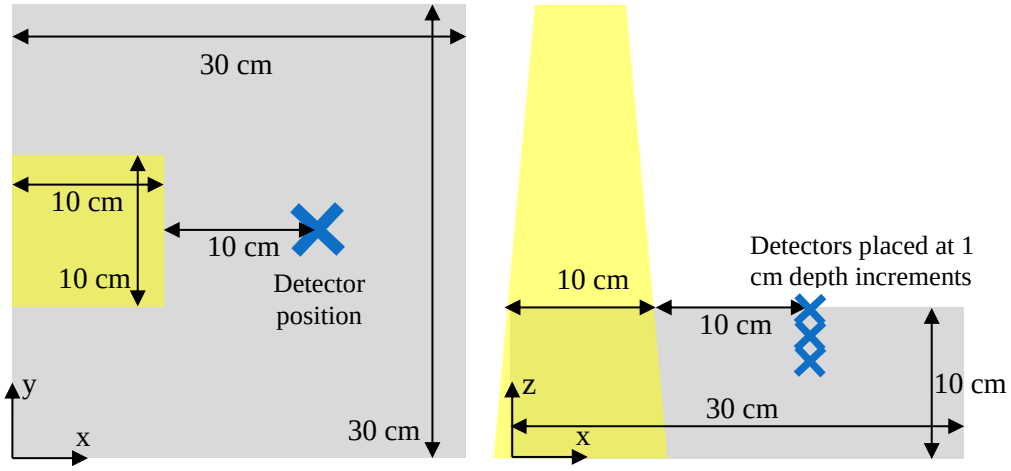

Figure 34: Solid water, x-ray field and detector position configuration. Detectors were placed at 1 cm depth increments from the surface to 7 cm depth. The entire phantom was 10 cm deep.

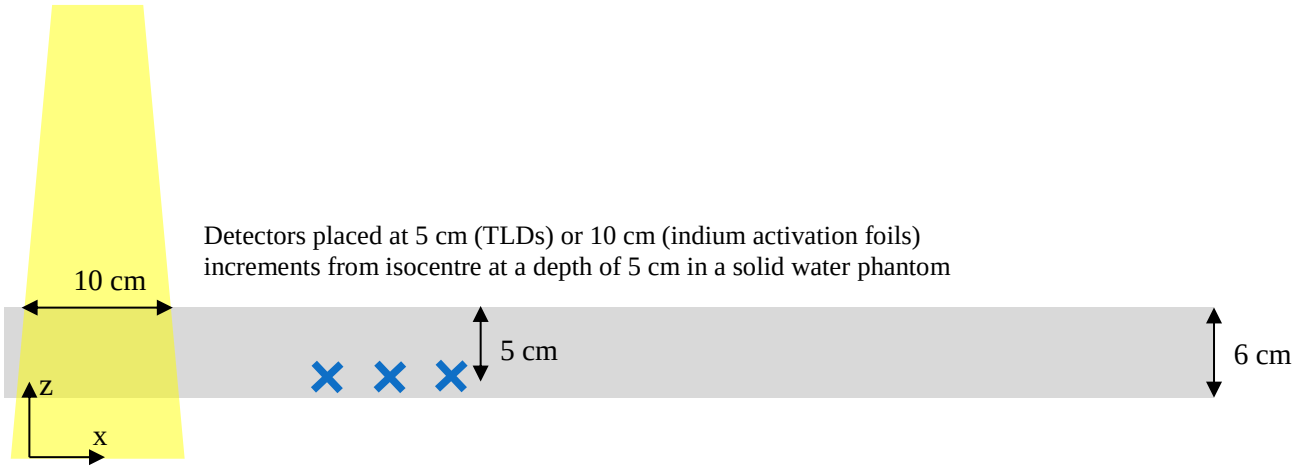

Figure 35: Measurement configuration for out-of-field neutron fluence measurements as a function of distance from isocentre. Detectors were placed at a depth of 5 cm in a 120 × 30 × 6 cm solid water phantom.

5.1.2 MCNP modelling

To determine the cross section values for the activation of the indium and copper foils, Monte Carlo modelling was used to determine the energy spectrum of neutrons incident on the foils at the different depths in solid water.

The moderation of the neutron energy spectrum was modelled in 1 cm depth increments in an A-150 tissue-equivalent plastic (Berger *et al* 2009) phantom beneath a Varian 21EX. The model was designed to match the experimental irradiation geometry as closely as possible. The dimensions of the treatment bunker were measured, and the walls, floor and a ceiling composed of concrete were included in the model. A carbon treatment couch was included below isocentre; with a 30 × 30 × 10 cm^3 solid water phantom positioned such that the centre of a 10 × 10 cm^2 field was 5 cm from one edge of the phantom, replicating the experimental set up as shown in Figure 34. The variance reduction techniques discussed in §4.3.2 were employed to improve simulation efficiency. The neutron fluence was scored in 1 cm cells using MCNP6 standard tally F4 in 40 logarithmic energy bins from 1 × 10^{-8} to 10 MeV.

5.1.3 TLD readout

The TLDs were read on the day following exposure using a Harshaw 5500 automatic reader. The responses are corrected for individual chip variations relative to the average of the TLD batch as determined in a 6 MV photon beam. Four un-irradiated TLDs of each type were also read to determine the background signal. The signal from the irradiated TLD100H, 600H and 700H were corrected for background signals of 2.3, 2.7 and 2.6 nC respectively. The difference between the responses of TLD600H and TLD700H at each depth were taken and multiplied by the calibration factor 7×10^5 ($\pm$ 2 $\times 10^5$) neutrons/cm^2/nC determined in §4.1.3.

5.1.4 Activation measurement

The activities of the foils exposed at various depths in solid water as shown in Figure 34 were measured with the sodium iodide scintillators (NaI(Tl)) described in §4.2.4 between 35 and 60 minutes after irradiation.

The activation foils exposed at distances from the beam isocentre the activity of the indium foils were also measured with a 3 × 3" sodium iodide scintillator, but this time using a portable Ortec DigiBASE-E Ethernet multichannel analyser PMT base (Ametek, USA). The portable nature of the detector allowed the measurement of the foils to occur between 2 and 35 minutes following the irradiation. However, the distance between the activation foils and the detector was less reproducible in the portable set up, which contributes additional uncertainty to the detector efficiency and results in an overall increase in the uncertainty in the calculated neutron fluence.

5.2 Results

5.2.1 MCNP calculated neutron energy spectra as a function of depth in solid water

The MCNP calculated neutron energy spectra in 1 cm depth increments in solid water is shown in Figure 36. These spectra were used to determine weighted neutron interaction cross section values for activation of indium and copper (see Table 16) which are needed to evaluate neutron fluence. They are also used to determine energy weighted fluence to dose conversion factors from the MCNP calculated function shown in Figure 29.

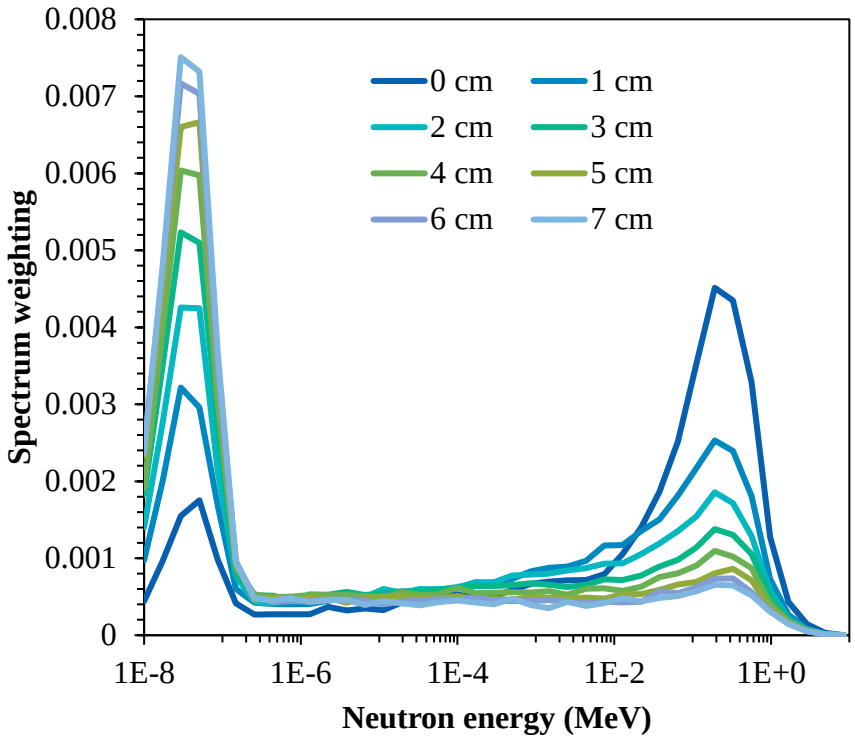

Figure 36: MCNP6 calculated neutron energy spectra at 1 cm increment depths in solid water from an 18 MV Varian 21EX.

Table 16: The weighted average cross sections for indium and copper activation by neutrons with the energy spectra shown in Figure 36.

Depth in solid water (cm)	**^{115}In(n,γ) cross section (cm^2)**	**^{63}Cu(n,γ) cross section (cm^2)**
0	6.17×10^{-23}	6.36×10^{-25}
1	1.02×10^{-22}	1.15×10^{-24}
2	1.28×10^{-22}	1.52×10^{-24}
3	1.49×10^{-22}	1.83×10^{-24}
4	1.59×10^{-22}	2.04×10^{-24}
5	1.66×10^{-22}	2.26×10^{-24}
6	1.66×10^{-22}	2.39×10^{-24}
7	1.68×10^{-22}	2.45×10^{-24}

5.2.2 Neutron fluence as function of depth and distance from isocentre in solid water measured with TLDs and activation foils

The responses of the three TLD types for each irradiation geometry are shown in Figure 37 and Figure 38. TLD600H are enriched in ^{6}Li up to 95.12 % (Saint-Gobain 2001), which has a significantly higher neutron interaction cross section for neutrons with energies below about 2 keV. As expected the TLD600H response was significantly higher than either of the other two types. TLD100H is composed of natural lithium containing 7.59 % ^{6}Li (Rosman and Taylor 1999) shows a slightly higher response than TLD700H containing < 0.03 % ^{6}Li (Saint-Gobain 2001). The difference between the TLD100H and the TLD700H response shows that there is a small portion of the TLD100H response which is due to the presence of neutron radiation. TLD100H are commonly used for x-ray dosimetry. If measurements are made in the presence of neutron radiation, the dose reported may be overestimated as a result of the neutron response of the ^{6}Li in the TLD100H. Kry *et al* (2007a) observed this effect in TLD100 and TLD700 (LiF:Mg,Ti) which have similar lithium concentrations as TLD100H and TLD700H (LiF:Mg,Cu,P). The Mg, Cu, P doped TLD100H are more sensitive than the Mg, Ti doped TLD100 and are more suitable for measuring low doses. Kry *et al* (2007a) recommended that only TLDs enriched in ^{7}Li, with a reduced ^{6}Li concentration be used for out-of-field measurements.

The neutron fluence measured by TLDs at depths in solid water is shown in Figure 39. The maximum fluence is measured at 4 cm depth in solid water. The neutron fluence as a function of distance from isocentre for collimators aligned at 0° and 90° is shown in Figure 40. The fluence measured with the collimators aligned at 90° is consistently lower than that measured at 0° however, the results agree within uncertainty. The consistency of the results might indicate that the trend is the result of a real difference in neutron fluence based on the alignment of the collimator. The asymmetry of the jaws and MLC collimators within the head could possibly result in more or less scatter depending on the arrangement and alignment of these collimators. It is worth noting that a similar trend in out of field photon dose has been previously observed (Taylor *et al* 2011).

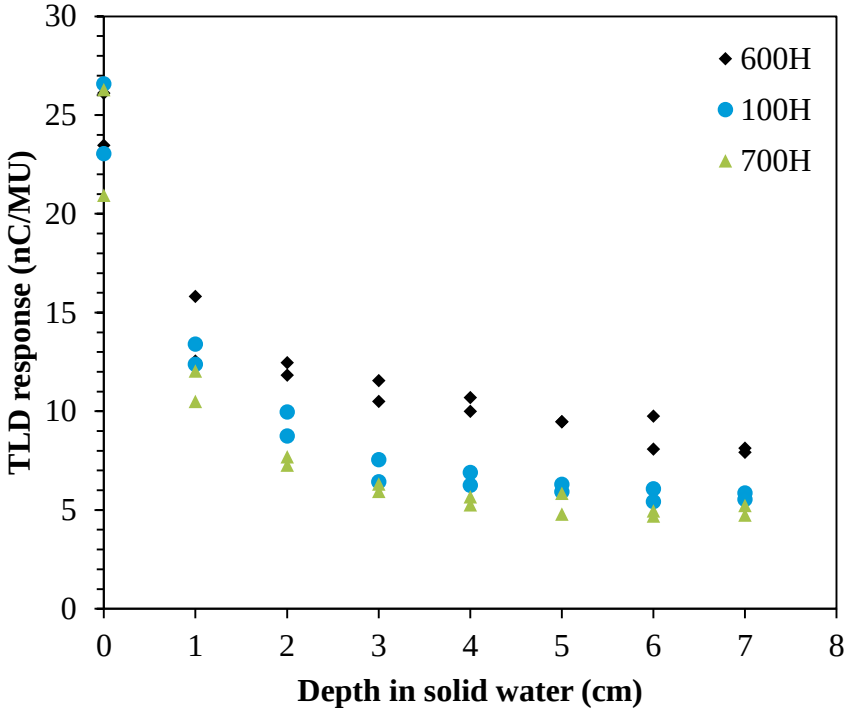

Figure 37: The responses of TLD100H, 600H and 700H per MU delivered. The TLDs were 10 cm from the edge of an 18 MV, 10 × 10 cm^2 field incident on a 30 × 30 × 10 cm^3 solid water phantom. The responses of two TLDs of each type at each position are shown to indicate an estimate of the magnitude of uncertainty associated with the response of a given TLD.

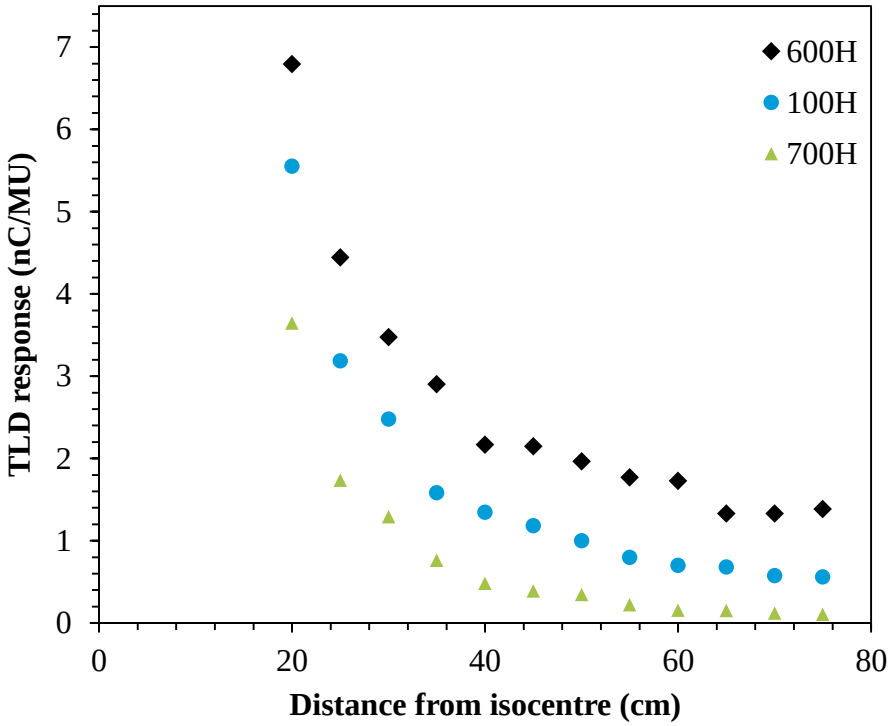

Figure 38: The responses of TLD100H, 600H and 700H per MU delivered with an 18 MV beam delivered with the collimators aligned at 0°.

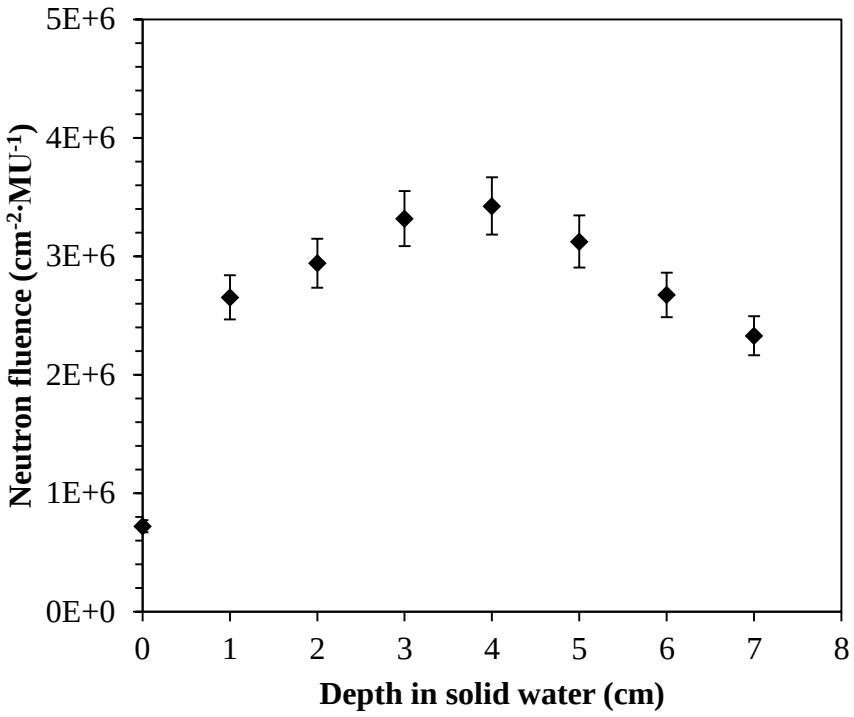

Figure 39: Neutron fluence per monitor unit measured by TLD600H and 700H pairs. The uncertainty is propagated from the uncertainty in the calibration factor only as determined in §4.1.3.

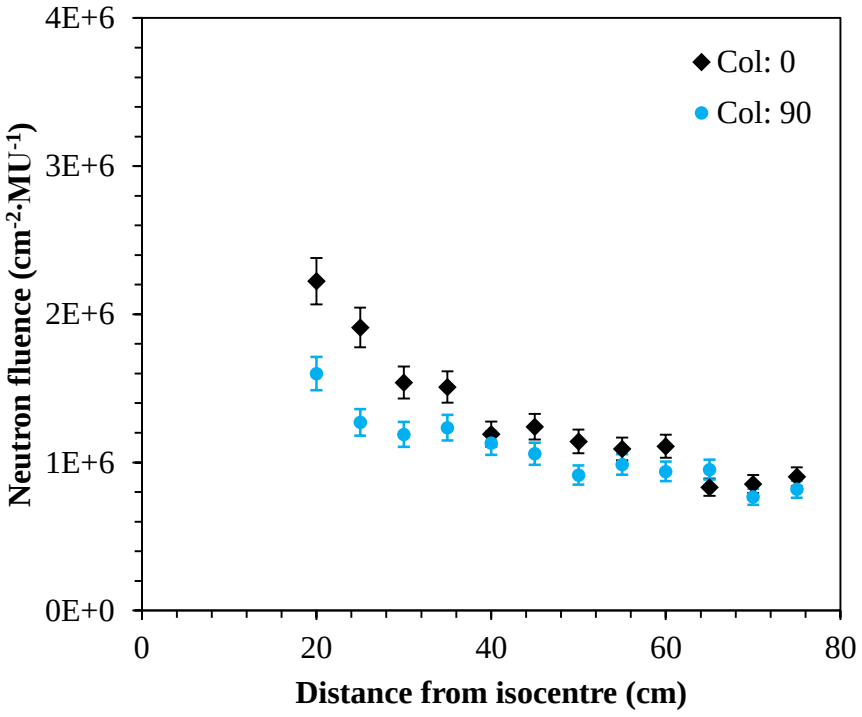

Figure 40: Neutron fluence per MU as a function of distance from isocentre for 18 MV fields delivered with the collimator at 0° and at 90° as measured with TLD-600H and TLD-700H. The uncertainty is propagated from the uncertainty in the calibration factor only as determined in §4.1.3.

The fluence at depths in solid water as measured with indium and copper activation foils are shown in Figure 41 and Figure 42 respectively. The fluence as a function of distance from isocentre measured with indium activation foils is shown in Figure 41.

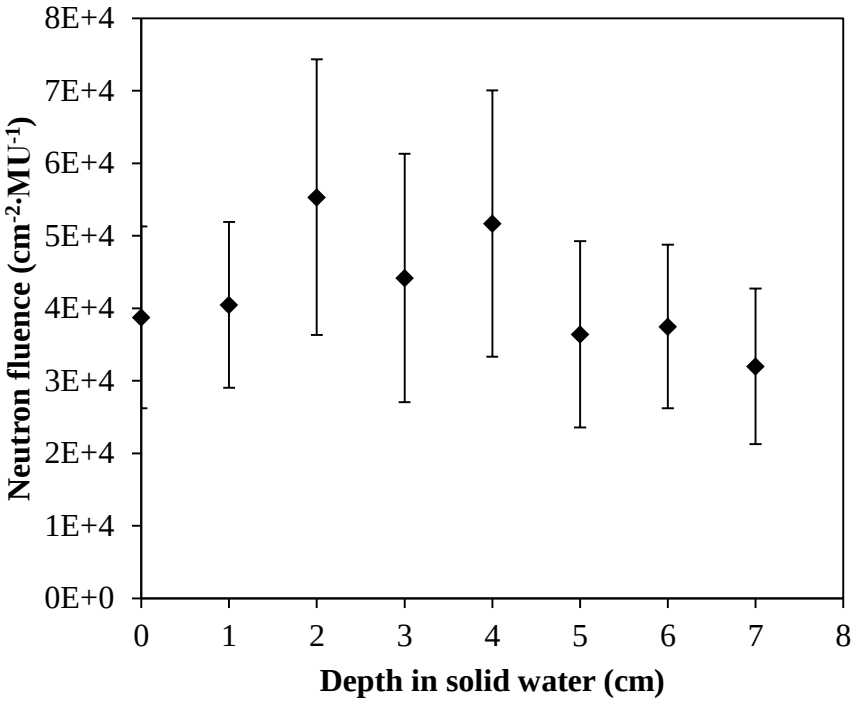

Figure 41: Neutron fluence per monitor unit determined by the activation of indium. The fluence was calculated from the four most prominent gamma-ray peaks and the average and standard deviation of these is shown. The standard deviation is greater than the magnitude of the uncertainty calculated via the quadratic addition of uncertainties.

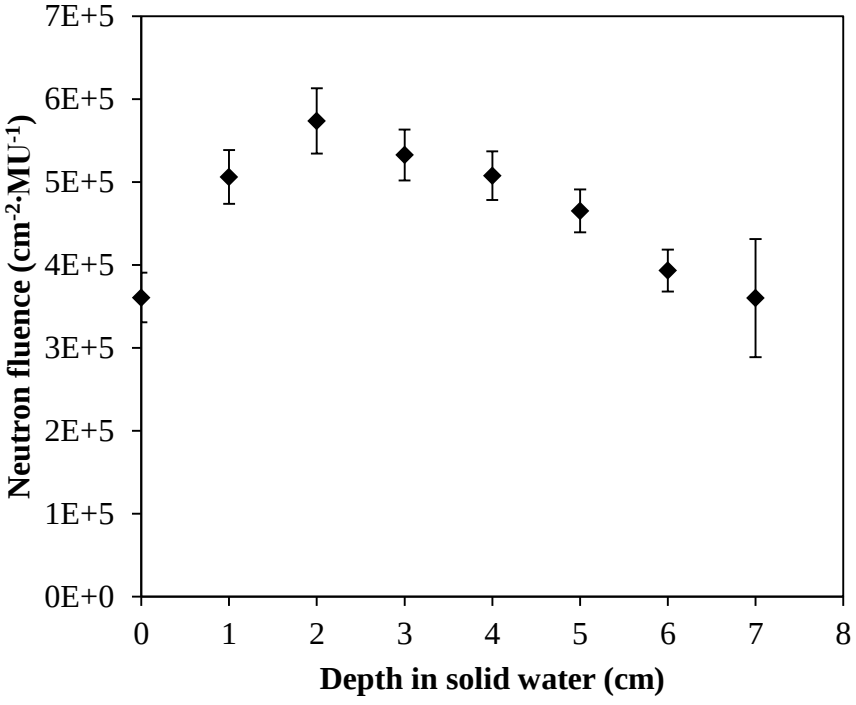

Figure 42: Neutron fluence rate determined by copper activation foils. The magnitude of the error bars was calculated using quadratic addition of uncertainties (see equation 22).

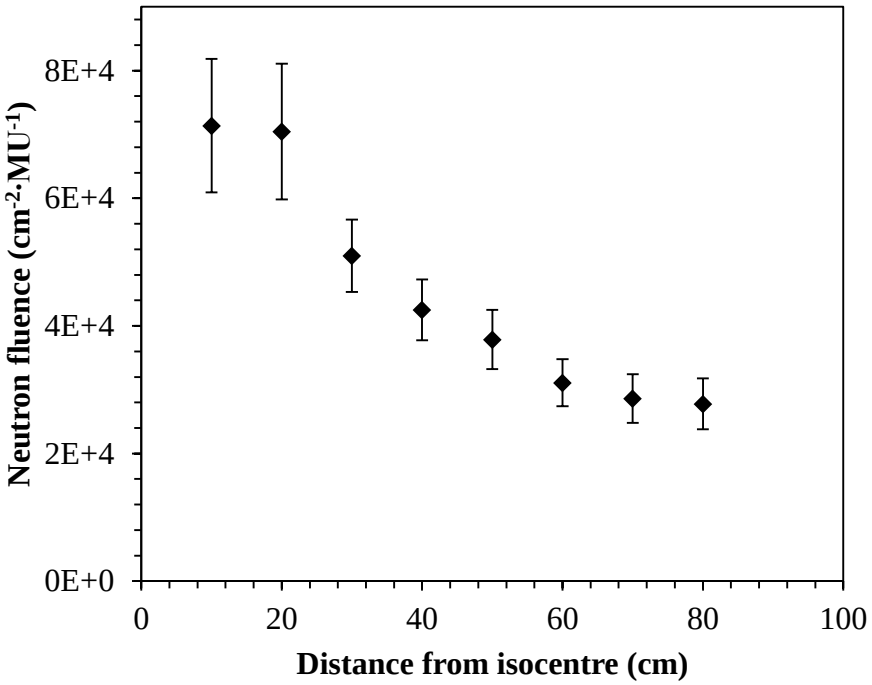

Figure 43: The neutron fluence per MU as a function of distance from isocentre for 18 MV fields delivered with the collimator at 0° as measured with indium activation foils. The fluence was calculated from the four most prominent gamma-ray peaks (416, 818, 1097 and 1294 keV) and the average and standard deviation of these is shown. The standard deviation of the results calculated from the four peaks is greater than the magnitude of the uncertainty calculated via the quadratic addition of uncertainties.

5.2.3 Disagreement between detectors

The large discrepancy between the results obtained with the three different detectors indicates the high degree of uncertainty between each measurement technique as a result of the interpretation of the detector response. The spread of results gives an indication of the order of magnitude of neutron fluence. The results reported here will be compared with those reported in existing published literature in §7.1. The discrepancies observed here will be further discussed in chapter 7. Whilst there is a high degree of uncertainty in the magnitude of the neutron fluence, it is possible to observe consistent trends in the data. The MCNP calculated neutron fluence in Figure 19 (§4.1.5) show a similar shape as depth in tissue increases. The calculated neutron fluence shown in Figure 22 (§4.1.5) indicate a maximum fluence at 2 – 3 cm depth in tissue for linac neutron spectra from literature. Isotopic neutron sources show a maximum fluence at depths of 4 – 6 cm in tissue. Figure 44 shows the trend in the fluence measured in solid water with indium activation foils shows a maximum at 2 – 3 cm, and the copper activation foils show a maximum at 2 cm depth in solid water. The TLD measured fluence shows a maximum at 3 – 4 cm depth. Although the points in Figure 44 and Figure 45 do not explicitly intersect, as the results in Figure 44 are at a distance of 15 cm from isocentre, extrapolating the data in Figure 45 shows agreement of approximately 30 % for the activation foils and TLDs, which indicates reproducibility of the results within the bounds of the discrepancy observed.

The magnitude of the measured neutron fluence as a function of distance from the isocentre also varies with the detector used (see Figure 45). The TLD measured results are consistently about one order of magnitude higher than those measured with activation foils. The trend of fluence decreasing as the distance from the field increases is as expected. The ‘direct’ fast neutrons are expected to decrease with the square of distance from the field, whilst the ‘scattered’ thermal neutrons are expected to be uniform throughout the room (McCall *et al* 1999).

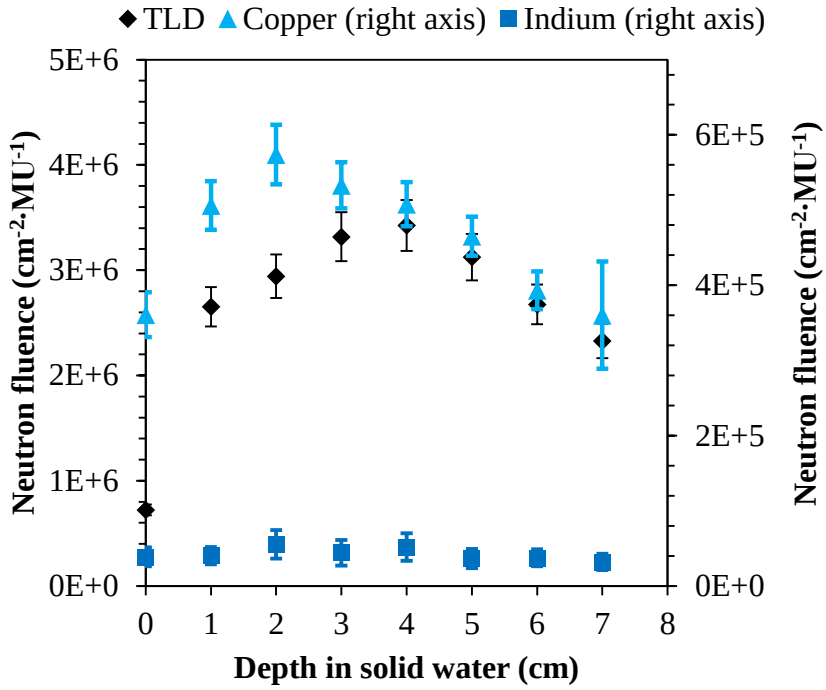

Figure 44: A compilation of results from Figure 39, Figure 41 and Figure 42 which each show the neutron fluence rate as a function of depth in solid water as measured with TLDs, copper activation foils and indium activation foils. The results obtained with the activation foils are significantly lower than those obtained from TLD and have been plotted against the right hand axis so that the trends may be compared.

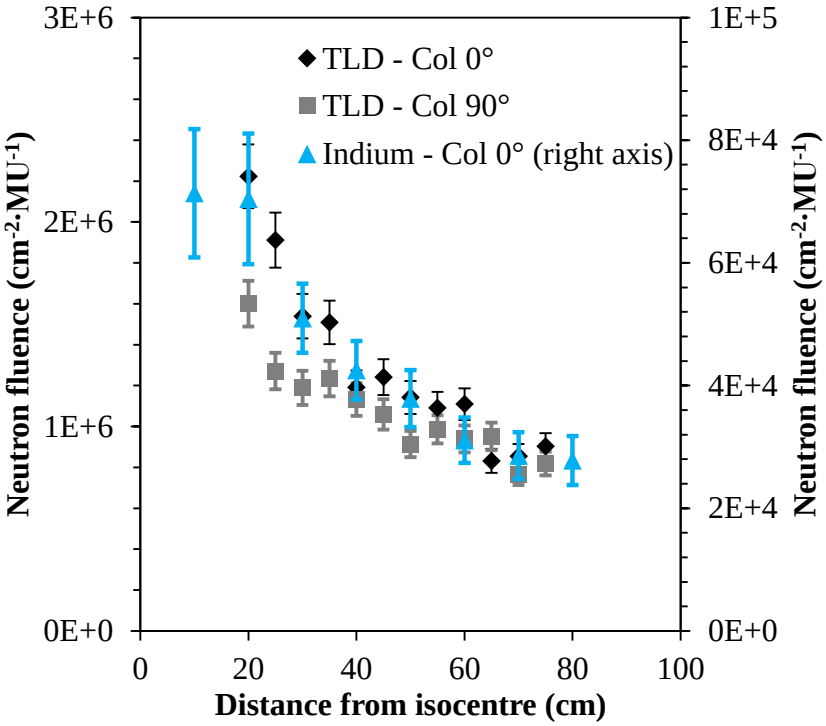

Figure 45: A compilation of results from Figure 40 and Figure 43 which each show the neutron fluence rate as a function of the distance from the isocentre of a photon field as measured with TLDs and indium activation foils. The results obtained with the activation foils are significantly lower than those obtained from TLD and have been plotted against the right hand axis so that the trends may be compared.

The most likely source of the discrepancy between the different detectors is ultimately traceable to the neutron energy spectrum. The TLD responses are uncorrected for energy dependence in this measurement because the energy spectra produced by medical linear accelerators are of low enough energies that the ratio of responses from ^{6}LiF and ^{7}LiF TLD materials is constant (see Figure 18) and as these measurements were taken with solid water build up, the moderated neutrons have even lower energies. The activation foils results rely much more heavily on the modelled neutron energy spectrum. The neutron fluence calculated from the activity of a given foil is inversely proportional to the cross section (see equation 21), which is strongly dependent on the neutron energy spectrum as shown in Figure 27. The results for neutron fluence shown in Figure 44 and Figure 45 were determined using cross section values (shown in Table 16) which were calculated for the MCNP modelled spectra shown in Figure 36.

The cross sections for neutron interactions with ^{115}In and ^{63}Cu are shown in Table 12 for standard isotopically produced neutrons with the energy spectra shown in Figure 12 and for the spectra sourced from published literature shown in Figure 16. The discrepancy between the neutron fluence results obtained from the activity of indium and copper activation foils is potentially the result of uncertainty in the neutron energy spectrum contributing to an error in the cross section value. To explore this possibility a sensitivity analysis was conducted using the same neutron energy spectra as those used to test dose to TLDs in chapter 4. The discrepancy between the two foil materials is expressed as a ratio in the second column of Table 17 below. The ratio is relatively constant with increasing depth indicating that the degree of moderation in the spectra at each depth is modelled consistently. The ratio of neutron fluence calculated from the activities of the copper and indium foils has been recalculated for the cross sections given in Table 12 for the neutron spectra given in the column headings. Whilst this ignores the (not insignificant) moderation of neutron energy with increasing depth in solid water, it is included here to indicate the sensitivity of the fluence results to changes in neutron energy spectrum. For the positions at greater depths in solid water the energies used here are therefore higher than those which would occur realistically, however Table 17 shows that the lower energies result in greater disagreement between the copper and indium activation foils.

Table 17: The ratio of fluence measured with copper activation foils to the fluence measured with indium activation foils. Each column represents the results obtained using cross sections calculated for the neutron energy spectrum given in the column heading. The second column is the ratio of the original data presented in Figure 44, which was calculated from spectra modelled at each depth in solid water. The remaining spectra columns do not account for the moderation at each depth.

Depth (cm)	**Original result (Figure 44)**	**^{241}AmB [1]**	**^{241}AmBe [1]**	**^{252}Cf [1]**	**Isocentre [2]**	**1 metre [2]**	**1.5 metres [2]**	**Air [3]**	**Tissue [3]**
0	9.31	1.35	1.03	1.44	4.38	4.46	4.47	9.78	10.07
1	12.51	1.99	1.52	2.12	6.46	6.57	6.59	14.40	14.84
2	10.37	1.72	1.32	1.84	5.60	5.70	5.72	12.50	12.87
3	12.06	2.08	1.59	2.22	6.76	6.87	6.89	15.07	15.53
4	9.82	1.77	1.35	1.89	5.74	5.84	5.86	12.80	13.19
5	12.78	2.45	1.87	2.62	7.96	8.09	8.11	17.74	18.27
6	10.49	2.12	1.63	2.27	6.90	7.02	7.04	15.39	15.86
7	11.26	2.30	1.76	2.46	7.49	7.61	7.64	16.70	17.20

[1](ISO8529-1 2001) [2](Esposito *et al* 2008) [3](Kry *et al* 2009a)

The neutron fluence, as measured by activation foils of different materials, should be expected to agree for the same irradiation conditions. The ratios of the results obtained from copper and indium foils shown in Table 17 shows an approximately factor of 10 disagreement for the cross sections calculated for the MCNP modelled neutron spectra (Figure 36). When using the cross sections calculated for the neutron spectra from published literature of medical linacs, the results are roughly the same, with slightly better agreement for those from Esposito *et al* (2008) and slightly worse for those from Kry *et al* (2009a). The copper and indium activation foil results agree quite well for the cross sections calculated for high energy isotopic sources, however these energies are unrealistic for neutrons produced by a medical linear accelerator, especially for measurement positions inside a moderating material. These calculations are included to demonstrate the degree of uncertainty in the neutron energy spectrum which would be necessary to explain the discrepancy between the results from the two activation foil materials.

5.3 Results: Conversion to neutron dose equivalent rate

MCNP was used to calculate the dose deposited in a 30 × 30 × 30 cm^3 cube of ICRP tissue in 80 simulations of monoenergetic neutron sources with different energies (Figure 29). These values combined with the neutron energy spectra calculated in one centimetre depth increments in solid water shown in Figure 36 were used to determine neutron fluence to absorbed dose coefficients for the measurements made at depths in solid water. The values for absorbed dose per unit neutron fluence ($pGy \cdot cm^2$) are given in the third column of Table 18. The neutron dose equivalent is also a quantity of interest, because it accounts for the different damage inflicted by neutron radiation compared to other types of radiation. In order to convert the absorbed neutron dose to the neutron dose equivalent, the energy spectra from Figure 36 have been used in conjunction with the energy dependent ICRP103 (2007) radiation weighting factor for neutron radiation which is shown in Figure 2. The resultant radiation weighting factors for each energy spectrum are given in the fourth column of Table 18. Both sets of these values have been separately applied to the neutron fluence results presented in Figure 44 and Figure 45 to produce neutron absorbed doses in Figure 46 and Figure 47 as well as neutron dose equivalents in Figure 48 and Figure 49.

Table 18: Fluence to absorbed neutron dose conversion factors calculated in this study using MCNP for a variety of neutron energy spectra. The radiation weighting factors corresponding to each of these spectra is also given and has been calculated from the neutron radiation weighting factor function given in ICRP116 (2010). The absorbed dose per neutron and radiation weighting factors combined give the neutron dose equivalent per unit fluence.

Neutron spectrum	**Mean energy (MeV)**	**Dose per neutron fluence (pGy·cm^2)**	**Radiation weighting factor w_R**	**Dose equivalent per neutron fluence (pSv·cm^2)**
^{241}AmB [1]	2.63	21.9	15.7	343
^{241}AmBe [1]	4.05	26.2	13.7	358
^{252}Cf [1]	1.98	17.6	16.8	296
Isocentre [2]	0.510	7.84	15.7	123
1 metre [2]	0.310	5.73	14.2	81.2
1.5 metres [2]	0.267	5.09	12.7	64.6
Air [3]	0.249	4.75	10.6	50.2
Tissue [3]	0.146	3.21	7.52	24.2
Depth in solid water [4]				
0 cm	0.185	4.03	9.62	38.8
1 cm	0.107	2.72	6.71	18.2
2 cm	0.081	2.27	5.59	12.7
3 cm	0.065	2.01	4.89	9.82
4 cm	0.055	1.83	4.44	8.13
5 cm	0.047	1.69	4.07	6.89
6 cm	0.040	1.60	3.85	6.15
7 cm	0.038	1.55	3.74	5.82

[1] (ISO8529-1 2001) [2] (Esposito *et al* 2008) [3] (Kry *et al* 2009a) [4] This study, shown in Figure 36.

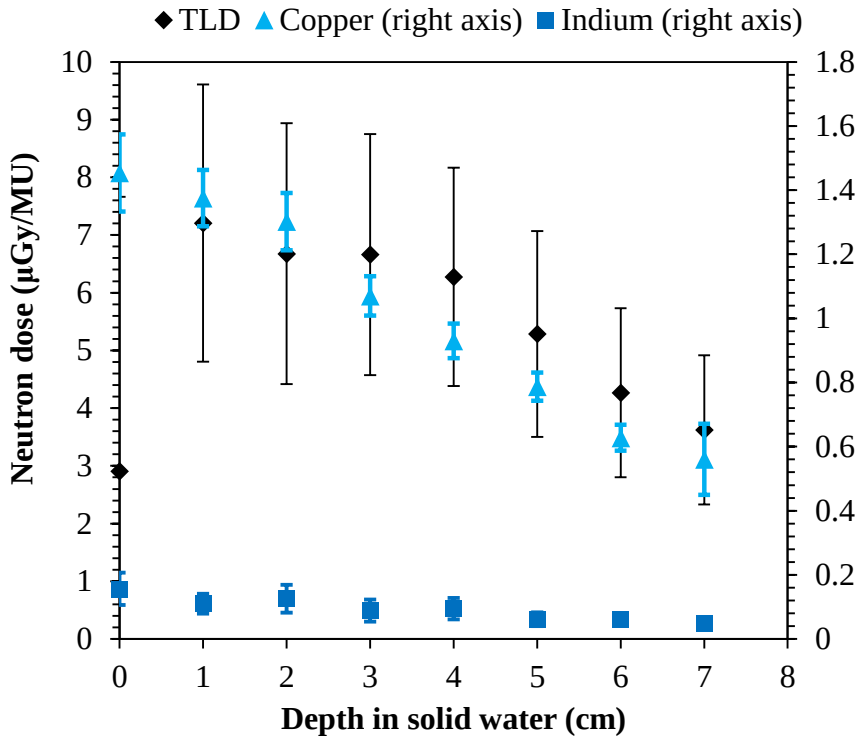

Figure 46: Absorbed dose from neutron radiation as a function of depth in solid water out-of-field of an 18 MV photon beam. The data is measured using ^{6}LiF and ^{7}LiF TLD pairs and indium and copper activation foils. The dose is calculated using the conversion factors presented in Table 18.

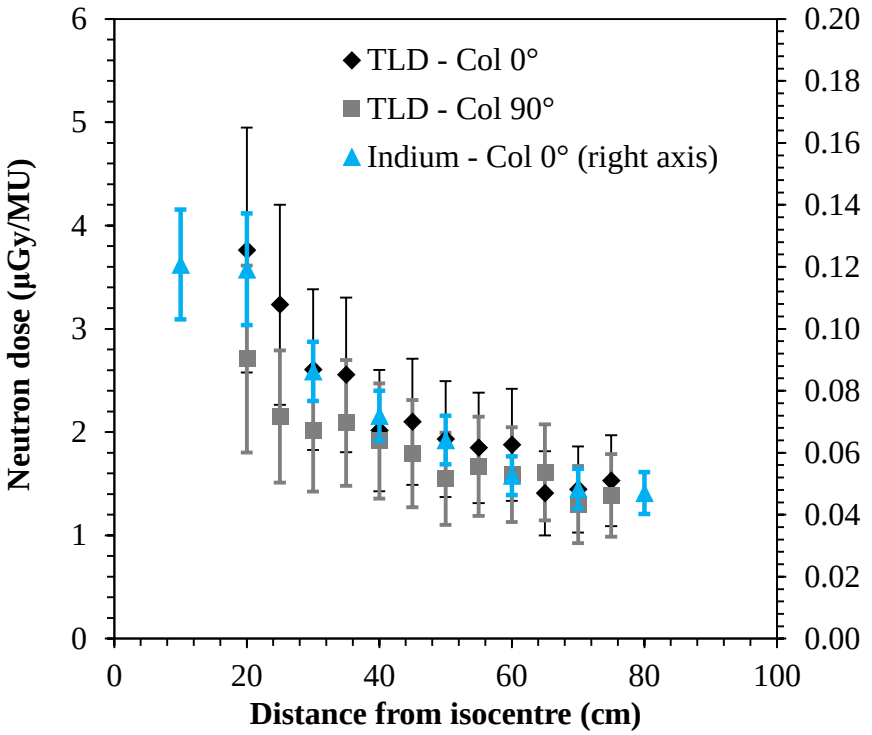

Figure 47: Absorbed dose from neutron radiation as a distance from the field edge of an 18 MV photon beam. The data is measured using ^{6}LiF and ^{7}LiF TLD pairs and indium activation foils. The dose is calculated using the conversion factors presented in Table 18.

The neutron dose equivalent is essential to assess the magnitude of the risk to patients potentially treated with 18 MV x-ray beams. The dose equivalent quantity allows inter comparison of the biological effects, and hence, risk resulting from irradiations by different types of radiation. It also allows comparison with this work and existing published literature, because it is the quantity most often reported. For the highest degree of clarity possible, all factors used to convert between neutron fluence, absorbed neutron dose and neutron dose equivalent in this work are presented in Table 18.

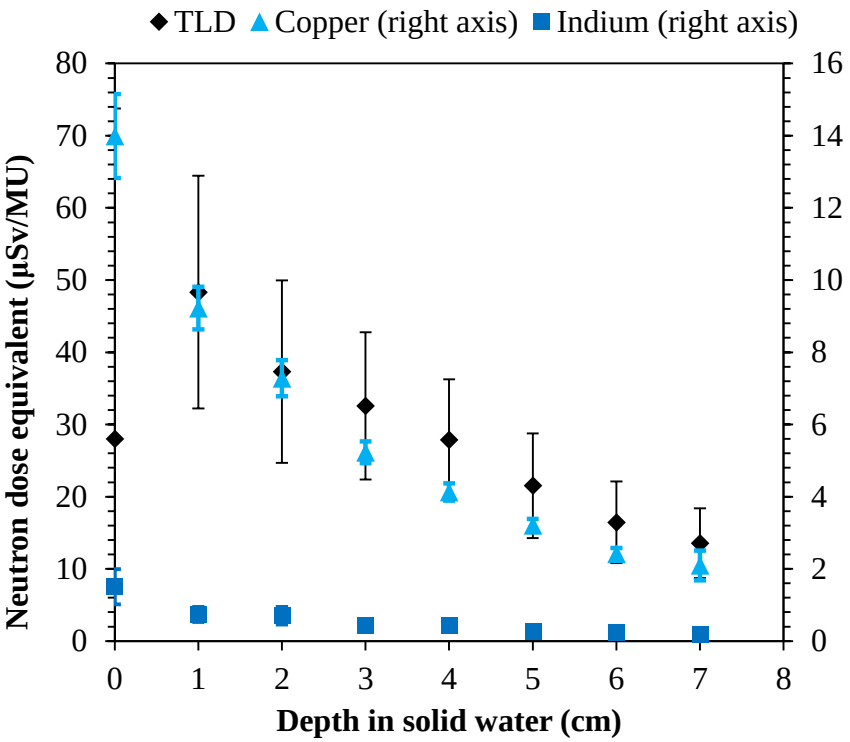

Figure 48: Neutron dose equivalent from neutron radiation as a function of depth in solid water out-of-field of an 18 MV photon beam. The data is measured using ^{6}LiF and ^{7}LiF TLD pairs and indium and copper activation foils. The dose equivalent is calculated using the conversion factors presented in Table 18.

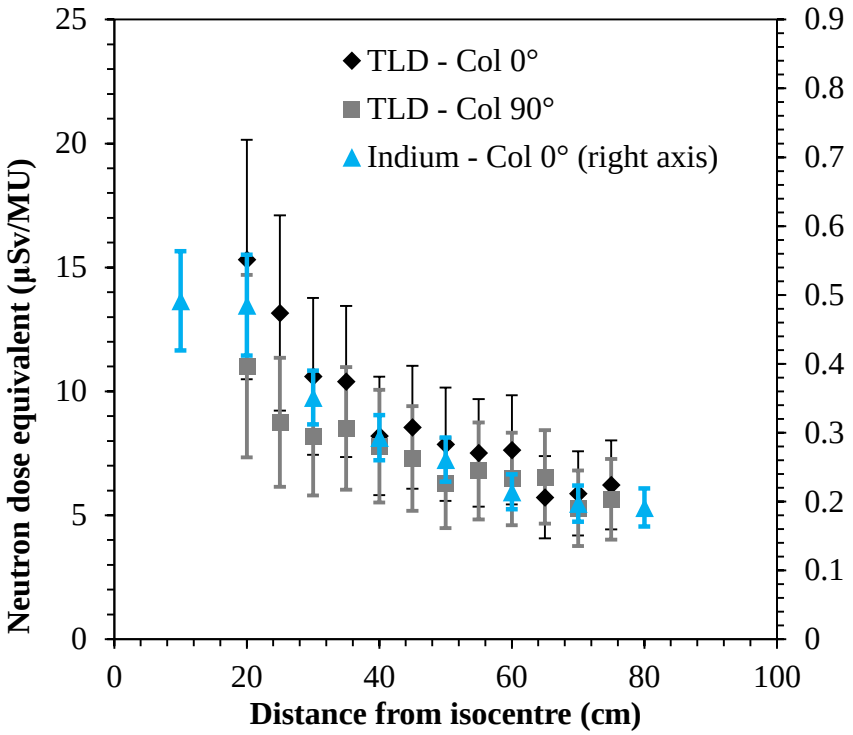

Figure 49: Neutron dose equivalent from neutron radiation as a distance from the field edge of an 18 MV photon beam. The data is measured using ^{6}LiF and ^{7}LiF TLD pairs and indium activation foils. The dose equivalent is calculated using the conversion factors presented in Table 18.

As discussed in §5.2.3, there is a significant degree of variation in values obtained from the different detectors employed in this study. For the purposes of discussion of the magnitude of the neutron dose an indicative range of values will be selected. The maximum neutron dose equivalent observed was 48 µSv/MU, as calculated from the responses of a pair of ^{6}LiF and ^{7}LiF TLDs placed at 1 cm depth in solid water at a distance of 10 cm from the edge of a 10 × 10 cm^2 18 MV field. A minimum value of 0.74 µSv/MU as measured with indium activation foils at the same location as the maximum TLD result.

5.4 Summary of the relevance to risk from neutron contamination

The results of neutron measurements in solid water phantoms are presented in this chapter. The measurement of neutrons in phantoms is used as a proxy to indicate the dose a patient might receive during 18 MV radiotherapy. Quantifying the neutron fluence rate allows the absorbed dose to tissue from neutron exposure to be determined. From this, the neutron dose equivalent can be determined. The resultant risk to a patient can be discussed in a quantitative manner from the neutron dose equivalent information presented.

6. Indirect risks posed by neutron production

Neutrons produced *via* the photonuclear effect in high energy radiotherapy may be incident on all objects within a medical linear accelerator bunker. The most immediate concern is the risk to the patient. However, there are secondary effects which may also pose a risk to staff and equipment. Production of neutrons by high energy photons may result in activation of the target nuclei of the interaction. These neutrons may then interact with otherwise stable nuclei and cause further activation. Components within a medical linear accelerator operating at high energies can become radioactive and remain so after termination of the beam. The risk this poses is of greater relevance to radiotherapy staff who may be in close proximity to a linac frequently throughout their work. Neutrons incident on patients during treatment are of concern because of their high radiobiological effect (RBE). Neutron interactions within patients are unlikely to cause a high degree of activation because interaction with tissue resulting in residual activity have lower cross sections (see Figure 1, §2.2). However, patients with metallic implants undergoing radiotherapy are at risk of activation of the implanted object. Electronic implants such as pacemakers may be damaged and malfunction due to radiation exposure (Zaremba *et al* 2015). Hip prostheses may be activated by incident neutrons or high energy photons directly from the treatment beam.

Two specific cases have prompted specific concerns from treating staff and are worthy of individual investigation. This chapter describes the application of established conventional methods for gamma ray spectroscopy and TLD photon dosimetry to quantify the degree of activation in linacs and prosthetic hips. The isotopes produced are identified with gamma spectroscopy and the resulting doses are determined from ion chamber and TLD measurements. The work in this chapter has also been published in peer reviewed journals; please see Keehan *et al* (2015) and (Keehan *et al* 2017).

6.1 Activation of the components in the linear accelerator

Medical linear accelerators operating above 7-8 MeV produce contaminant neutrons through photonuclear interactions in which a high energy photon causes the emission of a neutron. The loss of a neutron for some nuclei renders them unstable and radioactive. The extent of the activation depends on the number of monitor units (MU) delivered at high energies. Treatment techniques that require a higher number of MU produce a higher level of activity. Total body irradiation (TBI), intensity modulated radiotherapy (IMRT), volumetric modulated arc therapy (VMAT) and stereotactic ablative body radiotherapy (SABR) typically require long beam times and can benefit from being delivered at high energies. TBI requires a very large field size, whilst IMRT, VMAT and SABR are typically delivered as small fields. For small fields there is a larger mass of collimating material intersecting the beam, which provides shielding against secondary radioactivity produced after the beam is terminated. The large fields of TBI require the collimators to be fully open for the delivery of the beam. If the jaws remain open at termination of the beam, the absence of shielding results in a higher dose rate at the beam exit window of the linac. The relevant isotopes are identified in this section, and the measurements of the resultant doses at representative positions are presented.

6.1.1 Methods

6.1.1.1 Methods for identifying the radioisotopes produced in linac components

Gamma-ray spectroscopy was used to identify radioisotopes present following termination of 18 MV beams from a Varian 21EX and an Elekta Synergy. A 3 × 3 inch sodium iodide (NaI(Tl)) scintillation detector (Saint-Gobain, France) and Ortec DigiBASE-E Ethernet multichannel analyser PMT base (Ametek, USA) were calibrated with the characteristic gamma-ray emissions of ^{137}Cs, ^{22}Na and ^{60}Co. The detector was then placed on the treatment couch, with the centre of the crystal at 100 cm SDD. Spectral measurements were acquired after 8 hours (Varian) and 4 hours (Elekta) of typical use at multiple energies (Figure 51). Spectra were also measured from one minute following 500 MU delivered at 18 MV from each linac (Figure 52). The detector was removed from the room whilst the beam was delivered and placed at isocentre within one minute of the beam termination to avoid any afterglow effects.

Gamma-ray spectra were also measured immediately following the delivery of 18 MV electron beams. A 25 × 25 cm^2 applicator was used to deliver 10,000 MU at a dose rate of 1,000 MU/min. The spectrum measured following this beam is compared to that measured following an 18 MV photon beam in Figure 53. For comparison, an 18 MV electron beam was also delivered in service mode without the presence of an applicator.

6.1.1.2 Methods for determining doses resulting from activation of the linac head

The photon dose rate directly under the beam exit window of the Varian linac was measured using a PTW 32002 1 litre spherical ion chamber (Freiburg, Germany). The chamber has a polyoxmethylene wall and graphite coated polystyrene central electrode.

The dose rates were measured with the jaws remaining open (40 × 40 cm^2) after each of four 2197 MU beams from a Varian 21EX were delivered to a patient as part of an 18 MV total body irradiation treatment on two consecutive days. The treatment was the first of the day, and background measurements were taken after pre-treatment machine testing/warm-up, before any treatment beams were delivered. Two twenty minute measurements were taken for each of two treatment fractions, following left and right lateral deliveries (see Figure 50) of 2197 MU each at a dose rate of 200 MU/min. The chamber was set up on the treatment couch out of the beam, and moved into place just after termination of the beam. To estimate the dose rate received by a radiation therapist attending the patient at the TBI treatment couch, dose measurements at this position, 4.8 metres from the linac face, were also taken.

To investigate correlation between the amount of collimation and the level of induced activity 10,000 MU were delivered with the jaws open to 40 × 40 cm^2 and closed to 0.5 × 0.5 cm^2. Measurements were also made outside of the closed jaws to quantify the benefit of the attenuation provided by the jaws.

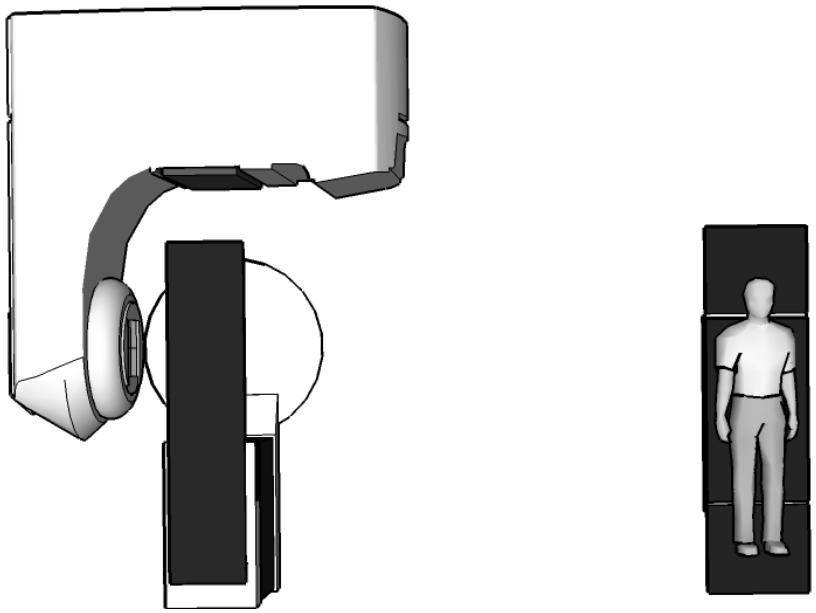

Figure 50: Right lateral total body irradiation geometry viewed from above. The gantry was rotated 90° and the patient was positioned on a TBI treatment couch at the edge of the treatment room, 4.8 meters from the linac face.

6.1.2 Results

6.1.2.1 Results for identifying the radioisotopes produced in linac components

Gamma spectra were acquired from a Varian linac after 8 hours and from an Elekta linac after 4 hours of typical use at multiple energies (Figure 51). Spectra were also measured from within one minute following a delivery of 500 MU at 18 MV from a Varian and an Elekta (Figure 52). The spectra shown in Figure 51 are subtracted from those shown in Figure 52 in order to show the activity generated during the 500 MU delivery only.

The spectrum measured following an electron beam of 10,000 MU delivered at 18 MeV is shown in Figure 53. An 18 MV electron beam was also delivered in service mode without the presence of an applicator. The spectrum measured following this beam is compared to that measured with an applicator in place in Figure 54.

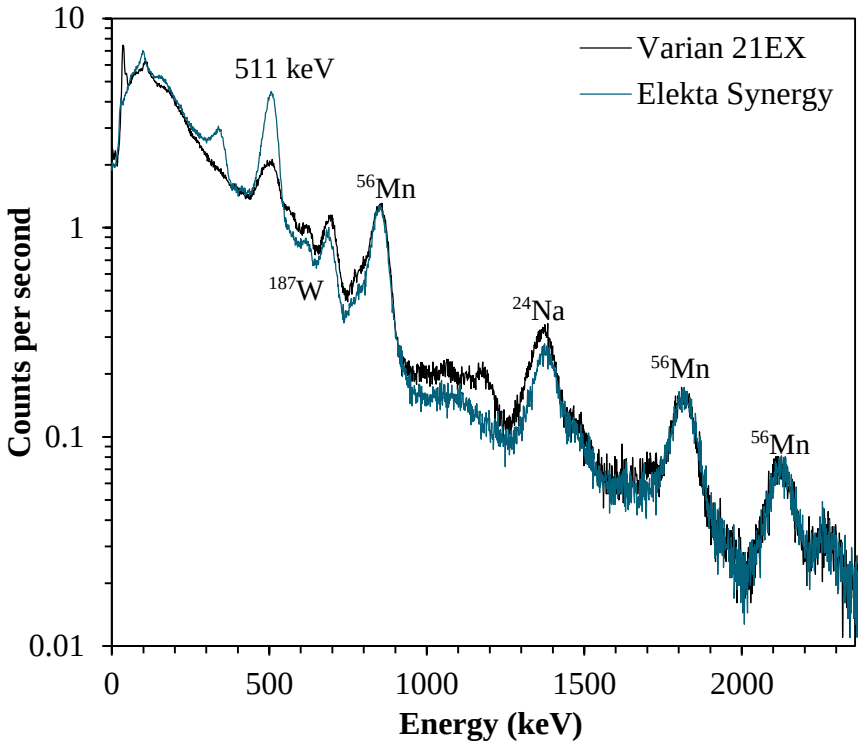

Figure 51: Gamma-ray spectra measured at 100 cm SDD following ~8 hours of typical use at multiple energies for the Varian 21EX and ~4 hours of typical use at multiple energies for the Elekta Synergy.

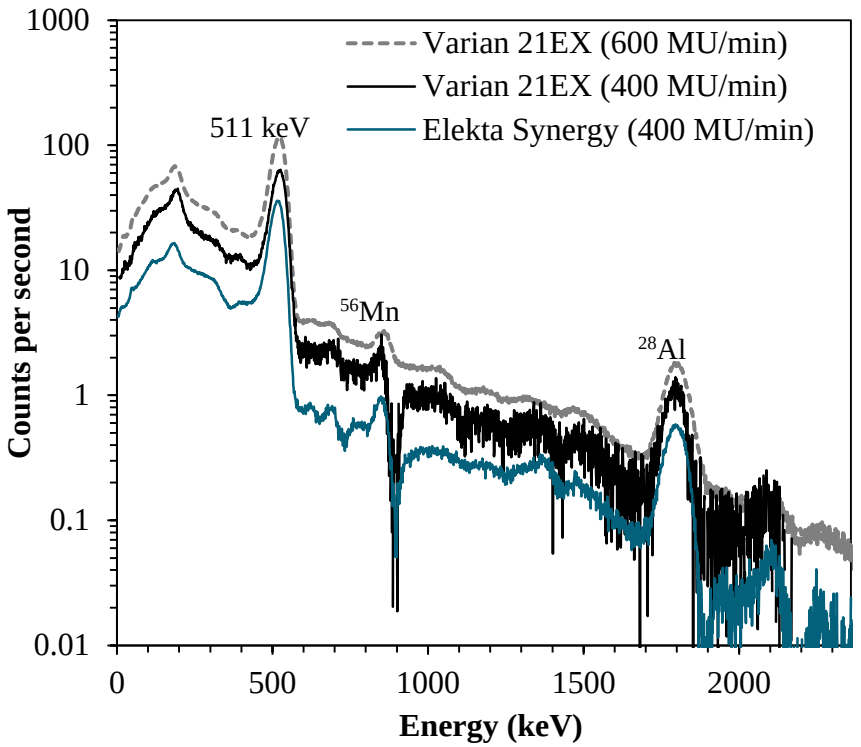

Figure 52: Gamma-ray spectra measured at 100 cm SDD following 500 MU photon beams delivered at 18 MV. The beams from the Varian 21EX were delivered at dose rates of 600 MU/min and at 400 MU/min. The Elekta Synergy beam was delivered at 400 MU/min only. The detector was placed on the couch within one minute of termination of the beam and spectra were acquired for forty minutes. The spectra shown in Figure 51 were subtracted.

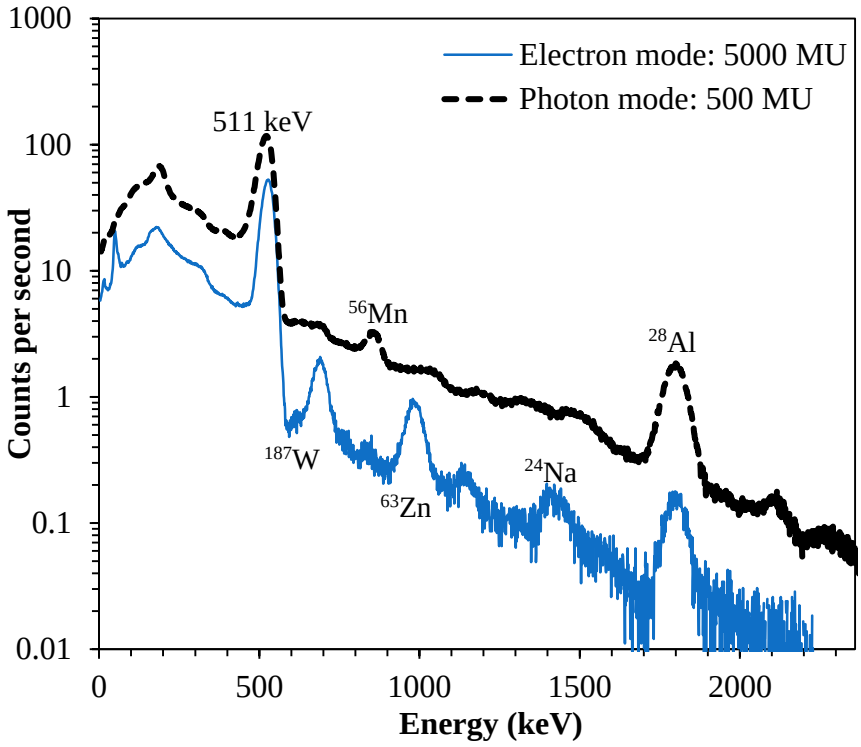

Figure 53: The spectrum measured following an 18 MV electron beam of 10,000 MU at a dose rate of 1,000 MU/min. The spectrum measured following 500 MU of an 18 MV photon beam at 600 MU/min from Figure 52 is shown for comparison of the difference in the magnitude of the activity.

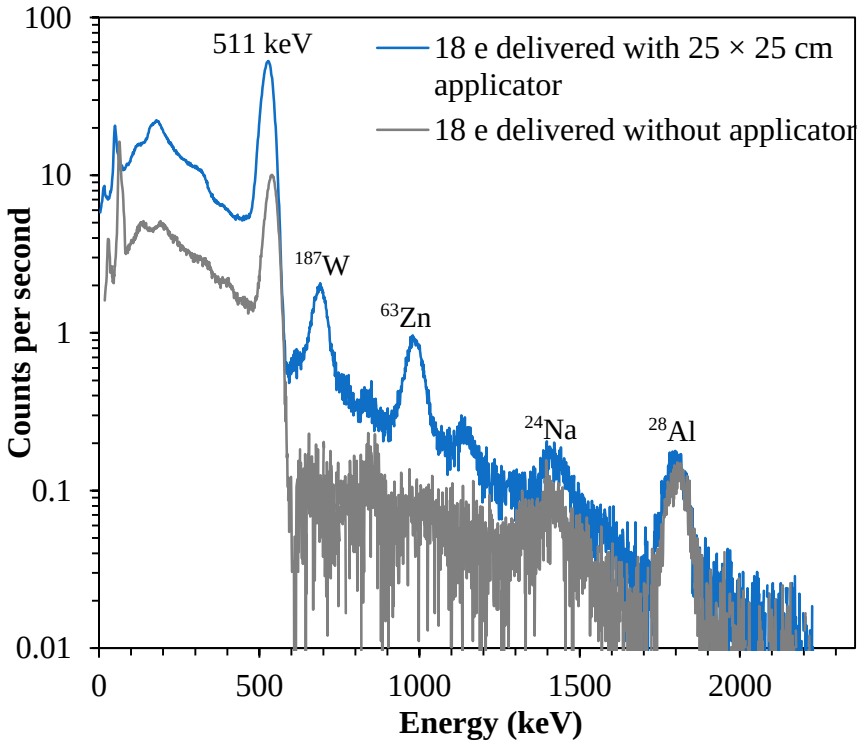

Figure 54: Spectra measured following 10,000 MU delivered at a dose rate of 1,000 MU/min in 18 MV electron mode. One beam was delivered with a 25 × 25 cm^2 applicator in place and the other in linac service mode without an applicator in place.

The isotopes identified from their characteristic gamma-ray energy peaks in Figure 51, Figure 52, Figure 53, and Figure 54 are shown in Table 19. The 1779 keV peak from ^{28}Al (with half-life 2.3 minutes) is only visible in the spectra acquired immediately following termination of the 18 MV beam (Figure 52). The peaks of the longer lived ^{187}W, ^{56}Mn and ^{24}Na are not visible in Figure 52 but appear after the short lived activation products have decayed (Figure 51). The gamma-ray spectra measured following electron beams had much lower count rates (by a factor of ~250) and thus activity than those measured following photon beams, see Figure 53. The spectra in Figure 53 are not normalised to the number of monitor units delivered in each beam because the level of activation is dependent on the dose rate and total time for beam delivery as well as the half-lives of the isotopes produced. The activation is not linearly related to the number of monitor units. The lower activity observed following the electron beams is expected because the cross sections for direct electro-nuclear events are estimated to be of the order of the fine structure constant, 1/137, compared to the cross sections for photonuclear interactions (McCall *et al* 1984). The 962 keV gamma peak of ^{63}Zn shown in Figure 54 is only present in the spectrum measured with the electron applicator present.

Table 19: Isotopes identified in the spectra shown in Figure 48, Figure 49, Figure 50, and Figure 51.

Isotope	Energy (keV)	Half-life	Interaction
^{187}W	686	24 hours	(n,γ)
^{63}Zn	962	38 min	(γ,n)
^{56}Mn	847, 1811, 2113	2.6 hours	(n,γ)
^{24}Na	1369	15 hours	(n,γ)
^{28}Al	1779	2.3 min	(n,γ)

6.1.2 Doses resulting from activation of the linac head

The dose rate was measured following left and right lateral beams delivered during a patient TBI. The left lateral beams were delivered first, followed by the right lateral beams. The dose rate measured after the second of the lateral beams is always higher than after the first beams because of the accumulation of activity. The dose rates measured on the first day showed an overall lower activity than on the second day, because an interlock occurred during this delivery which resulted in the initial beam being interrupted. The beam was off for approximately one minute while the interlock was checked and recorded before the remaining monitor units were delivered. During this time isotopes continue to decay whilst no more are being produced resulting in an overall lower activity when all monitor units had been delivered.

The patient is positioned near the bunker wall for the TBI, and this is typically where staff stand when they first enter the room to attend to the patient. Further dose measurements were taken at the patient location (4.8 m away from the beam exit window ('■' in Figure 55) to provide more realistic dose information for concerned staff.

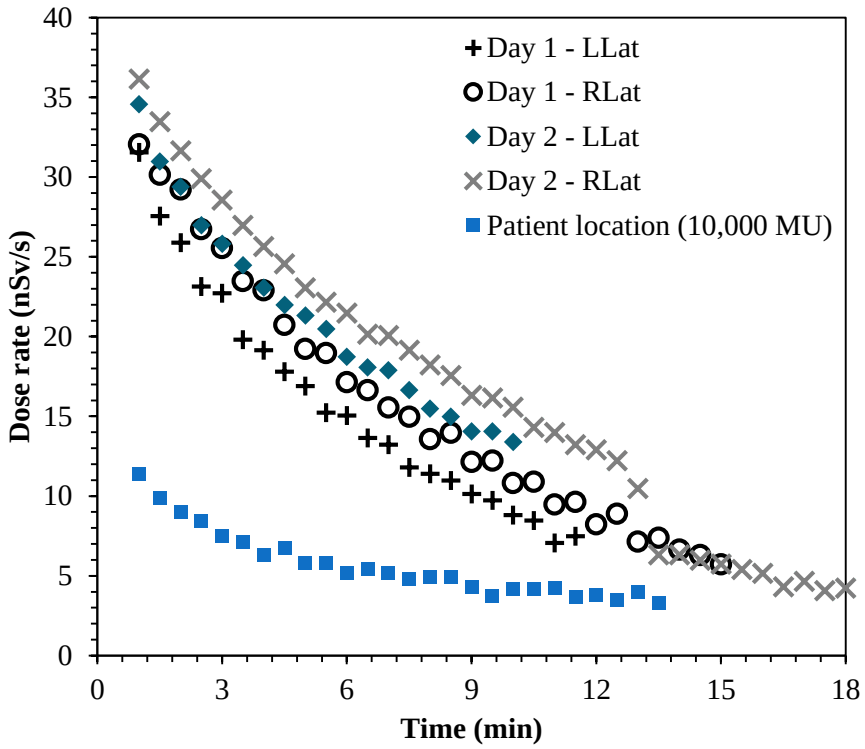

Figure 55: The dose rate measured at the beam exit window following TBI beams delivered to a patient. The left lateral beams were delivered first, followed by the right lateral. During day 1 a beam interlock occurred resulting in premature termination of the beam. The fault was documented and the beam restarted within a couple of minutes. Also shown is the dose rate measured at the patient location, 4.8 m from the linac face.

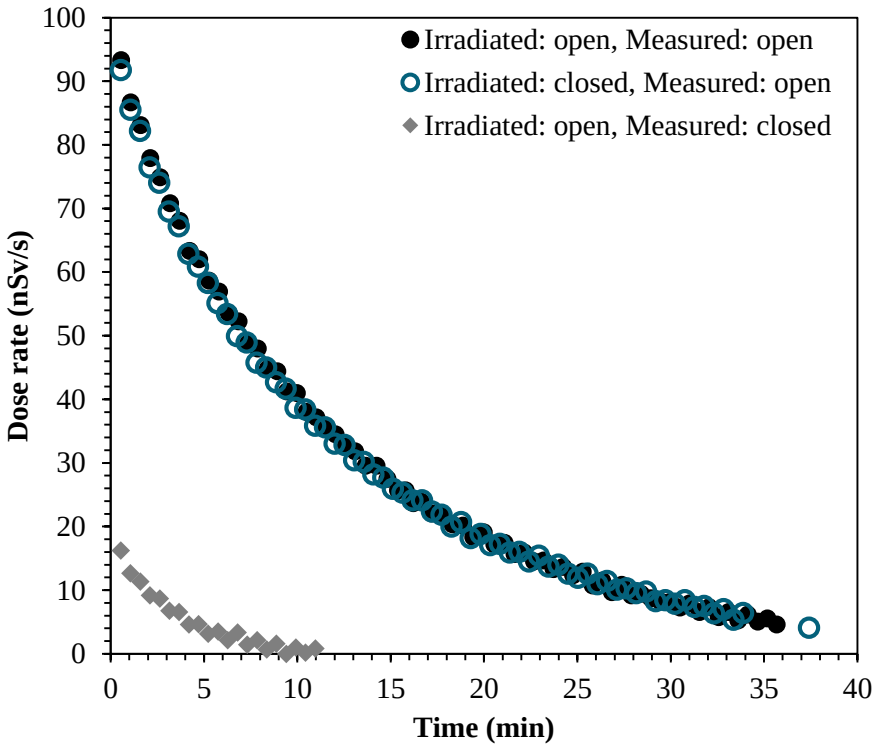

Figure 56: The dose rates measured at the beam exit window of a Varian 21EX after 10,000 MU at 18 MV. Beams were delivered with the jaws and MLC fully retracted to form a 40 × 40 cm^2 field designated "open" and with the jaws fully closed to form a 0.5 × 0.5 cm^2 field designated "closed". The dose rates were also measured in these two configurations.

To investigate a possible correlation between the amount of induced activity and the degree of beam collimation, 10,000 MU were delivered in photon mode with the jaws open and closed. As evident in Figure 56, there was no difference observed between the induced radioactivity for small or large field sizes. However, the dose rate is significantly reduced by the extra shielding provided by the jaws if they are closed after beam delivery ('♦' in Figure 56). The dose rate integrated over ten minutes directly below the closed jaws is a factor of 12 lower than that measured with the jaws opened. Closing the jaws before entering the treatment room to reduce the dose from activation products within the linac is justifiable by this reduction, in keeping with the ALARA principle. It is already common practice at some hospitals to do this after a high energy treatment.

For a staff member spending 10 minutes at the patient location following a TBI delivery involving six fractions of four beams of 2197 MU the annual dose estimate is 750 μSv for an annual patient load of 24. The dose received by staff as a result of induced radioactivity has the potential to make a small contribution to the 20 mSv annual dose limit for occupational exposure. If the jaws are closed before the staff member enters the room, the dose rate over 10 minutes is reduced by a factor of 12, and results in a reduced annual dose to staff members of 65 μSv. This assumes that the same staff member would receive this small dose each time a TBI is delivered and does not account for rostering and rotation of staff throughout the year.

6.2 Activation of hip prostheses in patients

Patient implants, pacemakers, or prostheses composed of non-biological materials may invite significantly different interactions with incident photon and neutron radiation. Heavy nuclei typically have much larger neutron interaction cross sections than the light isotopes predominantly found in tissue. Modern radiotherapy typically involves highly conformal photon beams directed toward a target volume. Contaminant neutrons may be scattered by collimators, but not efficiently absorbed by them. Compared to the photon field, neutrons do not exist as a collimated beam, but as a comparatively diffuse fluence incident on the entire patient (McCall *et al* 1979).

The National Joint Replacement Registry of the Australian Orthopaedic Association (AOA 2016) reported 44,710 hip replacements in the 2015 calendar year. The number of hip replacements has increased each year since complete national data collection was commenced in 2003 with a 64.9 % increase to 31 December 2015. In 2003 the AAPM task group 63 (Reft *et al* 2003) conducted a survey of 30 institutions which showed that 1 – 4 % of patients has prosthetic devices which could affect their therapy.

One of the challenges for pelvic radiotherapy of patients with hip prostheses arises from the artefacts which occur during the planning CT. The high density prosthesis material causes higher attenuation meaning fewer photons reach the detector, which results in an overall lower quality image. The interfaces between a prosthesis and regular tissue type produce bright streaking artefacts in the image (Coolens and Childs 2003). This can lead to inappropriate assignment of CT number to certain regions, which will in turn affect the dose calculation (Roberts 2001). It also becomes difficult to ascertain the boundaries of the prosthesis and of surrounding anatomical structures. Figure 57 shows a CT image of a prostate cancer patient with bilateral hip prostheses. The dark patches labelled "artifacts" are caused by the highly attenuating prosthesis material. Modern CT scanners with artefact reducing algorithms are able to produce better quality images.

It is common practice to avoid directly irradiating metallic prostheses in treatment planning as they are known to perturb the radiation field and reduce the dose to the tissue downstream of the prosthesis (Reft *et al* 2003). Moreover, treatment planning systems do not accurately account for beams traversing

metallic implants and estimate the reduction in dose poorly (Keall *et al* 2003). However, beams are commonly allowed to pass nearby or even through prostheses on exit from the patient.

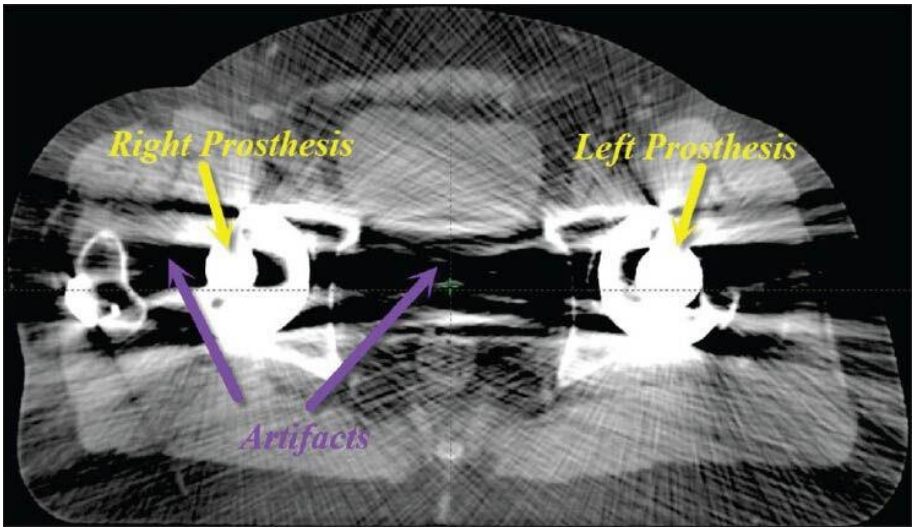

Figure 57: A transversal view of computed tomography slice of prostate cancer patient showing bilateral metallic hip prostheses and artifacts taken from (Rana and Pokharel 2014).

Prostheses may be activated by photons and/or neutrons in high energy radiotherapy. High energy photons can activate prostheses *via* the photonuclear effect, causing the emission of neutrons from within the patient. Neutrons produced in the linac can also be incident on and activate the prostheses, even when planned treatment beams are not directly incident upon them, due to the diffuse nature of the neutron contamination arising from the high frequency of neutron scattering events. These neutrons have mean energies in the vicinity of 0.14 MeV in tissue (Kry *et al* 2009a) and, as such, have high cross sections for capture with the nuclei of hip prostheses. Neutron capture often induces radioactivity in the target nuclei.

In addition to the direct interaction of neutrons with patient tissue, neutrons pose another potential exposure pathway to patients via the production of unstable product nuclei following neutron capture. These radioactive nuclei may emit secondary radiations with half-lives that may be much longer than the beam irradiation times. This can be extended to the neutron activation of metal objects inside the patient. The decay of activation products may involve radiation emissions that will deposit energy in nearby tissue.

6.2.1 Methods

6.2.1.1 Irradiation geometries

Prosthetic hips (Thackray, UK) were irradiated in and out-of-field by 18 MV photon beams in a water phantom in different geometries. The four representative irradiation geometries of interest are shown in Figure 58. The beam entering through the prosthesis (Figure 58 (a)) should ideally be avoided clinically because the prosthesis directly shadows the target. However, this geometry is sometimes necessary to avoid adjacent organs at risk. It is also of interest as it provides a “worst-case” scenario for activation. The other three geometries are more commonly encountered clinically. The beam exiting through the prosthesis, Figure 58 (c), is identical to the “entry” beam (a) except the beam has been significantly attenuated before entering the prosthesis. Beams (b) and (d) pass laterally to the prosthesis, which is exposed only to out-of-field photons and neutrons scattered from the linac head. The water phantom configurations used to simulate these geometries are shown in Figure 59 (a-d). Each water phantom was

placed on at least 3 cm of solid water backscatter material. Each irradiation was 200 MU delivered by a Varian 21 EX at a dose rate of 400 MU/min in 18 MV ($TPR_{20,10}$ = 0.784) photon mode.

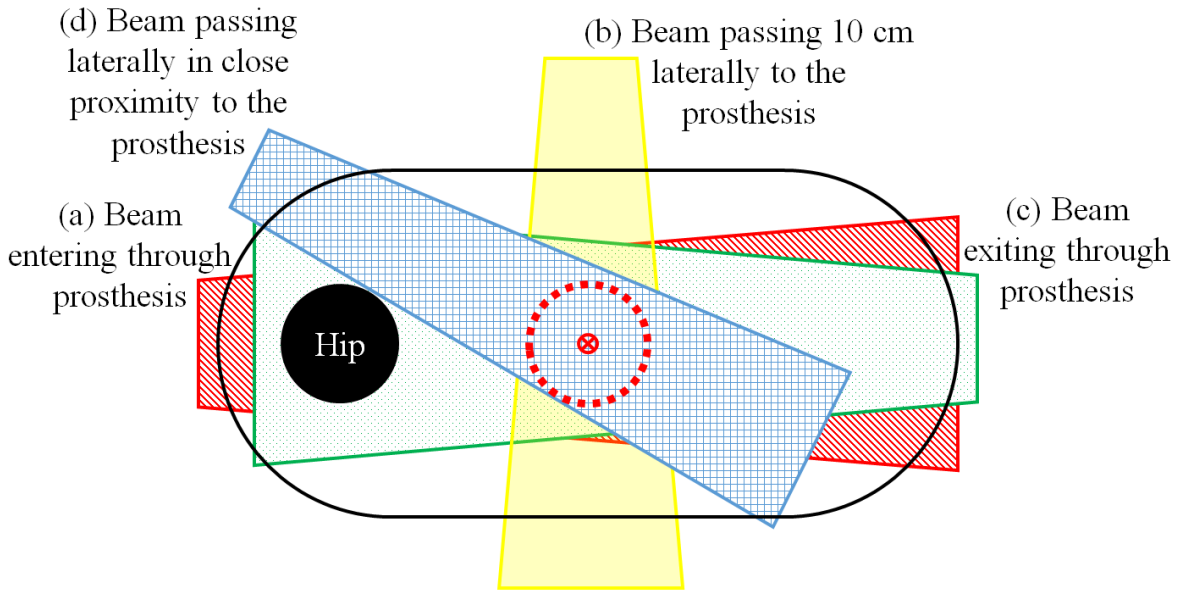

Figure 58: Simulated patient irradiation geometries. Beam (a) enters through the prosthesis, (b) passes laterally 10 cm away. Beam (c) exits through the prosthesis with a larger degree of photon attenuation and neutron moderation than beam (a). Beam (d) also passes laterally in close proximity (within 1 cm) to the prosthesis. The labels (a), (b), (c) and (d) correspond to the geometries shown in Figure 59.

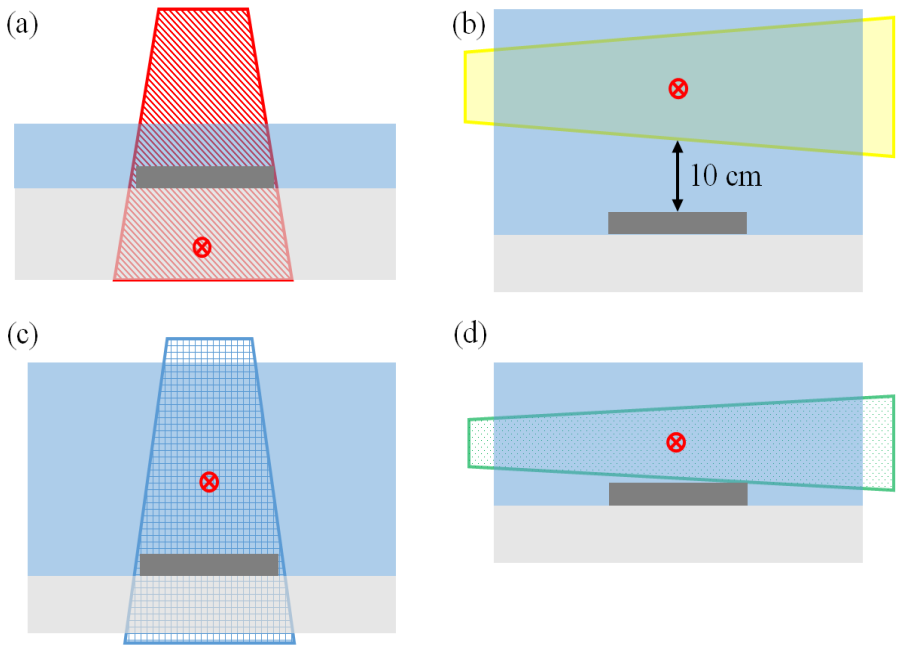

Figure 59: Prosthetic hips were irradiated in a water tank by (a) a beam entering through the prosthesis, (b) a beam passing 10 cm laterally to the prosthesis, (c) a beam exiting through the prosthesis and (d) a beam passing laterally in close proximity to the prosthesis. The red circle represents the isocentre of the beam. Each water phantom was placed on at least 3 cm of solid water backscatter material. The labels (a), (b), (c) and (d) correspond to the geometries shown in Figure 58.

6.2.1.2 Isotopic identification with gamma spectroscopy

The gamma ray energy spectra were acquired within one minute of termination of the beam with a 3 × 3" NaI(Tl) scintillation detector (Saint-Gobain, France) and an Ortec DigiBASE-E Ethernet multichannel analyser PMT base (Ametek, USA). The spectra were each acquired for 15 minutes to allow sufficient counts for peak identification.

6.2.1.3 Dosimetry

To induce sufficient activity to produce a measurable dose, one prosthesis was irradiated at isocentre in water by 10,000 MU from an Elekta Synergy at a dose rate of 450 MU/min at 18 MV ($TPR_{20,10}$ = 0.780). High sensitivity LiF:Mg,Cu,P thermoluminescence dosimeters (TLD-100H) (Harshaw, USA) were used to measure the dose resulting from radioactive isotopes produced in the prosthesis. 24 TLD chips (0.89 × 3.1 × 3.1 mm^3) were placed on the surface of the hip within two minutes of termination of the beam (see Figure 60) and removed after 12 hours (5 half-lives of the longest lived isotope). The responses of the TLDs were measured with a Harshaw 5500 automated reader. Each TLD was corrected for its individual sensitivity relative to the batch average as determined in a 6 MV beam (Faulkner *et al* 1999).

The average signal of 16 un-irradiated TLDs was subtracted from the signal of TLDs placed on the hip to remove background signal unrelated to the irradiation. This is important for reducing uncertainty when using high sensitivity TLDs to measure very low doses (Shoushan *et al* 1986). The backgound dose was minimised by annealing the TLDs immediately before the measurements were performed and the read-out was within 24 hours of the measurements. A total of 50 TLD chips were read out with a Harshaw 5500 automatic reader, which takes approximately 1 hour. Half of the un-irradiated background TLDs were read at the beginning and the other half at the end to allow for variations over the duration of the read-out session. Standards irradiated to 5, 10, 20 and 50 cGy at 6 MV were also read during the session for calibration of the dosimeters affixed to the prosthesis.

Figure 60: The left figure shows a 3 × 3 mm TLD-100H chip. It is affixed to a small square of graph paper by plastic cling wrap which is held in place by double sided tape at the edges of the square. The right figure shows the graph paper squares with attached TLDs affixed to the hip prosthesis following irradiation.

6.2.2 Results

6.2.2.1 Isotopic identification with gamma spectroscopy

The gamma-ray spectra acquired following irradiation show the characteristic gamma-ray peaks of ^{53}Fe, ^{56}Mn and ^{52}V (Figure 61). The total count rates measured during spectroscopy of in-field irradiated prostheses were between 6 and 7.5 times higher than those measured from out-of-field irradiated prostheses. The prostheses irradiated in the lateral out-of-field region are notable for the absence of the ^{53}Fe gamma-ray peaks. The half-lives and gamma-ray energies of these isotopes are given in Table 20.

Radioactive ^{53}Fe with a half-life of 8.51 minutes was observed only in prostheses directly irradiated by 18 MV photon beams. Production of ^{53}Fe is thus attributed to photonuclear interactions with stable ^{54}Fe

and involves neutron production from within the prosthesis itself. This neutron production from within the patient may pose a further risk because of the high relative biological effectiveness (RBE) of neutron radiation.

^{56}Mn and ^{52}V with half-lives of 155 and 3.74 minutes respectively were observed for prostheses irradiated in-field as well as those placed just outside the field and 10 cm from the field. The production of these isotopes is attributed to activation by contaminant neutrons which do not exhibit the same penumbral drop in fluence as photons.

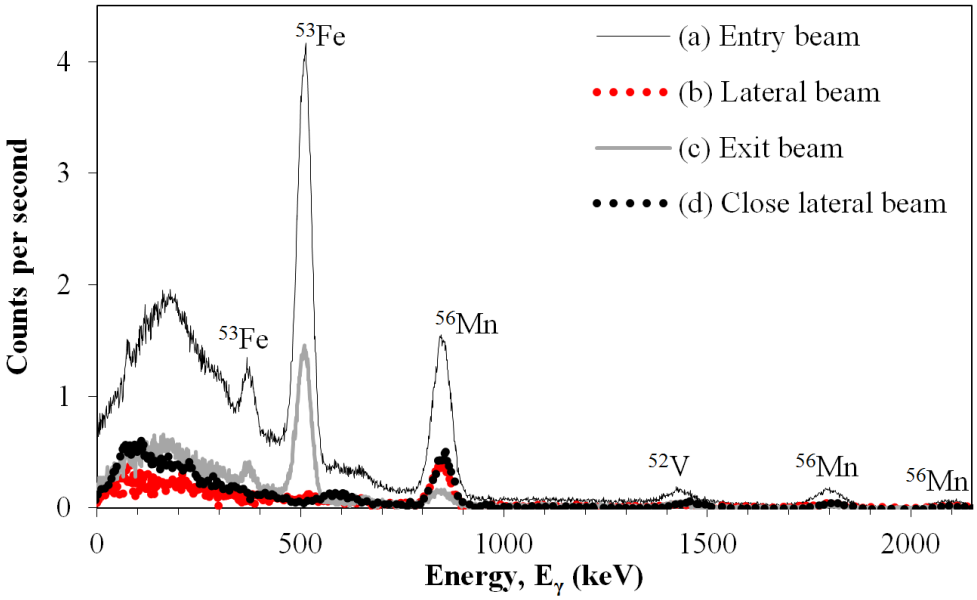

Figure 61: Gamma-ray energy spectra acquired over 15 minutes within one minute of irradiation, for each of the irradiation schemes illustrated in Figure 58 and Figure 59. The peaks shown are consistent with the isotopes given in Table 20.

Table 20: The gamma-ray energies and half-lives of the isotopes produced within the hip prostheses.

E_γ (keV)	Half-life (min)	Isotope	Reaction
378, 511	8.51	^{53}Fe	(γ,n)
847, 1811, 2113	155	^{56}Mn	(n,γ)
1434	3.74	^{52}V	(n,γ)

6.2.2.2 Dosimetry

The average dose measured over the 12 hours immediately following direct irradiation of 10,000 MU was 0.20 mGy at an effective distance of 1 mm (LiF density 2.2 g/cm^3, thickness of the chip 0.89 mm) from the surface with a standard deviation of 0.04 mGy. The limit of detection calculated from the mean and standard deviation of the readings of the un-irradiated background TLDs was 0.05 mGy (with a 99% confidence interval). The highest dose was recorded by the TLDs attached to the thickest part of the prosthesis reflecting the proximity of greater mass of activated material (see Figure 62).

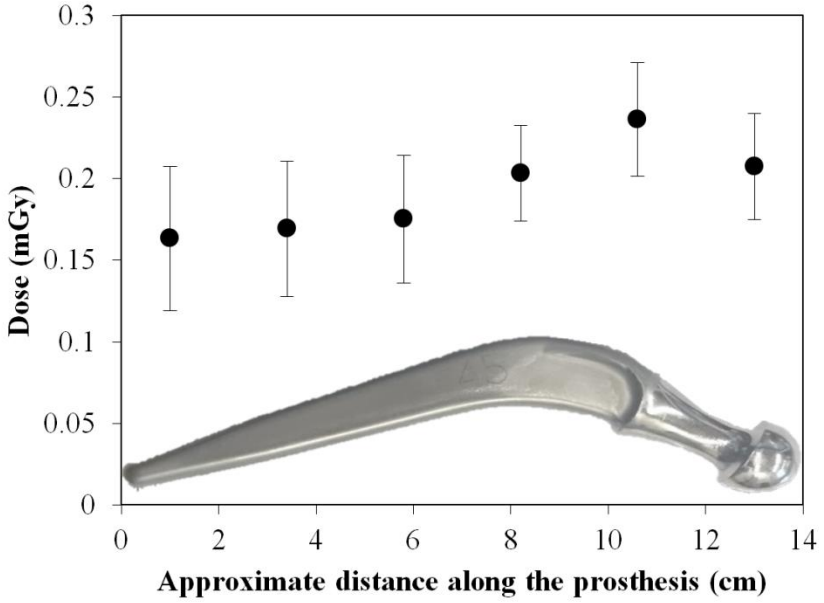

Figure 62: The dose measured on the surface of the prosthesis as a function of the approximate distance from the narrow end to the thicker end which is inserted into the socket. The error bars are the standard deviations of three to four TLD measurements taken at approximately the same distance. Inset: Photo of the hip prosthesis.

The photon dose measured from two minutes post irradiation for a twelve hour duration was 0.20 ± 0.04 mGy for a 10,000 MU irradiation. Twelve hours is approximately five times the longest half-life identified and more than 96% of the radionuclei produced will decay during this time. The dose is slightly higher at the surface of the hip in the thicker regions which is due to the larger mass present. This dose is minute compared to the treatment dose and even the out-of-field doses resulting from scatter and leakage x-rays.

The dose rate induced in prostheses following a typical 2 Gy treatment fraction is of greater clinical relevance. The surface dose over 12 hours was below the minimum detectable limit of 0.05 mGy following the 200 MU exposures performed to measure the gamma spectra of the activated prostheses. The activity induced in a material is not linearly related to the number of monitor units delivered because some nuclei decay during the beam delivery. The overall activity induced is dependent on both the number of MU and the dose rate. The activity of those prostheses irradiated in-field was much higher than those irradiated out of the primary photon field. The surface dose rate of a prosthesis irradiated out-of-field would be expected to be reduced by a similar factor, and it would be below the limit of detection of 0.05 mGy.

6.3 Summary of the relevance to indirect risk from neutron contamination

This chapter lays the foundation for addressing the risk from secondary radiation resulting from photonuclear events and neutron activations. Identifying the isotopes produced in both medical linear accelerators and activated prosthesis within patients allows the half-lives of the radioisotopes to be identified. The half-lives of the isotopes determines the length of time which is relevant for exposures to staff and patients, which in turn relates to the degree of risk. The amount of radioactivity also must be factored in to fully assess the degree of risk. The multiple isotopes activated by neutron interactions provide different contributions to the net dose. Each isotope is produced in a different quantity and has a different half-life, which makes the analysis of the risk non-trivial. The approach here, of measuring the dose rate as a function of time informs risk management strategies, such as the use of shielding or waiting times.

By measuring the dose at the linac face and at a representative location within the treatment bunker following 18 MV beam deliveries, the resulting risk to radiotherapy staff who may frequently be exposed to an activated linac can be determined. The dose at the surface of a prosthetic hip irradiated by an 18 MV is used to quantify the degree of risk which a patient is exposed to resulting from the neutron interactions which may occur during an 18 MV radiotherapy treatment.

7. Discussion

This chapter provides an in-depth discussion of the results of direct neutron measurements and secondary activations presented in the previous chapters. An assessment of the validity of direct neutron measurements is conducted using a comprehensive summary of published neutron dose equivalent values compiled for this study. The results of the neutron phantom measurements are discussed in the context of the risk posed to the patient. Activation of the components of linear accelerators and of implanted devices within patients is also discussed, with a view to assessing the risk posed to staff and patients. The degree of activation observed in linacs is low level, but could be of concern for staff who may spend a significant period of time in close proximity to the machines. Radioisotopes produced in hip prostheses exposed to high energy radiotherapy beams have been identified and presented in chapter 6 and will be discussed in this chapter in terms of the resultant risk to patients.

7.1 Comparison of direct neutron measurement results to literature values

An in-depth literature review was conducted to assess the validity of the direct neutron measurements made in this study. Journal publications which reported a neutron dose equivalent measured or calculated under irradiation conditions similar to those used in this study were included. The reported neutron dose equivalents are shown in Figure 63. References and detailed information about the parameters of each measurement or calculation are given in Table 21.

Nearly all studies which report the results of physical measurements used Bonner spheres or anthropomorphic phantoms. The studies which used Bonner spheres or similar were aiming to measure the neutron energy spectrum and have also inferred the net neutron fluence from the spectrum unfolding data. The studies which used anthropomorphic phantoms have predominantly reported neutron fluence or dose information for organ locations in specific phantom models. The depth of measurement points from the surface and distance from the irradiating field is not always disclosed explicitly.

The measurement configurations used in this study were intended to provide a systematic assessment of the changes with depth and distance from the irradiating field. Although the irradiation conditions and points of measurement differ between studies, this collection of data is useful to assess the order of magnitude of neutron dose equivalent. The two data points from this study which are included in Figure 63 are the maximum results for each detector from the depth-dose curve presented in Figure 48.

The data has been separated according to some key parameters in Figure 64, Figure 65, Figure 66, and Figure 67. Data was included in these figures for all studies where the parameter of interest was specified in the publication. A spread of values is anticipated because the other variables are not held fixed in each plot. The average neutron dose equivalent at some key distances from beam isocentre are shown in Figure 64. Figure 65 shows the average dose measured with different field sizes. The reported doses are separated by the measurement or calculation method in Figure 66 and Figure 67 shows the average results determined for different manufacturers' linacs for given nominal beam energies. Each data point is labelled with the number of reported values used to calculate the average.

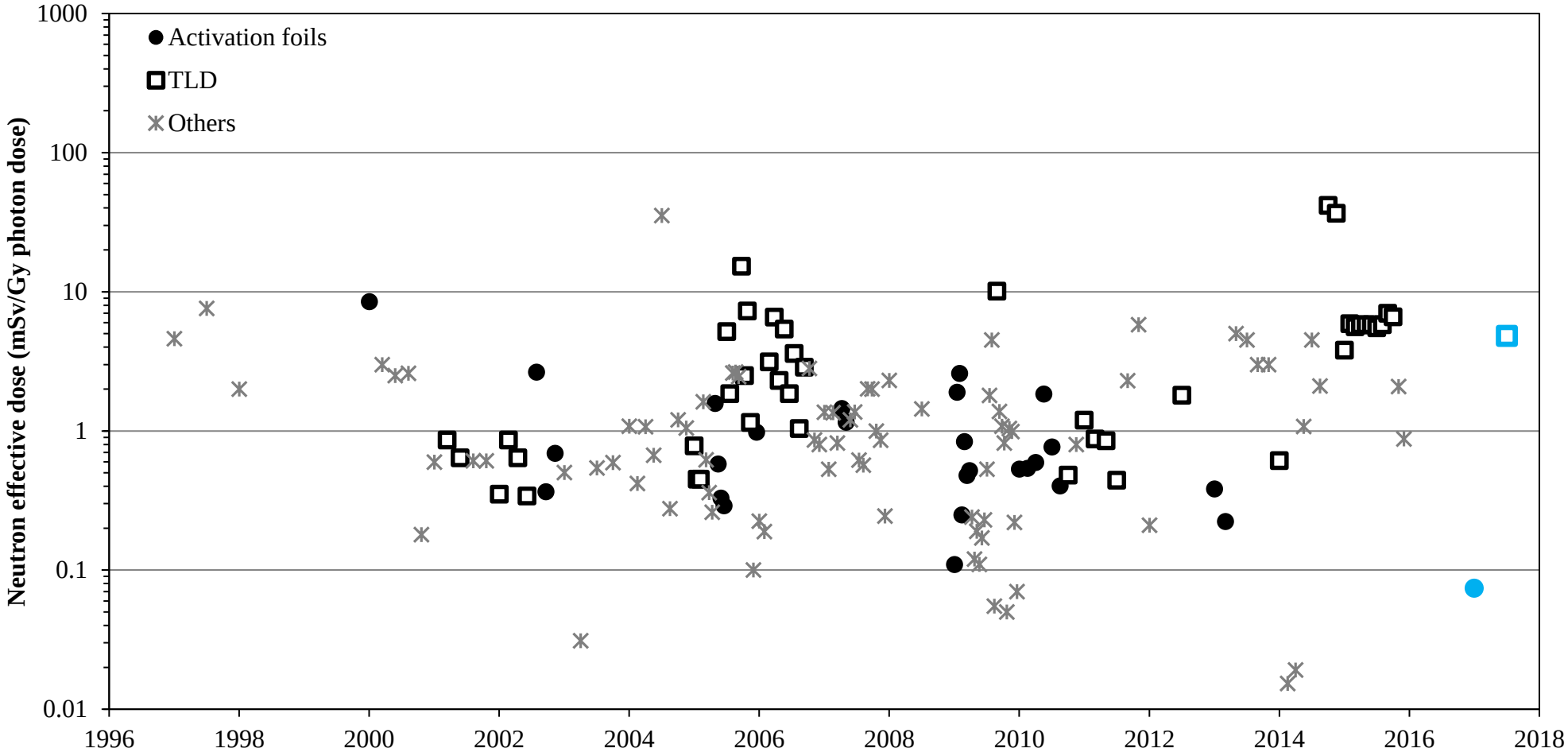

Figure 63: Neutron dose equivalent in mSv/Gy photon dose as reported in literature. The coloured points are those measured in this study. Note the vertical axis is logarithmic. The plot incorporates 152 data points taken from 58 references; see Table 21 for details and references. Results from publications are grouped together and ordered the year of publication.

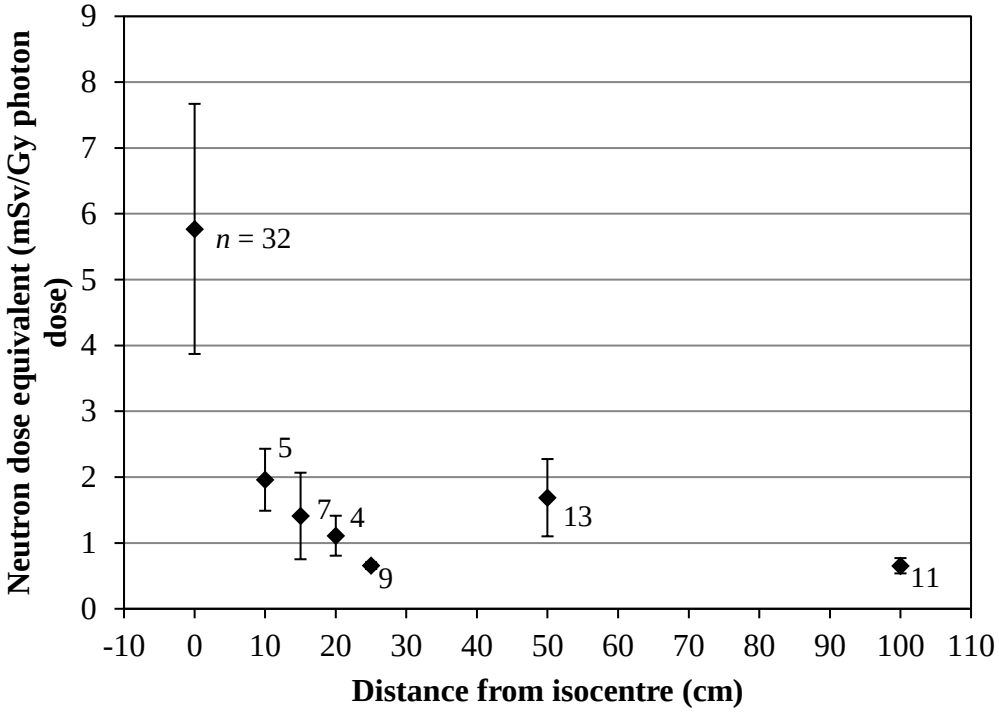

Figure 64: The mean neutron dose equivalent in mSv/Gy photon dose as reported in literature at different distances from isocentre. The error bars represent the standard uncertainty of the mean. Each data point is labelled with the number of values used to calculate the mean.

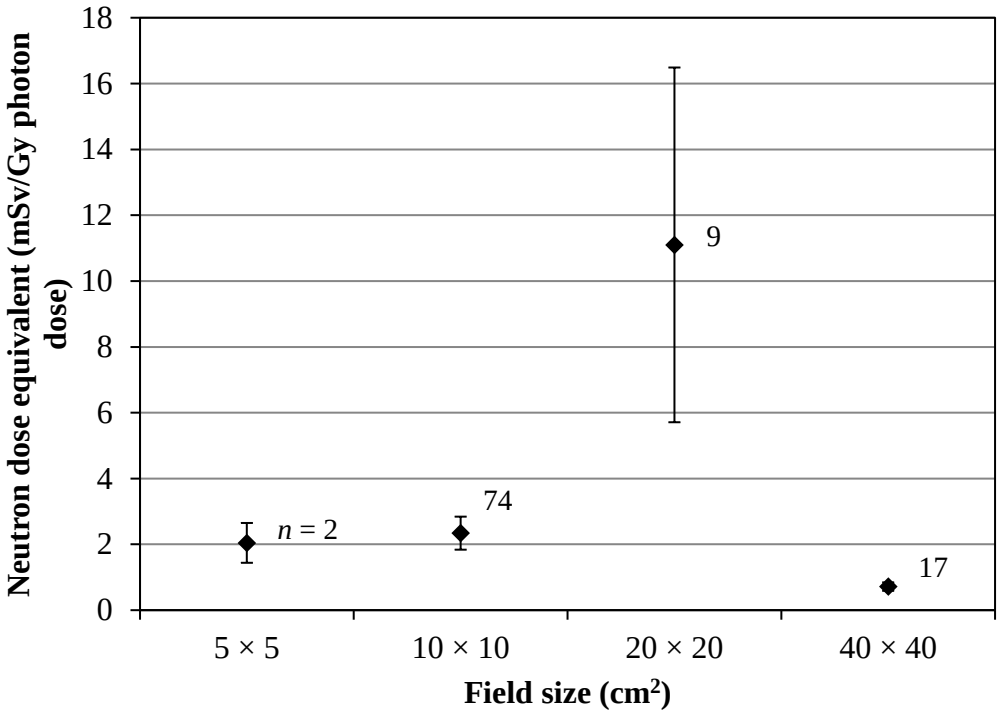

Figure 65: The mean neutron dose equivalent in mSv/Gy photon dose as reported in literature for different treatment field sizes. The error bars represent the standard uncertainty of the mean. Each data point is labelled with the number of values used to calculate the mean.

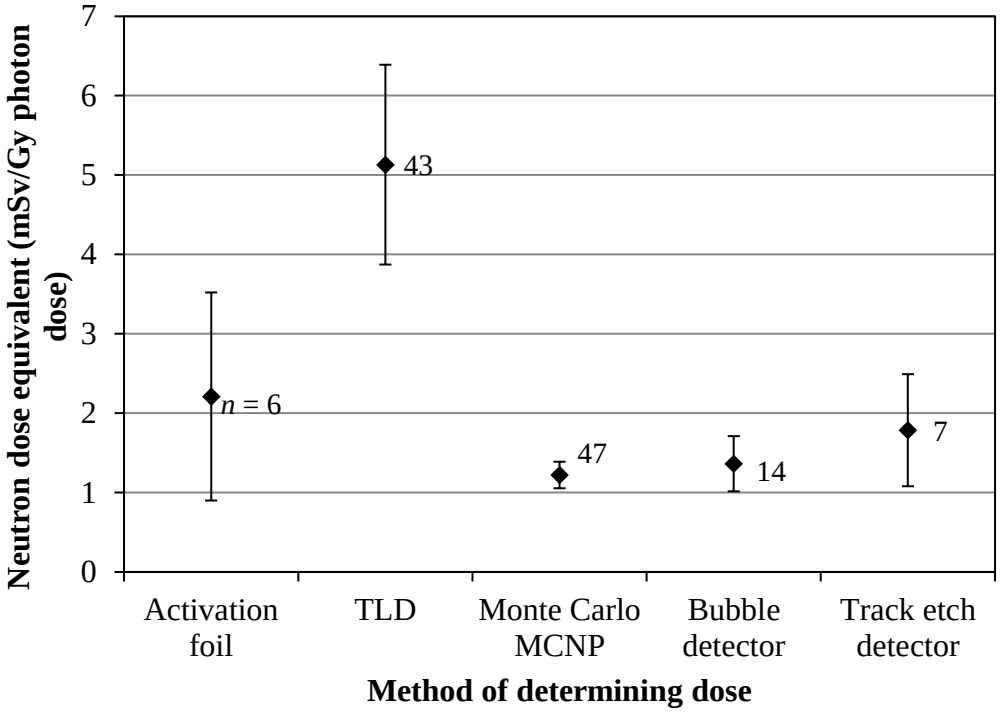

Figure 66: The mean neutron dose equivalent in mSv/Gy photon dose as reported in literature determined from different measurement and calculation techniques. The error bars represent the standard uncertainty of the mean. Each data point is labelled with the number of values used to calculate the mean. The detectors were positioned at various locations, the distance from isocentre for each study is given in Table 21.

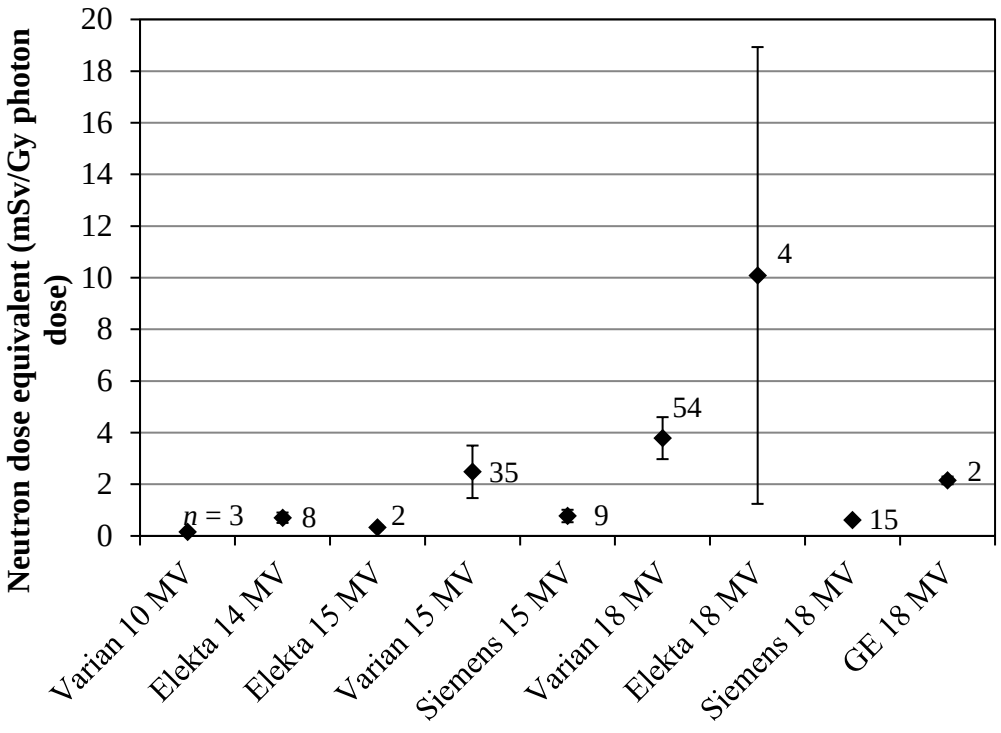

Figure 67: The mean neutron dose equivalent in mSv/Gy photon dose as reported in literature for different linac manufacturers and accelerating potentials. The error bars represent the standard uncertainty of the mean. Each data point is labelled with the number of values used to calculate the mean. The measurements were conducted at various locations, the distance from isocentre used in each study is given in Table 21.

The data compiled from literature and shown in Figure 63 varies over more orders of magnitude than that observed with the systematic changes with depth and distance measured in this study (Figure 48, Figure 49). The wide spread of values plotted in Figure 63 is not unexpected given that the measurements are taken under different conditions, however since the overall variation is greater than the systematic changes observed in the data collected for this study, this may reflect the degree of the inherent challenges in neutron dosimetry. The data shown in Figure 63 has been reported for a variety of irradiation conditions; however, all measurement or calculation points were specified within the patient plane. The irradiations vary amongst machine manufacturer, accelerating potential and field size. The results are also compiled for a number of different measurement techniques and for values calculated using Monte Carlo simulation codes.

It is of interest from a radiation protection point of view to note the upper bound on the neutron dose equivalent values. It is common practise in risk assessment to take a conservative approach to determining estimates so that a worst case scenario can be considered. The upper bound from the data collated in Figure 63 is approximately 35 to 40 mSv/Gy.

The mean of values reported at the same distance from isocentre are calculated and shown in Figure 64. Apart from an outlying value at a distance of 50 cm, which has a large standard deviation, the neutron dose reduces with distance from the isocentre in the near out-of-field region, up to 25 cm from isocentre. At greater distances there is less data available at different distances, so the compilation of results is coarse in resolution. It is expected that the far out-of-field regions would have a relatively constant neutron fluence and spectrum of low energy scattered neutrons (McCall *et al* 1999).

Neutron dose equivalent results obtained from irradiation by different photon field sizes are shown in Figure 65. The standard deviation of the mean of doses measured with an irradiation field size of 20 × 20 cm^2 is quite large and makes it difficult to determine an overall trend between dose and field size. The work of Sohrabi *et al* (2016) showed that for out-of-field neutron measurements, field size did not correlate with neutron dose equivalent. In-field measurements did show an increase in neutron dose equivalent with increasing field size. This implies that both primary (direct) and scattered neutrons contribute to the neutron fluence in-field and the greater the amount of lead and tungsten collimators intersecting the beam, the more neutron fluence is scattered *away* from the primary field. For neutrons outside the primary field, the fluence is primarily scattered neutrons and is not significantly affected by the field size of the primary field.

The measurement or calculation technique chosen may introduce a systematic bias in the result. Figure 66 shows the average of all results measured with the same detector type and those calculated with Monte Carlo code MCNP. The neutron dose equivalents reported from measurements made with TLDs appear to be significantly higher than those results obtained through the use of other detectors and through modelling. This may be due to the energy dependence of TLD response and the effect of using a calibration source with a different energy spectrum to that produced by a medical linear accelerator. Many of the publications included did not mention an energy correction, and of those that did the magnitude of the correction was not explicitly reported.

The energy correction used for TLD calibration in this work assumes no scattering (or moderation) of the AmBe source. A very large room was chosen specifically to reduce the effect of scattered neutrons. A larger surface area corresponds to fewer scattered neutrons relative to direct neutrons (McCall *et al* 1999). It is an assumption of this work that the surface area of the calibration room was sufficiently large that the scattered component is negligible. If this assumption is incorrect, the overall effect is that the value of *k* used to correct the TLD response in the calibration is too high. This would result in the calibration factor determined being an *under*estimate of the true calibration factor, and the measured neutron fluences presented in chapter 5 were an *under*estimate of the true neutron fluence. This seems

unlikely, as the TLD results of this thesis (and of many other works, see Figure 66) tend to be *higher* than the results achieved through other methods.

Of the published studies included in this review, only two used more than one type of detector to perform the measurements under the same conditions. Di Fulvio *et al* (2013) used track etch detectors and bubble detectors with good agreement with results of 4.5 and 5 mSv/Gy at isocentre. Ipe *et al* (2000) used a combination of activation foils, track etch detectors, and bubble detectors with neutron dose equivalent results varying from 2.5 to 8.5 mSv/Gy photon dose. The overall discrepancy between detector types observed in Figure 66 is invisible to an individual using only one type of detector.

Different linac designs could be expected to influence the level of neutron contamination. The cross section for neutron production is material dependent and energy dependent. The photon energy spectrum produced by a linac will also have an effect. The results reported for measurements made from different linac manufacturers and nominal beam energies are shown in Figure 67. There is a high degree of uncertainty in the mean dose equivalent for neutrons produced by Elekta linacs operating at 18 MV, because there are relatively few studies reporting on this. There is much more data available for linacs manufactured by Varian, where a clear increase in neutron dose equivalent with increasing beam energy can be observed. This is expected as the cross section for neutron production in the materials most commonly present in linacs peaks around 12 – 15 MeV (see Figure 1, §2.2).

The wide spread of reported values for neutron dose equivalent under similar irradiation conditions highlights the difficulty of accurate neutron dosimetry. The overly simplistic treatment of energy spectrum effects on both calibration exposures and linac measurements is probably the largest source of error in published works to date. Calibration of detectors or dosimeters with neutron sources of higher energy than the linac neutrons, without correctly accounting for the energy dependence can result in overestimation of the neutron fluence or dose. Many papers do not fully describe the procedure or calculation used to convert neutron fluence to equivalent or effective dose, which may make comparison between studies invalid.

The results presented in this thesis also have considerable associated uncertainty. The calibration factor determined for the ^{6}LiF and ^{7}LiF TLD pairs has a high uncertainty because the low signal produced by the TLDs is inherently noisy and the neutron source activity has an uncertainty of 5 %. The main source of uncertainty in the activation foil measurements comes from the high uncertainty in the neutron energy spectrum used to calculate the activation foil cross section.

Table 21: Reported neutron dose equivalent dose per Gy of photon dose for a variety of positions, linac manufacturers and field sizes.

Reference	**Neutron dose equivalent (mSv/Gy)**	**Distance from isocentre (cm)**	**Linac manufacturer and beam energy**	**Field size (cm^2)**	**Detector or Monte Carlo code used**	**Comments**
This work	0.07	15	Varian 18 MV	10 × 10	Activation foil - indium	
	4.83	15	Varian 18 MV	10 × 10	TLD	
Barquero *et al* (2002)	0.35	30	Siemens 18 MV	40 × 40	TLD	
	0.86	25	Siemens 18 MV	40 × 40	TLD	
	0.64	25	Siemens 18 MV	40 × 40	TLD	
	0.34	80	Siemens 18 MV	40 × 40	TLD	
Barquero *et al* (2005)	0.78	25	Siemens 18 MV	40 × 40	TLD	
	0.45	25	Siemens 18 MV	40 × 40	TLD	
	0.45	25	Siemens 18 MV	40 × 40	TLD	
Bedogni *et al* (2013)	0.383	150	Varian 15 MV	10 × 10	Activation foils	
	0.224	200	Varian 15 MV	10 × 10	Activation foils	
Benites-Rengifo *et al* (2014)	0.612	100	Varian 15 MV	20 × 20	TLD	Median spectrum energy values
Bezak *et al* (2015)	3.8	Thyroid	Varian 18 MV	10 × 10	TLD	4 field prostate treatment
	5.9	Lung	Varian 18 MV	10 × 10	TLD	4 field prostate treatment
	5.6	Oesophagus	Varian 18 MV	10 × 10	TLD	4 field prostate treatment
	5.8	Liver	Varian 18 MV	10 × 10	TLD	4 field prostate treatment
	5.8	Spleen	Varian 18 MV	10 × 10	TLD	4 field prostate treatment
	5.8	Stomach	Varian 18 MV	10 × 10	TLD	4 field prostate treatment
	5.5	Kidney	Varian 18 MV	10 × 10	TLD	4 field prostate treatment
	5.8	Pancreas	Varian 18 MV	10 × 10	TLD	4 field prostate treatment
	7	Colon	Varian 18 MV	10 × 10	TLD	4 field prostate treatment
	6.6	Small intestine	Varian 18 MV	10 × 10	TLD	4 field prostate treatment
Carinou *et al* (2005)	1.62	0	Elekta 14 MV	10 × 10	Monte Carlo MCNP	
	0.62	20	Elekta 14 MV	10 × 10	Monte Carlo MCNP	
	0.36	50	Elekta 14 MV	10 × 10	Monte Carlo MCNP	
	0.26	90	Elekta 14 MV	10 × 10	Monte Carlo MCNP	
	1.58	0	Elekta 14 MV	10 × 10	Activation foils	
	0.58	20	Elekta 14 MV	10 × 10	Activation foils	
	0.33	50	Elekta 14 MV	10 × 10	Activation foils	
	0.29	90	Elekta 14 MV	10 × 10	Activation foils	

Reference	Neutron dose equivalent (mSv/Gy)	Distance from isocentre (cm)	Linac manufacturer and beam energy	Field size	Detector or Monte Carlo code used	Comments
Chen *et al* (2006)	0.225	100	Varian 10 MV	10 × 10	Bubble detector	
	0.189	100	Varian 10 MV	10 × 10	Monte Carlo FLUKA	
Chibani and Ma (2003)	0.503	0	Siemens 18 MV	10 × 10	Monte Carlo MCNP	
Chu *et al* (2011)	1.195	36	Varian 15 MV	10 × 10	TLD	
	0.874	100	Varian 15 MV	10 × 10	TLD	
	0.847	36	Varian 15 MV	40 × 40	TLD	
	0.441	100	Varian 15 MV	40 × 40	TLD	
d'Errico *et al* (1998)	2	10	GE 18 MV	10 × 10	Bubble detector	
Di Fulvio *et al* (2013)	5	0	GE 20 MV	10 × 10	Track etch detector	
	4.5	0	GE 20 MV	10 × 10	Bubble detector	
	3	10	GE 20 MV	10 × 10	Track etch detector	
	3	10	GE 20 MV	10 × 10	Bubble detector	
Domingo *et al* (2010)	0.532	50	Siemens 15 MV	10 × 10	Activation foils	
	0.539	50	Siemens 15 MV	10 × 10	Activation foils	
	0.595	50	Siemens 18 MV	10 × 10	Activation foils	
	1.846	50	Siemens 23 MV	10 × 10	Activation foils	
	0.769	50	Varian 15 MV	10 × 10	Activation foils	
	0.403	50	Elekta 15 MV	10 × 10	Activation foils	
Facure *et al* (2004)	1.08		GE 25 MV		Monte Carlo MCNP	140 cm from target
	0.42		Siemens 20 MV		Monte Carlo MCNP	140 cm from target
	1.07		Varian 18 MV		Monte Carlo MCNP	100 cm from target
	0.67		Varian 15 MV		Monte Carlo MCNP	100 cm from target
Falcao *et al* (2007)	1.36		GE 25 MV		Monte Carlo MCNP	
	0.53		Siemens 20 MV		Monte Carlo MCNP	
	1.35		Varian 18 MV		Monte Carlo MCNP	
	0.82		Varian 15 MV		Monte Carlo MCNP	
Fernandez *et al* (2007)	1.452	100	Varian 18 MV	10 × 10	Activation foils	Fission, intermediate and thermal
	1.158	100	Varian 18 MV	10 × 10	Activation foils	Giant dipole resonance and thermal
Followill *et al* (1997)	4.6	50	Varian 18 MV		Calculated	
	7.6	50	Varian 25 MV		Calculated	
Ghassoun *et al* (2011)	2.3	0	GE 18 MV	10 × 10	Monte Carlo MCNP	
Golnik *et al* (2004)	35.4	0	Varian 15 MV	10 × 10	Chamber	

Reference	Neutron dose equivalent (mSv/Gy)	Distance from isocentre (cm)	Linac manufacturer and beam energy	Field size	Detector or Monte Carlo code used	Comments
Golnik *et al* (2007)	1.2	50	Varian 15 MV	10 × 10	Chamber	
	1.367	50	Varian 15 MV	10 × 10	Chamber	
	0.617	100	Varian 15 MV	10 × 10	Chamber	
	0.567	100	Varian 15 MV	10 × 10	Chamber	
Hälg *et al* (2014)	0.015	7.46479	Varian 15 MV		Track etch detector	IMRT
	0.019	12.5352	Varian 15 MV		Track etch detector	IMRT
Howell *et al* (2005a)	5.17	21	Varian 18 MV		TLD	IMRT
	1.85	21	Varian 18 MV		TLD	Conventional
	2.61		Varian 18 MV	0 × 0	Monte Carlo MCNP	
	2.65		Varian 18 MV	5 × 5	Monte Carlo MCNP	
	2.46		Varian 18 MV	10 × 10	Monte Carlo MCNP	
Howell *et al* (2005b)	15.26		Varian 18 MV		TLD	IMRT
	2.49		Varian 18 MV		TLD	Conventional
	7.26		Varian 15 MV		TLD	IMRT
	1.15		Varian 15 MV		TLD	Conventional
Howell *et al* (2006)	3.13	0	Varian 18 MV		TLD	Conventional
	6.58	0	Varian 18 MV		TLD	IMRT
	2.3	40	Varian 18 MV		TLD	Conventional
	5.38	40	Varian 18 MV		TLD	IMRT
	1.85	0	Varian 15 MV		TLD	Conventional
	3.59	0	Varian 15 MV		TLD	IMRT
	1.04	40	Varian 15 MV	10 × 10	TLD	Conventional
	2.86	40	Varian 15 MV	10 × 10	TLD	IMRT
Howell *et al* (2009)	0.11	40	Varian 15 MV	10 × 10	Activation foils	
	1.9	40	Varian 18 MV	10 × 10	Activation foils	
	2.6	40	Varian 20 MV	10 × 10	Activation foils	
	0.25	40	Elekta 15 MV	10 × 10	Activation foils	
	0.84	40	Elekta 18 MV	10 × 10	Activation foils	
	0.48	40	Siemens 15 MV	10 × 10	Activation foils	
	0.52	40	Siemens 18 MV	10 × 10	Activation foils	
Hsu *et al* (2010)	0.48	40	15 MV	6 × 11	TLD	
Huang *et al* (2005)	0.1	0	15 MV		Monte Carlo FLUKA	

Reference	Neutron dose equivalent (mSv/Gy)	Distance from isocentre (cm)	Linac manufacturer and beam energy	Field size	Detector or Monte Carlo code used	Comments
Ipe *et al* (2000)	8.5	0	Varian 15 MV	20 × 20	Activation foil	
	3	0	Varian 15 MV	20 × 20	Track etch detector	
	2.5	0	Varian 15 MV	20 × 20	Bubble detector	
Kim and Lee (2007)	2.01	5	Varian 15 MV	10 × 10	Monte Carlo MCNP	
	2	5	Varian 15 MV	10 × 10	Monte Carlo MCNP	
Kralik and Turek (2004)	0.2763	71	Varian 15 MV	20 × 20	^{3}He counter	
Kry *et al* (2005b)	0.98	Colon	Varian 18 MV		Activation foil	Prostate 3D CRT
Kry *et al* (2007b)	1	10	Varian 18 MV	10 × 10	Monte Carlo MCNP	
Kry *et al* (2008)	2.31	40	Varian 18 MV	10 × 10	Monte Carlo MCNP	
Kry *et al* (2009a)	1.8	20	Varian 18 MV	10 × 10	Monte Carlo MCNP	
Kry *et al* (2009b)	0.24	Colon	Varian 18 MV		Monte Carlo MCNP	Prostate IMRT
	0.12	Liver	Varian 18 MV		Monte Carlo MCNP	Prostate IMRT
	0.19	Stomach	Varian 18 MV		Monte Carlo MCNP	Prostate IMRT
	0.11	Oesophagus	Varian 18 MV		Monte Carlo MCNP	Prostate IMRT
	0.17	Lung	Varian 18 MV		Monte Carlo MCNP	Prostate IMRT
	0.23	Thyroid	Varian 18 MV		Monte Carlo MCNP	Prostate IMRT
	0.53	Testes	Varian 18 MV		Monte Carlo MCNP	Prostate IMRT
La Tessa *et al* (2014)	1.079	10.13	Elekta 25 MV		Bubble detector	IMRT
Lin *et al* (2001)	0.598	23.2558	Siemens 15 MV	40 × 40	Bubble detector	
Lin *et al* (2007)	0.856	15	Siemens 15 MV	10 × 10	Bubble detector	
	0.244	15	Siemens 15 MV	10 × 10	Bubble detector	
Maglieri *et al* (2015)	2.083	40	Varian 18 MV		Bubble detector	
Martinez-Ovalle *et al* (2011)	5.8	0	Varian 18 MV		Monte Carlo MCNP	
Mesbahi *et al* (2010)	0.8	10	Elekta 18 MV	10 × 10	Monte Carlo MCNP	
Mohammadi *et al* (2015)	0.875	0	Siemens 15 MV	10 × 10	Monte Carlo MCNP	
Nedaie *et al* (2014)	4.5	0	Varian 18 MV	20 × 20	Monte Carlo MCNP	
	2.1	0	Elekta 18 MV	20 × 20	Monte Carlo MCNP	
	41.8	0	Varian 18 MV	20 × 20	TLD	
Nedaie *et al* (2014)	36.6	0	Elekta 18 MV	20 × 20	TLD	
Ongaro *et al* (2000)	2.6	15	Siemens 15 MV		Monte Carlo MCNP	
Rebello *et al* (2008)	1.44	20	Varian 18 MV	5 × 5	Monte Carlo MCNP	
Reft *et al* (2006)	2.807	27	Cl-2100 18 MV	10 × 10	track etch detector	

Reference	Neutron dose equivalent (mSv/Gy)	Distance from isocentre (cm)	Linac manufacturer and beam energy	Field size	Detector or Monte Carlo code used	Comments
Reft *et al* (2006)	0.863	27	Primus 18 MV	10 × 10	track etch detector	
	0.797	27	SL-C 18 MV	10 × 10	track etch detector	
Roy and Sandison (2000)	0.18		Varian 18 MV	30 × 30	Bubble detector	Dose to foetus from chest irradiation
Saeed *et al* (2009)	4.5	0	Varian 18 MV	10 × 10	Monte Carlo GEANT	
Sánchez-Doblado *et al* (2012)	0.21	15	Varian 15 MV	10 × 10	Digital detector	
Sánchez-Doblado *et al* (2009)	0.055		18 MV		Digital detector	
Sanz *et al* (2001)	0.86	25	Siemens 18 MV	40 × 40	TLD	
	0.64	25	Siemens 18 MV	40 × 40	TLD	
	0.61	25	Siemens 18 MV	40 × 40	Monte Carlo MCNP	
	0.61	25	Siemens 18 MV	40 × 40	Monte Carlo MCNP	
Takam *et al* (2009)	10.09	Colon	Varian 18 MV		TLD	4 field prostate treatment
Takam *et al* (2012)	1.8	50	Varian 18 MV		TLD, track etch detector	In air measurement
Thomas *et al* (2002)	2.652	0	Varian 15 MV	40 × 40	Activation foil	
	0.367	100	Varian 15 MV	40 × 40	Activation foil	
	0.691	100	Varian 15 MV	40 × 40	Activation foil	with 30° hard wedge
Vanhavere *et al* (2004)	1.2		Varian 18 MV	10 × 10	Bubble detector	Total dose to organs
Waller *et al* (2003)	0.031	0	Varian 18 MV	10 × 10	Bubble detector	
	0.541		Varian 18 MV	10 × 10	MCNP	157 cm from the head
	0.593		Varian 18 MV	10 × 10	Bubble detector	157 cm from the head
Zabihzadeh *et al* (2009)	1.38	0	Varian 20 MV		Monte Carlo MCNP	
	1.08	0	Varian 18 MV		Monte Carlo MCNP	
	0.05	0	Varian 10 MV		Monte Carlo MCNP	
	1.04	0	Siemens 20 MV		Monte Carlo MCNP	
	0.99	0	Siemens 18 MV		Monte Carlo MCNP	
	0.22	0	Siemens 15 MV		Monte Carlo MCNP	
	0.07	0	Siemens 10 MV		Monte Carlo MCNP	
Zanini *et al* (2004)	1.05	15	Varian 18 MV	10 × 10	Monte Carlo MCNP	

7.1.1 A note on the "Sins of the Sievert"

The use of *dose equivalent* for comparison between studies is not necessarily a suitable comparison. Relatively recently, in the ICRP103 (2007) report, the radiation weighting factor for neutrons was re-evaluated to reflect a new understanding of the energy dependence of neutron dose deposition behaviour. The relative biological effect of neutrons is energy dependent, and the accepted values have been updated and re-evaluated over time and introduce a degree of uncertainty when comparing historically reported values. There is also data to suggest that the ICRP values are overly conservative and not appropriate for high energy radiations or neutrons (Pelliccioni 1998). Not all published studies used for comparison in this work use the same methodology to convert fluence to dose equivalent, or dose in Gray to dose equivalent in Sieverts. It would indeed be more accurate if studies would report neutron absorbed doses in units of Gray and comparisons could be performed without the added uncertainty of the equivalent or effective dose conversion weighting factors. However, the measurement of neutron dose is exceptionally complicated. Neutron dose to tissue cannot be directly measured; the dose to the detector is radically different and the calibration is dependent on energy spectrum. Even if the dose (in Gray) could be inferred, it would not provide an appropriate metric with which to assess the risk from exposure to a given dose. In order to quantify the risk, the neutron fluence (which *can* be measured) should be converted to a neutron dose equivalent (in Sieverts). However, results reported this way should be unambiguous in reporting the methods and values used to convert to dose equivalent in Sieverts in order to allow comparison with other values into the future.

7.1.2 Risk

The challenges and uncertainties associated with neutron dosimetry are illustrated by Figure 63. The spread of reported values for neutron dose in high energy radiotherapy makes it difficult to accurately evaluate the risks to patients. In estimating a risk, the tendency is to err on the side of conservatism and over-estimate the risk. The widely employed ALARA principle and the Linear No Threshold (LNT) model exemplify this conservatism. The danger of course is that the potential benefits of high energy radiotherapy are lost because of potentially over-conservative risk estimates.

The neutron dose evaluated in this thesis is within the range of 0.1 to 5 % of the delivered photon dose. Taking the lower bound of 0.1 % of the photon dose, the neutron dose is likely low enough to consider implementing longer, more complex treatments such as IMRT, VMAT, SABR and TBI if the dose distribution could be significantly improved by using higher energy beams. However, taking the upper bound of neutron doses up to 5 % of the photon dose, this dose is high enough to warrant some restriction and perhaps complete prohibition of the use of higher energy beams for treatment modalities involving high numbers of MU.

The principles of risk analysis require that the consequence of the risk be a consideration in the evaluation. Since the consequences in this case will directly impact on a cancer patient's projected survival following treatment, a conservative approach is justified when assessing the risk resulting from a neutron dose which cannot be more precisely quantified. In order to make a more informed judgement on the issue of neutron contamination in high energy radiotherapy, more accurate neutron dosimetry is required. The largest reduction in the uncertainty in neutron dosimetry can be made with more detailed and accurate information about the neutron energy spectrum produced by medical linear accelerators. This would be best achieved with detailed Monte Carlo modelling. This could be made possible if the manufacturers of medical linear accelerators released detailed dimensions of the shielding and other components inside medical linear accelerators. The size of the treatment bunker and the composition of the walls, ceiling and flooring also need to be considered in developing an accurate model.

7.2 Indirect risk from secondary activation

The photonuclear effect may cause the emission of neutrons and may also induce secondary radioactivity. The nuclei from which the neutrons are emitted may become unstable from the loss of a neutron and become radioactive. This can affect components in the linac itself as well as other materials inside the treatment room. The isotopes present in human tissue do not have high cross sections for neutron activation or photonuclear interactions; however implanted devices may have an increased likelihood of becoming activated. The photonuclear effect poses a risk to staff and patients from activation of the linac and activation of patient implants. A flow chart describing the interactions and locations of secondary activation is shown in Figure 68.

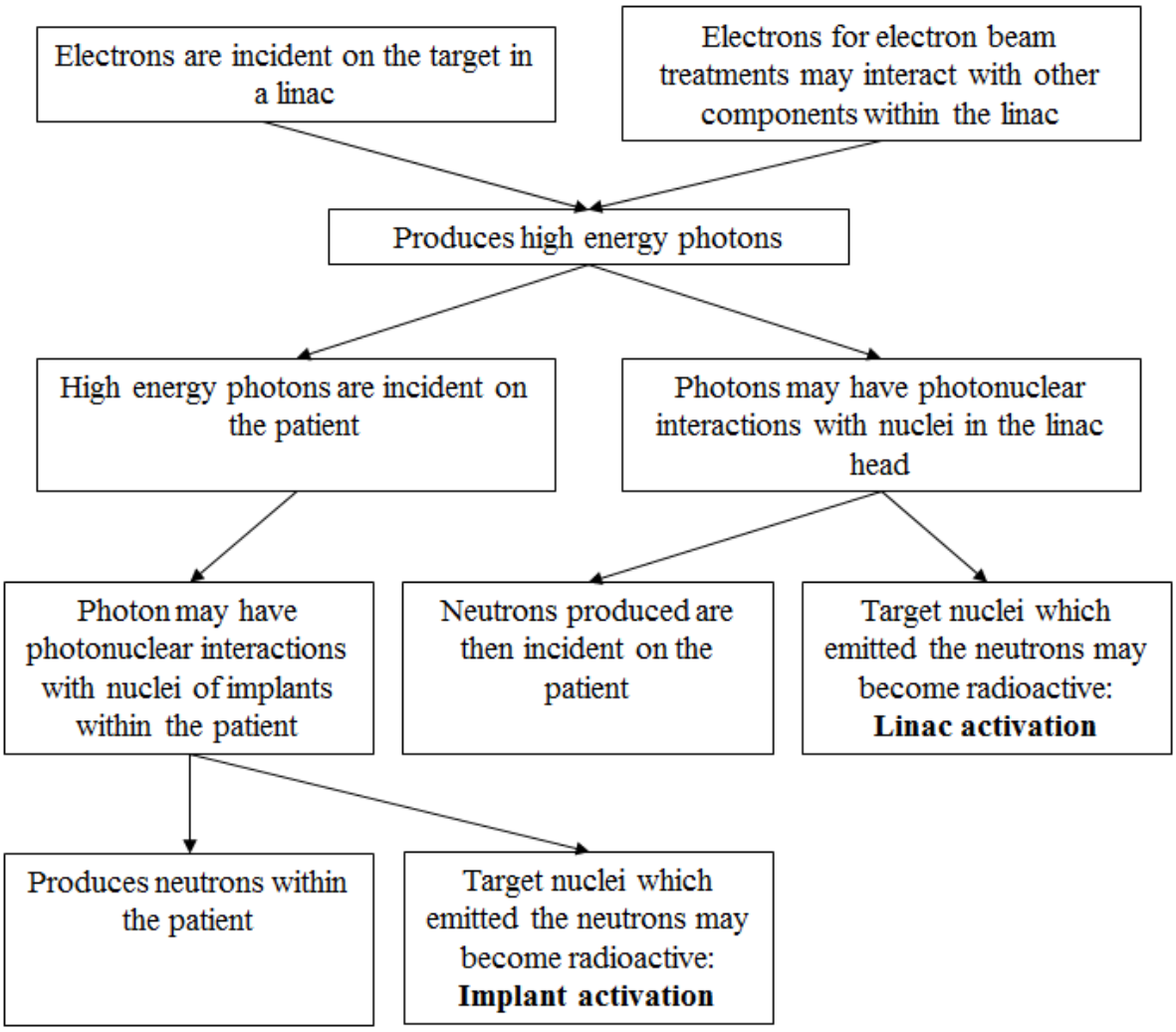

Figure 68: Flowchart summary of the indirect neutron risks, those caused by secondary activations.

7.2.1 Linac activation

Reported staff annual dose estimates from activation caused by 3D conformal radiotherapy techniques range from 0.7 mSv (Almen *et al* 1991) and 0.9 mSv (Donadille *et al* 2008) for a variety of linear accelerator models, up to 2.5 mSv (Perrin *et al* 2003) and 5 mSv (Ho *et al* 2012) both estimated from measurements performed on Elekta Precise linear accelerators. Rawlinson *et al* (2002) report the estimated dose to staff from activation as a result of IMRT treatments (up to 17mSv/year) and conventional treatments (3 mSv/year) from measurements made on a Varian 21EX. IMRT treatments are of interest in this context because they typically require a large number of monitor units and are

performed more frequently in the clinic. However, as they involve small field sizes, the jaws provide additional shielding from activation products. If the jaw position is left unchanged after treatment, the annual dose estimate resulting from the induced activity following 18 MV TBI (0.75 mSv) presented in chapter 6 of this thesis is much lower than that reported for IMRT (17 mSv) and conventional treatment (3 mSv), which reflects the more frequent utilization of these treatments. The estimates of Rawlinson *et al* (2002) are calculated for the delivery of 55 IMRT fractions of 1600 MU (88,000 MU/week) and 150 CRT fractions of 400 MU per week (60,000 MU/week). The typical TBI patient load used to calculate dose estimates is for an average of 26,364 MU/week. The lower patient load of TBI contributes to the lower annual dose estimate. The increased distance between the linac head and the patient (and therefore staff member) in TBI also contribute to the lower dose estimate.

7.2.2 Acitvation of implanted prosthetic hips

Contaminant neutrons in high energy radiotherapy can induce radioactivity in metallic prostheses, even when prostheses are outside the primary field. In chapter 6, ^{56}Mn and ^{52}V were found to be present in prostheses directly irradiated and those exposed between ~1 and 10 cm from the edge of the field. ^{53}Fe was observed only from in-field irradiation and is therefore attributed to the photonuclear effect. Since ^{56}Mn and ^{52}V are produced regardless of whether the prosthetic hip was in- or out-of the photon field, they are attributable to neutron activation. Prostheses irradiated in-field demonstrated count rates 6 – 7.5 times higher than those irradiated out-of-field. The dose measured at the surface of a prosthesis irradiated to 10,000 MU was 0.20 mGy over 12 hours (five half-lives of the longest lived isotope produced in the prosthesis). The surface dose rates for fewer MU and out-of-field irradiations were below the limit of detection for the TLDs. This is very low dose when compared to prescribed radiotherapy doses and even the out-of-field photon dose a patient receives from scatter and leakage radiation, which may be of the order of 0.1% or 70 mGy for a typical prostate treatment of 70 Gy.

7.2.3 Risk from secondary activations

The primary concern relating to the photonuclear production of neutrons in high energy radiotherapy is additional, potentially unknown, exposure to patients. The untargeted tissues within a patient may be receiving an additional, detrimental dose from contaminant neutrons. A secondary concern following neutron production is radioactivity remaining in target nuclei following photonuclear events or secondary activation caused by the ejected neutrons themselves. The activation of the linear accelerator mainly affects radiotherapy staff, as opposed to patients, because the doses are fairly low in magnitude and it is only the staff who spend a large percentage of their time in close proximity to a linac. An indirect risk to patients may arise from activation of implanted materials which have high neutron interaction cross sections.

The annual dose staff receive as a result of activation of the linear accelerator is in the vicinity of ~ 750 μSv for an 18 MV TBI patient load of two per month. The dose can be reduced by closing the jaws at the completion of the beam to take advantage of the existing shielding built into medical linear accelerators.

The activation of hip prostheses in a water phantom revealed that the resultant dose to patients is ~ 0.20 mGy over the 12 hours following beam delivery for a prosthesis directly irradiated by 10,000 MU. This is a very small dose, even when compared to the out-of-field doses proximal organs at risk may receive in a typical treatment in the order of 10s of mGy and in general, direct irradiation of implants is avoided to prevent attenuation of the dose distribution before it reaches the target volume.

7.3 Relevance to thesis objectives

The direct and indirect risks from photoneutrons produced in high energy radiotherapy have been discussed in this chapter. The direct risk from patient exposure to neutrons is discussed in terms of the results of neutron dose measurement which were given in chapter 5. The neutron dose equivalents determined in this study were also compared to the extensive range of values published in literature. There are also indirect risks resulting from secondary activation, where photonuclear interactions result in activation or where the neutrons themselves cause activation. The activities and resultant doses measured were presented in chapter 6 and discussed in this chapter in the context of the risk to both radiotherapy staff and patients.

8. Conclusions

The neutron contamination resulting from photonuclear events occurring in the production of x-ray radiotherapy beams at high energies must be considered when evaluating risk to the patient from untargeted dose. Any potential benefits from the improved x-ray dose distribution must be weighed against any additional risk which arises from the use of higher energy beams. The degree of risk posed by neutron contamination can only be evaluated with accurate quantification of the neutron fluence. The neutron fluence is the simplest quantity to measure, giving a density or rate of particles produced. However, this quantity cannot easily be related to the biological effects which occur in human tissue or therefore, the risk which may be involved. Dose is often used to evaluate risk from radiation exposures because the resultant biological effects are proportional to the dose. The measurement of fluence, and subsequent determination of absorbed dose from neutrons and even neutron dose equivalent all require some degree of understanding of the neutron energy spectrum produced.

The use of ^{6}LiF and ^{7}LiF TLD pairs to measure neutrons in radiotherapy is quite common and can be done without detailed knowledge of the neutron energy spectrum produced by a medical linear accelerator; provided a correction for energy spectrum is used in the calibration of these detectors. However to determine the dose which would be absorbed by tissue if irradiated by the same neutron fluence a highly accurate energy spectrum is required. The interactions neutrons undergo with the isotopes present in tissue are different to those which occur with the lithium and fluoride nuclei present in the TLD material or any other detector which might be used to quantify neutron contamination.

There have been a wide range of values published in the results of peer reviewed papers covering measurements under similar conditions. This wide range of values indicates a high degree of uncertainty which in turn leads to uncertainty amongst clinical physicists and a general mistrust of 15 and 18 MV x-ray beams. How many high energy MU are safe? At what point does the risk become unacceptable? The current methods for quantifying neutron contamination in radiotherapy beams must be improved in order to address the uncertainty and allow accurate assessments of the risks.

The greatest challenge to accuracy in neutron detection and dosimetry no doubt arises from the strong energy dependence of neutron interaction cross sections in many materials. This affects the energy dependence of the detector material, as well as the dose absorption in tissue and the damage caused by the energy deposited in tissue by the neutron exposure. One of the most significant obstacles in comparing data measured or calculated in present and future studies is a lack of detailed disclosure in existing published studies regarding the methods used to convert fluence to absorbed dose or dose equivalent. The fluence is the simplest quantity to determine, but is often not reported. The most commonly reported quantity is the neutron dose equivalent which is weighted for the biological effect. This quantity is dependent on the neutron energy and is calculated from the neutron absorbed dose. The dose to tissue from neutrons primarily comes from secondary charged particles released by nuclear interactions within the tissue. The probability of these interactions and the amount of energy they release is strongly dependent on the energies of the incident neutrons.

So, how can we improve our knowledge of the neutron energy spectrum? Monte Carlo modelling of the neutron production and transport allows calculation of the neutron energy spectrum incident on patients treated with high energy x-rays. The energy spectrum is sensitive to the geometry and material of the components within the linac which produce the treatment beam, with most of the neutron contamination being produced in the primary collimation unit of the x-ray beam. The shielding and bending magnet components of the linac, which do not affect the modelling of the photon beam for computational studies of radiotherapy beams, do have an effect on the neutron energy. A great deal of scattering occurs within the lead and tungsten collimators and shields, which reduces the energy of the neutrons. The size of the

room in which the linac is installed also has an effect on the neutron energy, and the material of the walls, floor, ceiling and other scattering surfaces is significant (McCall *et al* 1979). Simulations developed to interrogate neutron energy information should include a great deal of detail on a much larger physical scale than most radiotherapy Monte Carlo simulations.

Whilst it is relatively simple to produce a model of a radiotherapy treatment bunker for a given clinical scenario, it is much harder to acquire detail and model the internal structure and composition of the shielding within a medical linear accelerator. There are obvious differences in the components which produce the x-rays between manufacturers and models of linacs in current use in Australia. There are less obvious, but no less important, differences in the surrounding structures. The Varian TrueBeam linear accelerator for example, has an extremely different approach to shielding design compared with previous Varian linac models. All of these details will have a significant effect on the energy spectrum of neutrons produced by the linac and that which falls incident on a patient treated with a high energy beam.

These details of the design and composition of linacs and particularly shielding components are not readily available. If the uncertainty amongst experts around quantification of neutron contamination is to be reduced, these details are needed. Detailed geometrically accurate simulations can be produced, which will require high powered computation and targeted variance reduction to produce statistically significant results. The photonuclear effect which produces the neutron contamination is a relatively low probability event in the grand scheme of interactions a photon can undergo. This requires a great deal of computational power, as many incident particles are required to produce enough neutrons to be transported and then analysed with an acceptably low statistical uncertainty.

There is currently interest in Australia for installing a proton therapy facility. The risk from contamination from neutrons must be considered against the potential benefits offered by proton therapy. The ability to accurately quantify the risk is essential to the safe implementation of proton therapy techniques.

The neutron dose measured in this study was between 0.1 mSv and 5 mSv per Gy of x-ray dose delivered to the dose output specification point. Doses measured with TLDs were consistently higher than those measured with activation foils. Reported values in literature range from 0.0007 to 42 mSv/Gy with a mean of 2.6 mSv/Gy.

The principles of radiation protection are founded on a conservative attitude toward radiation exposure. Although the linear no-threshold model for low dose exposure is controversial and there is little reliable scientific evidence to support limiting *all* exposures even at very low dose levels, it is likewise difficult (or perhaps impossible) to prove beyond all doubt that there might be a low level dose which is *safe* for human exposure in all circumstances. Therefore a risk management procedure aims to limit *all* unnecessary exposures. If we cannot accurately quantify the neutron dose and therefore the neutron risk, we must take the conservative approach and take reasonable measures to limit this potential exposure.

Other aspects of the risk posed by neutrons also require consideration. Many therapists in local radiotherapy facilities have enquired about entering a bunker following the delivery of high energy beams, as it is known that a degree of activation of the components of linacs can occur. This work has presented dose measurements following TBI deliveries of ~2000 MU per beam and found the dose to be relatively low. In the interests of ALARA and a conservative approach to radiation protection, it is recommended that the in-built shielding and collimation present within linear accelerator treatment units is utilised. The jaws and secondary collimators can be closed following patient treatment before hospital staff enter the room. This can provide a six-fold reduction in the dose resulting from activated components within the linac which are primarily located higher within the treatment head than these final beam collimation components. This result has been discussed with radiation therapy staff at the

hospital where the measurements were taken and has been used to reassure staff concerned about their individual exposure.

In Australia, radiotherapy staff are monitored for radiation exposure, and typically only low levels are observed. If a clinic were to significantly increase its high energy workload, and an increase in staff exposure levels occurred it would be identified by the existing routine monitoring. The option of waiting a set cooling off period of a few minutes before entering the room is not practicable in a busy clinic and staff should instead make use of the built in shielding within the linear accelerator by closing the jaws before re-entering the room to tend to the patient. Software controls could be implemented to automate the jaws moving to the closed position following high energy exposures.

The neutron production and interaction cross sections in predominantly light elements present in human tissue are relatively low, as compared to heavier elements in general. The presence of foreign objects in and around patients presents a new exposure pathway and potential risk. A proportion of patients undergoing radiotherapy are elderly and may have hip replacements. This introduces a high Z, high density prosthesis which may be in close proximity to the target volume or impede the traversal of treatment beams. It is best practise to avoid such structures in treatment planning because of the high x-ray attenuation of high Z materials, but beams will often be allowed to pass nearby or exit through metallic prostheses. Scattered photons incident on these materials have the potential to produce neutrons from within the patient and neutrons produced in the components of the linac itself will be incident on the prosthesis even if no x-ray beams are directly incident. Any neutrons produced or interacting with a metallic implant are likely to produce secondary radioactivity in the atoms of the object. The isotopes produced and their half-lives depend on the composition of the object in question and the likelihood of inducing radioactivity depends on the energies of the incident neutrons.

The doses resulting to tissue surrounding irradiated hip prostheses have been investigated in this study. The dose was found to be around 0.2 mGy over a 12 hour exposure to a prosthesis irradiated to 10,000 MU. This dose is extremely small when compared to magnitude of doses prescribed in radiotherapy and even the out-of-field doses inevitably received by healthy tissues from scattered x-rays. Implants composed of other materials should be evaluated separately as different isotopes will produce different radioisotopes and other interactions may deposit more or less dose to the un-targeted tissues around implanted materials. The size of the prosthesis present also plays an important part.

The risks posed by neutron contamination are primarily from doses deposited in un-targeted healthy tissues during high energy radiotherapy. The production of neutrons in a radiotherapy treatment bunker can also cause induced radioactivity in other materials in the room. The components of the linear accelerator itself are exposed to the highest fluence rate of neutrons and are likely to be the highest source of induced radioactivity in the room after termination of treatment beams. This is a low level of radiation, but may pose a risk to staff members who may spend a large proportion of their time in close proximity to the treatment machines. In addition, whilst patients are unlikely to become activated themselves, any foreign materials present may have high neutron interaction probabilities. Implants such as pace-makers, hip prostheses and so on, may well cause internal neutron production or become activated during high energy radiotherapy.

Recommendations arising from this study:

- ^{6}Li and ^{7}Li enriched TLD pairs can be used to measure neutron fluence in radiotherapy, but an energy correction should be used for the neutron energy spectrum of the calibration source.
- An energy correction is needed to convert measured neutron fluence to absorbed dose and/or dose equivalent.
- Future studies reporting on neutron measurements in radiotherapy should explicitly disclose the values of any energy corrections used to determine fluence, absorbed dose or dose equivalent.
- Radiation therapy staff performing lots of high energy treatments should consider closing the jaws before re-entering the room to shield against neutron induced radioactivity within the linac components.
- The activation of hip prostheses does not result in a significant dose to the surrounding tissue. There are many reasons to avoid irradiation of prostheses during radiotherapy, but the dose from activation should not be a cause of concern.

References

Almen A, Ahlgren L and Mattsson S 1991 Absorbed dose to technicians due to induced activity in linear accelerators for radiation therapy *Physics in medicine and biology* **36** 815

Alpen E L 1997. *Radiation biophysics*, Academic Press.

AOA 2016 Australian Orthopaedic Association National Joint Replacement Registry Annual Report,

Apfel R E and d'Errico F 2002 A neutron spectrometer based on temperature variations in superheated drop compositions *Nuclear Instruments and Methods in Physics Research Section A: Accelerators, Spectrometers, Detectors and Associated Equipment* **476** 298-303

Audi G and Wapstra A 1993 The 1993 atomic mass evaluation:(I) Atomic mass table *Nuclear Physics A* **565** 1-65

Auxier J, Snyder W and Jones T 1968 Neutron interactions and penetration in tissue *Radiation dosimetry* **1** 275-316

Barquero R, Méndez R, Iniguez M, Vega H and Voltchev M 2002 Thermoluminescence measurements of neutron dose around a medical linac *Radiation protection dosimetry* **101** 493-496

Barquero R, Mendez R, Vega-Carrillo H R, Iñiguez M P and Edwards T M 2005 Neutron spectra and dosimetric features around an 18 MV linac accelerator *Health physics* **88** 48-58

Basunia M S 2013 Nuclear Data Sheets for A= 28 *Nuclear Data Sheets* **114** 1189-1291

Bednarz B, Athar B and Xu X G 2010 A comparative study on the risk of second primary cancers in out-of-field organs associated with radiotherapy of localized prostate carcinoma using Monte Carlo-based accelerator and patient models *Medical physics* **37** 1987-1994

Bedogni R, Domingo C, Esposito A, Gentile A, García-Fusté M, de-San-Pedro M, Tana L, d'Errico F, Ciolini R and Di Fulvio A 2013 Calibration of PADC-based neutron area dosemeters in the neutron field produced in the treatment room of a medical LINAC *Radiation Measurements* **50** 78-81

Benites-Rengifo J L, Vega-Carrillo H R and Velazquez-Fernandez J 2014 Photoneutron spectrum measured with a Bonner sphere spectrometer in planetary method mode *Applied Radiation and Isotopes* **83** 256-259

Berger M, Coursey J, Zucker M and Chang J 2009 Stopping-Power & Range Tables for Electrons, Protons, and Helium Ions

Bezak E, Takam R and Marcu L G 2015 Peripheral photon and neutron doses from prostate cancer external beam irradiation *Radiation protection dosimetry* **167** 591-601

Bilski P 2002 Lithium fluoride: from LiF: Mg, Ti to LiF: Mg, Cu, P *Radiation protection dosimetry* **100** 199-205

Blachot J 2010 Nuclear data sheets for A= 116 *Nuclear Data Sheets* **111** 717-895

Browne E and Tuli J 2007 Nuclear data sheets for A= 137 *Nuclear Data Sheets* **108** 2173-2318

Carinou E, Stamatelatos I E, Kamenopoulou V, Georgolopoulou P and Sandilos P 2005 An MCNP-based model for the evaluation of the photoneutron dose in high energy medical electron accelerators *Physica Medica* **21** 95-99

Carron N J 2006. *An introduction to the passage of energetic particles through matter*, CRC Press.

Chadwick J and Goldhaber M 1934 A 'nuclear photo-effect': disintegration of the diplon by g-rays *Nature* **134** 237-238

Chadwick M, Herman M, Obložinský P, Dunn M E, Danon Y, Kahler A, Smith D L, Pritychenko B, Arbanas G and Arcilla R 2011 ENDF/B-VII. 1 nuclear data for science and technology: cross sections, covariances, fission product yields and decay data *Nuclear Data Sheets* **112** 2887-2996

Chen C, Sheu R, Yeh C, Lin U and Jiang S 2006 A detailed study on the neutron contamination for a 10MeV medical electron accelerator *Nuclear Instruments and Methods in Physics Research Section A: Accelerators, Spectrometers, Detectors and Associated Equipment* **562** 1033-1037

Chibani O and Ma C-M C 2003 Photonuclear dose calculations for high-energy photon beams from Siemens and Varian linacs *Medical physics* **30** 1990-2000

Chu W, Lan J, Chao T, Lee C and Tung C 2011 Neutron spectrometry and dosimetry around 15 MV linac *Radiation Measurements* **46** 1741-1744

Coolens C and Childs P 2003 Calibration of CT Hounsfield units for radiotherapy treatment planning of patients with metallic hip prostheses: the use of the extended CT-scale *Physics in medicine and biology* **48** 1591
d'Errico F 1999 Fundamental properties of superheated drop (bubble) detectors *Radiation protection dosimetry* **84** 55-62
d'Errico F, Nath R, Tana L, Curzio G and Alberts W G 1998 In-phantom dosimetry and spectrometry of photoneutrons from an 18 MV linear accelerator *Medical physics* **25** 1717-1724
de Gonzalez A B, Wong J, Kleinerman R, Kim C, Morton L and Bekelman J E 2015 Risk of Second Cancers According to Radiation Therapy Technique and Modality in Prostate Cancer Survivors *International Journal of Radiation Oncology* Biology* Physics* **91** 295-302
Di Fulvio A, Tana L, Caresana M, D'Agostino E, de San Pedro M, Domingo C and d'Errico F 2013 Clinical simulations of prostate radiotherapy using BOMAB-like phantoms: results for neutrons *Radiation measurements* **57** 48-61
Domingo C, Garcia-Fuste M, Morales E, Amgarou K, Terrón J, Rosello J, Brualla L, Nuñez L, Colmenares R and Gómez F 2010 Neutron spectrometry and determination of neutron ambient dose equivalents in different LINAC radiotherapy rooms *Radiation Measurements* **45** 1391-1397
Donadille L, Trompier F, Robbes I, Derreumaux S, Mantione J, Asselineau B, Amgarou K, Martin A, Bottollier-Depois J and Queinnec F 2008 Radiation protection of workers associated with secondary neutrons produced by medical linear accelerators *Radiation Measurements* **43** 939-943
Esposito A, Bedogni R, Lembo L and Morelli M 2008 Determination of the neutron spectra around an 18MV medical LINAC with a passive Bonner sphere spectrometer based on gold foils and TLD pairs *Radiation Measurements* **43** 1038-1043
Facure A, Falcao R, Da Silva A and Crispim V 2004 Neutron dose rate evaluation for medical linear accelerators *Radiation protection dosimetry* **111** 101-103
Falcao R, Facure A and Silva A 2007 Neutron dose calculation at the maze entrance of medical linear accelerator rooms *Radiation protection dosimetry* **123** 283-287
Faulkner K, Broadhead D and Harrison R 1999 Patient dosimetry measurement methods *Applied Radiation and Isotopes* **50** 113-123
Fermi E 1934 Radioattività indotta da bombardamento di neutroni *La ricerca scientifica* **5** 1921-1938
Fernandez F, Domingo C, Amgarou K, Castelo J, Bouassoule T, Garcia M and Luguera E 2007 Neutron measurements in a Varian 2100C LINAC facility using a Bonner sphere system based on passive gold activation detectors *Radiation protection dosimetry* **126** 361-365
Fiechtner A and Wernli C 1999 Individual neutron monitoring with CR-39 detectors at an accelerator centre *Radiation protection dosimetry* **85** 35-38
Fischer H W, Tabot B E and Poppe B 2006 Activation processes in a medical linear accelerator and spatial distribution of activation products *Physics in medicine and biology* **51** N461
Followill D, Geis P and Boyer A 1997 Estimates of whole-body dose equivalent produced by beam intensity modulated conformal therapy *International Journal of Radiation Oncology* Biology* Physics* **38** 667-672
Followill D S and Nüsslin F 2007 POINT/COUNTERPOINT *Medical physics* **34** 1877
Fujii T, Tanaka H, Maruhashi A, Ono K and Sakurai Y 2011 Study on optimization of multiionization-chamber system for BNCT *Applied Radiation and Isotopes* **69** 1862-1865
Ghassoun J, Senhou N and Jehouani A 2011 Neutron and photon doses in high energy radiotherapy facilities and evaluation of shielding performance by Monte Carlo method *Annals of Nuclear Energy* **38** 2163-2167
Golnik N, Kamiński P and Zielczyński M 2004 A measuring system with a recombination chamber for neutron dosimetry around medical accelerators *Radiation protection dosimetry* **110** 273-276
Golnik N, Zielczyński M, Bulski W, Tulik P and Pałko T 2007 Measurements of the neutron dose near a 15 Mv medical linear accelerator *Radiation protection dosimetry* **126** 619-622
Gregori B, Papadopulos S, Cruzate J and Kunst J 2002 Multisphere neutron spectrometric system with thermoluminescence dosemeters: sensitive improvement *Radiation protection dosimetry* **101** 133-136
Hälg R, Besserer J, Boschung M, Mayer S, Lomax A and Schneider U 2014 Measurements of the neutron dose equivalent for various radiation qualities, treatment machines and delivery techniques in radiation therapy *Physics in medicine and biology* **59** 2457

Hall E J, Martin S G, Amols H and Hei T K 1995 Photoneutrons from medical linear accelerators—radiobiological measurements and risk estimates *International Journal of Radiation Oncology* Biology* Physics* **33** 225-230

Heaton H T and Jacobs R 1979. *Proceedings of a Conference on Neutrons from Electron Medical Accelerators: proceedings of a conference held at the National Bureau of Standards, Gaithersburg, Maryland, April 9-10, 1979*, US Dept. of Commerce, National Bureau of Standards: for sale by the Supt. of Docs., US Govt. Print. Off.

Ho L, White P, Chan E, Chan K, Ng J and Tam T 2012 Evaluation of Optimum Room Entry Times for Radiation Therapists after High Energy Whole Pelvic Photon Treatments *J Occup Health* **54** 131-140

Howell R M, Ferenci M S, Hertel N E and Fullerton G D 2005a Investigation of secondary neutron dose for 18 MV dynamic MLC IMRT delivery *Medical physics* **32** 786-793

Howell R M, Ferenci M S, Hertel N E, Fullerton G D, Fox T and Davis L W 2005b Measurements of secondary neutron dose from 15 MV and 18 MV IMRT *Radiation protection dosimetry* **115** 508-512

Howell R M, Hertel N E, Wang Z, Hutchinson J and Fullerton G D 2006 Calculation of effective dose from measurements of secondary neutron spectra and scattered photon dose from dynamic MLC IMRT for 6MV, 15MV, and 18MV beam energies *Medical physics* **33** 360-368

Howell R M, Kry S F, Burgett E, Hertel N E and Followill D S 2009 Secondary neutron spectra from modern Varian, Siemens, and Elekta linacs with multileaf collimators *Medical physics* **36** 4027-4038

Hsu F-Y, Chang Y-L, Liu M-T, Huang S-S and Yu C-C 2010 Dose estimation of the neutrons induced by the high energy medical linear accelerator using dual-TLD chips *Radiation Measurements* **45** 739-741

Huang W, Li Q and Lin Y 2005 Calculation of photoneutrons produced in the targets of electron linear accelerators for radiography and radiotherapy applications *Nuclear Instruments and Methods in Physics Research Section B: Beam Interactions with Materials and Atoms* **229** 339-347

ICRP103 2007. *The 2007 recommendations of the international commission on radiological protection*, Elsevier Oxford, UK.

ICRP116 2010 Conversion Coefficients for Radiological Protection Quantities for External Radiation Exposures. ICRP Publication 116 *Ann. ICRP* **40**

Ipe N E, Roesler S, Jiang S and Ma C. Neutron measurements for intensity Modulated Radiation therapy. Proceedings of the 22nd Annual International Conference of the IEEE Engineering In Medicine and Biology Society, July, 2000. 23-28.

ISO8529-1 2001 Reference neutron radiations First ed International Organization for Standardization.

Israngkul-Na-Ayuthaya I, Suriyapee S and Pengvanich P 2015 Evaluation of equivalent dose from neutrons and activation products from a 15-MV X-ray LINAC *Journal of Radiation Research* rrv045

JCGM 1995 Guide to the Expression of Uncertainty in Measurement, edition, 1993, corrected and reprinted 1995, Joint Commitee for Guides in Metrology (Geneva, Switzerland), ISBN 92-67-10188-9

Johansson K, Ohlsson M, Olsson N, Blomgren J and Renberg P 1999 Neutron induced single-word multiple-bit upset in SRAM *Nuclear Science, IEEE Transactions on* **46** 1427-1433

Keall P J, Siebers J V, Jeraj R and Mohan R 2003 Radiotherapy dose calculations in the presence of hip prostheses *Medical Dosimetry* **28** 107-112

Keehan S, Smith R L, Millar J, Esser M, Taylor M L, Lonski P, Kron T and Franich R D 2017 Activation of hip prostheses in high energy radiotherapy and resultant dose to nearby tissue *Journal of Applied Clinical Medical Physics* **18** 100-105

Keehan S, Taylor M, Smith R, Dunn L, Kron T and Franich R 2015 Dose and gamma-ray spectra from neutron-induced radioactivity in medical linear accelerators following high-energy total body irradiation *Radiation Protection Dosimetry*

Kessler Jr E, Dewey M S, Deslattes R, Henins A, Börner H, Jentschel M, Doll C and Lehmann H 1999 The deuteron binding energy and the neutron mass *Physics Letters A* **255** 221-229

Khan F M and Gibbons J P 2014. *Khan's the physics of radiation therapy*, Lippincott Williams & Wilkins.

Kim H S and Lee J K 2007 Assessment and measurement of the photoneutron field produced in the Varian medical linear accelerator *Journal of nuclear science and technology* **44** 95-101

Kralik M and Turek K 2004 Characterisation of neutron fields around high-energy X-ray radiotherapy machines *Radiation protection dosimetry* **110** 503-507
Krane K S 1987 Introductory nuclear physics *Introductory Nuclear Physics, by Kenneth S. Krane, pp. 864. ISBN 0-471-80553-X. Wiley-VCH, October 1987.* **1**
Kron T 1999 Applications of thermoluminescence dosimetry in medicine *Radiation protection dosimetry* **85** 333-340
Kry S F, Howell R M, Salehpour M and Followill D S 2009a Neutron spectra and dose equivalents calculated in tissue for high-energy radiation therapy *Medical physics* **36** 1244-1250
Kry S F, Howell R M, Titt U, Salehpour M, Mohan R and Vassiliev O N 2008 Energy spectra, sources, and shielding considerations for neutrons generated by a flattening filter-free Clinac *Medical physics* **35** 1906-1911
Kry S F, Price M, Followill D, Mourtada F and Salehpour M 2007a The use of LiF (TLD-100) as an out-of-field dosimeter *Journal of Applied Clinical Medical Physics* **8**
Kry S F, Salehpour M, Followill D S, Stovall M, Kuban D A, White R A and Rosen I I 2005a The calculated risk of fatal secondary malignancies from intensity-modulated radiation therapy *International Journal of Radiation Oncology* Biology* Physics* **62** 1195-1203
Kry S F, Salehpour M, Followill D S, Stovall M, Kuban D A, White R A and Rosen I I 2005b Out-of-field photon and neutron dose equivalents from step-and-shoot intensity-modulated radiation therapy *International Journal of Radiation Oncology* Biology* Physics* **62** 1204-1216
Kry S F, Salehpour M, Titt U, White R A, Stovall M and Followill D 2009b Monte Carlo study shows no significant difference in second cancer risk between 6-and 18-MV intensity-modulated radiation therapy *Radiotherapy and Oncology* **91** 132-137
Kry S F, Titt U, Followill D, Pönisch F, Vassiliev O N, White R A, Stovall M and Salehpour M 2007b A Monte Carlo model for out-of-field dose calculation from high-energy photon therapy *Medical physics* **34** 3489-3499
L'Annunziata M F 2007. *Radioactivity: Introduction and History*, Elsevier.
La Tessa C, Berger T, Kaderka R, Schardt D, Burmeister S, Labrenz J, Reitz G and Durante M 2014 Characterization of the secondary neutron field produced during treatment of an anthropomorphic phantom with x-rays, protons and carbon ions *Physics in medicine and biology* **59** 2111
Lin J-P, Chu T-C, Lin S-Y and Liu M-T 2001 The measurement of photoneutrons in the vicinity of a Siemens Primus linear accelerator *Applied Radiation and Isotopes* **55** 315-321
Lin J-P, Liu W-C and Lin C-C 2007 Investigation of photoneutron dose equivalent from high-energy photons in radiotherapy *Applied radiation and isotopes* **65** 599-604
Lonski P, Keehan S, Siva S, Pham D, Franich R, Taylor M and Kron T 2017 Out-of-field in vivo dosimetry using TLD in SABR for primary kidney cancer involving mixed photon fields *Physica Medica* **37** 9-15
Maglieri R, Licea A, Evans M, Seuntjens J and Kildea J 2015 Measuring neutron spectra in radiotherapy using the nested neutron spectrometer *Medical physics* **42** 6162-6169
Martinez-Ovalle S, Barquero R, Gómez-Ros J and Lallena A 2011 Neutron dose equivalent and neutron spectra in tissue for clinical linacs operating at 15, 18 and 20 MV *Radiation protection dosimetry* **147** 498-511
McCall R, Jenkins T and Shore R 1979 Transport of accelerator produced neutrons in a concrete room *Nuclear Science, IEEE Transactions on* **26** 1593-1602
McCall R C, Almond P, Holeman G, Devanney I, Lanzl L and Fuller E 1984 Neutron contamination from medical electron accelerators *NCRP Report* **79**
McCall R C, McGinley P H and Huffman K E 1999 Room scattered neutrons *Medical physics* **26** 206-207
McKeever S W, Moscovitch M and Townsend P D 1995 Thermoluminescence dosimetry materials: properties and uses
MCNP6 2013 MCNP6 *In:* PELOWITZ, D. B. (ed.) Los Alamos National Laboratory.
Mesbahi A, Keshtkar A, Mohammadi E and Mohammadzadeh M 2010 Effect of wedge filter and field size on photoneutron dose equivalent for an 18MV photon beam of a medical linear accelerator *Applied Radiation and Isotopes* **68** 84-89
Mohammadi N, Miri-Hakimabad H, Rafat-Motavlli L, Akbari F and Abdollahi S 2015 Neutron spectrometry and determination of neutron contamination around the 15 MV Siemens Primus LINAC *Journal of Radioanalytical and Nuclear Chemistry* 1-8

Nedaie H A, Darestani H, Banaee N, Shagholi N, Mohammadi K, Shahvar A and Bayat E 2014 Neutron dose measurements of Varian and Elekta linacs by TLD600 and TLD700 dosimeters and comparison with MCNP calculations *Journal of medical physics/Association of Medical Physicists of India* **39** 10

Ongaro C, Zanini A, Nastasi U, Ródenas J, Ottaviano G and Manfredotti C 2000 Analysis of photoneutron spectra produced in medical accelerators *Physics in medicine and biology* **45** L55

Ortec 2006 Maestro-32 6.0 ed USA.

Pelliccioni M 1998 Radiation weighting factors and high energy radiation *Radiation protection dosimetry* **80** 371-378

Pena J, Franco L, Gomez F, Iglesias A, Pardo J and Pombar M 2005 Monte Carlo study of Siemens PRIMUS photoneutron production *Physics in medicine and biology* **50** 5921

Perrin B, Walker A and Mackay R 2003 A model to calculate the induced dose rate around an 18 MV ELEKTA linear accelerator *Physics in medicine and biology* **48** N75

Rana S B and Pokharel S 2014 A dosimetric study of volumetric modulated arc therapy planning techniques for treatment of low-risk prostate cancer in patients with bilateral hip prostheses *South Asian journal of cancer* **3** 18

Rawlinson J A, Islam M K and Galbraith D M 2002 Dose to radiation therapists from activation at high-energy accelerators used for conventional and intensity-modulated radiation therapy *Medical Physics* **29** 598-608

Rebello W, Silva A and Facure A 2008 Multileaf shielding design against neutrons produced by medical linear accelerators *Radiation protection dosimetry* **128** 227-233

Reft C, Alecu R, Das I J, Gerbi B J, Keall P, Lief E, Mijnheer B J, Papanikolaou N, Sibata C and Van Dyk J 2003 Dosimetric considerations for patients with HIP prostheses undergoing pelvic irradiation. Report of the AAPM Radiation Therapy Committee Task Group 63 *Medical physics* **30** 1162-1182

Reft C S, Runkel-Muller R and Myrianthopoulos L 2006 In vivo and phantom measurements of the secondary photon and neutron doses for prostate patients undergoing 18MV IMRT *Medical physics* **33** 3734-3742

Roberts R 2001 How accurate is a CT-based dose calculation on a pencil beam TPS for a patient with a metallic prosthesis? *Physics in medicine and biology* **46** N227

Romero-Expósito M, Sánchez-Nieto B, Terrón J, Lopes M, Ferreira B, Grishchuk D, Sandín C, Moral-Sánchez S, Melchor M and Domingo C 2015 Commissioning the neutron production of a Linac: Development of a simple tool for second cancer risk estimation *Medical physics* **42** 276-281

Rosman K and Taylor P 1999 Report of the IUPAC subcommittee for isotopic abundance mea surements *Pure Appl. Chem* **71** 1593-1607

Roy S and Sandison G 2000 Shielding for neutron scattered dose to the fetus in patients treated with 18 MV x-ray beams *Medical physics* **27** 1800-1803

Saeed M, Moustafa O, Yasin O, Tuniz C and Habbani F 2009 Doses to patients from photoneutrons emitted in a medical linear accelerator *Radiation protection dosimetry* ncp029

Saint-Gobain C a D 2001 *In:* DETECTORS, S.-G. C. A. (ed.).

Salah N, Sahare P and Rupasov A 2007 Thermoluminescence of nanocrystalline LiF: Mg, Cu, P *Journal of Luminescence* **124** 357-364

Sánchez-Doblado F, Domingo C, Gómez F, Muñiz J, Barquero R, García-Fusté M, Hartmann G, Romero M, Terrón J and Pena J. On line neutron dose evaluation in patients under radiotherapy. World Congress on Medical Physics and Biomedical Engineering, September 7-12, 2009, Munich, Germany, 2009. Springer, 259-261.

Sánchez-Doblado F, Domingo C, Gómez F, Sánchez-Nieto B, Muñiz J, García-Fusté M, Expósito M, Barquero R, Hartmann G and Terrón J 2012 Estimation of neutron-equivalent dose in organs of patients undergoing radiotherapy by the use of a novel online digital detector *Physics in medicine and biology* **57** 6167

Sanz R B, Villafañe R M, Bayo M and Vega-Carrilho H 2001 Determination of neutron dose to patientes from a 18 MV LINAC *Trabajo CB/UEN-07/039*

Shambira S and Lazarus G 2015 A comparison of 6 MV and 18 MV cancer of the cervix volumetric modulated arc therapy (VMAT) treatment plans for large patient thickness *Physica Medica: European Journal of Medical Physics* **31** S11

Sheikh-Bagheri D and Rogers D 2002 Monte Carlo calculation of nine megavoltage photon beam spectra using the BEAM code *Medical physics* **29** 391-402
Shibata K, Iwamoto O, Nakagawa T, Iwamoto N, Ichihara A, Kunieda S, Chiba S, Furutaka K, Otuka N and Ohasawa T 2011 JENDL-4.0: a new library for nuclear science and engineering *Journal of Nuclear Science and Technology* **48** 1-30
Shoushan W, Goulong C, Fang W, Yuanfang L, Ziying Z and Jianhuan Z 1986 Newly developed highly sensitive LiF (Mg, Cu. P) TL chips with high signal-to-noise ratio *Radiation protection dosimetry* **14** 223-227
Singh B 2007 Nuclear data sheets for A= 64 *Nuclear Data Sheets* **108** 197-364
Sohrabi M, Hakimi A and Mahdavi S R 2016 A novel position-sensitive mega-size dosimeter for photoneutrons in high-energy X-ray medical accelerators *Physica Medica* **32** 778-786
Spurný F, Médioni G and Portal G 1976 Transfert d'énergie des neutrons rapides dans quelques matériaux thermoluminescents *Radioprotection* **11** 219
Takahashi K, Tazaki S, Miyahara J, Karasawa Y and Niimura N 1996 Imaging performance of imaging plate neutron detectors *Nuclear Instruments and Methods in Physics Research Section A: Accelerators, Spectrometers, Detectors and Associated Equipment* **377** 119-122
Takam R, Bezak E, Liu G and Marcu L 2012 The use of enriched 6Li and 7Li Lif: Mg, Cu, P glass-rod thermoluminescent dosemeters for linear accelerator out-of-field radiation dose measurements *Radiation protection dosimetry* **150** 22-33
Takam R, Bezak E, Yeoh E and Liu G. In-phantom peripheral organ doses from prostate irradiation using 18 MV external beam radiotherapy measured with 6LiF: Mg, Cu, P & 7LiF: Mg, Cu, P Glass-Rod TLDs. World Congress on Medical Physics and Biomedical Engineering, September 7-12, 2009, Munich, Germany, 2009. Springer, 557-560.
Tanaka S-i and Takeuchi K 1975 Neutron energy-dependent kerma factors for nuclides, Japan Atomic Energy Research Inst., Tokyo
Tanner R, Bartlett D and Hager L 2005 Operational and dosimetric characteristics of etched-track neutron detectors in routine neutron radiation protection dosimetry *Radiation measurements* **40** 549-559
Taylor M L and Kron T 2011 Consideration of the radiation dose delivered away from the treatment field to patients in radiotherapy *Journal of medical physics/Association of Medical Physicists of India* **36** 59
Taylor M L, Kron T and Franich R D 2011 Assessment of out-of-field doses in radiotherapy of brain lesions in children *International Journal of Radiation Oncology* Biology* Physics* **79** 927-933
Thomas D, Bardell A and Macaulay E 2002 Characterisation of a gold foil-based Bonner sphere set and measurements of neutron spectra at a medical accelerator *Nuclear Instruments and Methods in Physics Research Section A: Accelerators, Spectrometers, Detectors and Associated Equipment* **476** 31-35
Valentin J 2002 Basic anatomical and physiological data for use in radiological protection: reference values: ICRP Publication 89 *Annals of the ICRP* **32** 1-277
Vanhavere F, Huyskens D and Struelens L 2004 Peripheral neutron and gamma doses in radiotherapy with an 18 MV linear accelerator *Radiation protection dosimetry* **110** 607-612
Varian 1996 (Confidential Information, used with permission) *Varian Oncology Systems Monte Carlo Project*
Vega Carrillo H R and Iñiguez de la Torre M P 2002 Catalogue to select the initial guess spectrum during unfolding *Nuclear Instruments and Methods in Physics Research Section A: Accelerators, Spectrometers, Detectors and Associated Equipment* **476** 270-272
Verellen D and Vanhavere F 1999 Risk assessment of radiation-induced malignancies based on whole-body equivalent dose estimates for IMRT treatment in the head and neck region *Radiotherapy and Oncology* **53** 199-203
Walker J 2008. *Fundamentals of physics*, Wiley.
Waller E, Jamieson T, Cole D, Cousins T and Jammal R 2003 Experimental and computational determination of neutron dose equivalent around radiotherapy accelerators *Radiation protection dosimetry* **107** 225-232
Xiaolong H 2009 Nuclear data sheets for A= 198 *Nuclear Data Sheets* **110** 2533-2688
Youssian D and Horowitz Y 1998 Estimation of gamma dose in neutron dosimetry using peak 4 to peak 5 ratios in LiF: Mg, Ti (TLD-100/600) *Radiation protection dosimetry* **77** 151-158

Zabihzadeh M, Ay M R, Allahverdi M, Mesbahi A, Mahdavi S R and Shahriari M 2009 Monte Carlo estimation of photoneutrons contamination from high-energy X-ray medical accelerators in treatment room and maze: a simplified model *Radiation protection dosimetry* **135** 21-32

Zanini A, Durisi E, Fasolo F, Ongaro C, Visca L, Nastasi U, Burn K, Scielzo G, Adler J-O and Annand J 2004 Monte Carlo simulation of the photoneutron field in linac radiotherapy treatments with different collimation systems *Physics in medicine and biology* **49** 571

Zaremba T, Jakobsen A R, Søgaard M, THØGERSEN A, Johansen M B, Madsen L B and Riahi S 2015 Risk of Device Malfunction in Cancer Patients with Implantable Cardiac Device Undergoing Radiotherapy: A Population-Based Cohort Study *Pacing and Clinical Electrophysiology* **38** 343-356